CZECH TECHNICAL UNIVERSITY
IN PRAGUE
Faculty of Nuclear Sciences and Physical Engineering
Department of Physics

Diploma Thesis

Study of the Coherent Production of J/ψ in Pb-Pb UPC with Run 2 Data

Bc. Roman Lavička

Supervisor: prof. Jesús Guillermo Contreras Nuño, Ph.D.

Prague, 2016

ČESKÉ VYSOKÉ UČENÍ TECHNICKÉ
V PRAZE
Fakulta jaderná a fyzikálně inženýrská
Katedra fyziky

Diplomová práce

Studium koherentní produkce J/ψ v Pb-Pb UPC s daty z Run 2

Bc. Roman Lavička

Vedoucí práce: prof. Jesús Guillermo Contreras Nuño, Ph.D.

Praha, 2016

ČESKÉ VYSOKÉ UČENÍ TECHNICKÉ V PRAZE
FAKULTA JADERNÁ A FYZIKÁLNĚ INŽENÝRSKÁ
PRAHA 1 - STARÉ MĚSTO, BŘEHOVÁ 7 - PSČ 115 19

Katedra: fyziky *Akademický rok:* 2015/16

ZADÁNÍ DIPLOMOVÉ PRÁCE

Posluchač: Bc. Roman Lavička

Obor: Experimentální jaderná a částicová fyzika

Název práce: Studium koherentní produkce J/Psi v Pb-Pb UPC s daty z Run 2

Název práce: Study of the Coherent Production of J/Psi in Pb-Pb UPC with Run 2 Data
(anglicky)

Osnova:

1) Příprava triggeru pro ultraperiferální srážky ve střední rapiditě pro Run 2
2) Náběr dat při Pb-Pb UPC pro Run 2
3) Získání luminosity z nabraných dat
4) Výpočet korekce na akceptanci a efektivitu
5) Závislost účinného průřezu koherentní produkce J/Psi na rapiditě

Práce bude vypracována v anglickém jazyce.

Doporučená literatura:

[1] E. Abbas, et al. [ALICE collaboration], Charmonium and electron-positron pair photoproduction at midrapidity in ultra-peripheral Pb-Pb collisions at sqrt(s) = 2.76 TeV, arXiv:1305.1467 [nucl-ex]

[2] K. Aamodt, et al. [ALICE collaboration], The ALICE experimetn at the CERN LHC, JINST 3 (2008) S08002.

[3] J. G. Contreras, J. D. Tapaki, Ultra-peripheral heavy-ion collisions at the LHC, Int. J. Mod. Phys. A30 (2015) 1542012.

Jméno a pracoviště vedoucího diplomové práce:

prof. Guillermo Contreras Nuno, Ph.D., FJFI ČVUT

konzultanti: Mgr. Michal Broz, Ph.D., FJFI ČVUT, Ing. Jaroslav Adam, FJFI ČVUT

Dr. Evgeny Kryshen, CERN

Součástí zadání diplomové práce je její uložení na webové stránky katedry fyziky a zaslání abstraktu a klíčových slov ve formátu WORD na e-mailovou adresu katedry fyziky: kf@fjfi.cvut.cz

Datum zadání diplomové práce: 23.10.2015

Termín odevzdání diplomové práce: 06.05.2016

vedoucí katedry .... *děkan*

ČESKÉ VYSOKÉ UČENÍ TECHNICKÉ V PRAZE Fakulta jaderná a fyzikálně inženýrská -1-

V Praze dne 23.10.2015

Prohlášení:

Prohlašuji, že jsem svou diplomovou práci vypracoval samostatně a použil jsem pouze podklady (literaturu, projekty, SW atd...) uvedené v přiloženém seznamu.

Nemám závažný důvod proti použití tohoto školního díla ve smyslu § 60 Zákona č. 121/200 Sb., o právu autorském, o právech souvisejících s právem autorským a o změně některých zákonů (autorský zákon).

V Praze dne 6. května 2016

Roman Lavička

Title:
Study of the Coherent Production of J/ψ in Pb-Pb UPC with Run 2 Data

Author: Roman Lavička

Specialization: Experimental nuclear and particle physics

Sort of project: Diploma thesis

Supervisor: prof. Jesús Guillermo Contreras Nuño, Ph.D.

Abstract:
There are several different predictions for the behaviour of the gluon distribution in nuclei at small Bjorken x and experimental data is needed to chose among them. This is achieved by measuring the cross section of processes specially sensitive to this parton distribution. We focus on ultra-peripheral collision of lead-lead nuclei producing a J/ψ meson. Our main task is to calculate the rapidity- and t-dependence of the cross section. In this thesis we report our results with Run 1 data collected with an integrated luminosity of $22.4^{+0.9}_{-1.2}$ $\mu\mathrm{b}^{-1}$. The cross section dependence on rapidity is $\mathrm{d}\sigma^{\mathrm{coh}}_{\mathrm{J}/\psi}/\mathrm{d}y = 0.98^{+0.07}_{-0.06}(\mathrm{sta})$ mb. A detailed description of the measurement as well as the first results on low intensity data samples of Run 2 are available in the thesis. Descriptions of our work on UPC triggers and the luminosity calculation framework are parts of the thesis as well.

Key words: Ultra-peripheral heavy-ion collisions, ALICE, J/ψ, triggers, luminosity calculation, differential cross section

Název práce:
Studium koherentní produkce J/Ψ v Pb-Pb UPC s daty z Run 2

Autor: Roman Lavička

Abstrakt:
Pro popis chování rozložení gluonů v jádře při malých Bjorkenovo x existuje několik různých předpovědí. Abychom mezi nimi mohli vybrat tu správnou, potřebujeme experimentální data. Na nich se naměří účinný průřez procesů, které jsou zvlášť citlivé na tuto partonovou distribuci. My se zaměřujeme na ultraperiferální srážky jader olova, které produkují J/ψ mezon. Naším hlavním úkolem je spočítat závislost účinného průřezu na rapiditě a t. V této stati publikujeme naše výsledky z dat z Run 1, která byla nabrána s celkovou luminozitou $22.4^{+0.9}_{-1.2}$ $\mu\mathrm{b}^{-1}$. Účinnost účinného průřezu na rapiditě nám vyšla $\mathrm{d}\sigma^{\mathrm{coh}}_{\mathrm{J}/\psi}/\mathrm{d}y = 0.98^{+0.07}_{-0.06}(\mathrm{sta})$ mb. Celé měření společně s prvními výsledky z dat z Run 2 naměřených s nízkou intensitou jsou v práci k dispozici. Součástí stati je také popis naší práce na vývoji UPC triggerů a nástroje k výpočtu luminozity.

Klíčová slova: ultraperiferální srážky těžkých iontů, ALICE, J/ψ, triggery, výpočet luminozity, diferenciální účinný průřez

Acknowledgement

I would like to express my gratitude to my supervisor prof. Jesús Guillermo Contreras Nuño, Ph.D. for his invaluable advice and support during the realization of this work. I would also like to express my gratitude to my CERN Summer Student Programme supervisor Dr. Evgeny Kryshen for the opportunity to spend an amazing summer side-by-side the best people in the field and gaining new knowledge. I would also like to thank Mgr. Michal Broz, Ph.D for his preparation of the Monte Carlo simulations and Ing. Jaroslav Adam for his quick helps with programming difficulties.

Preface

One of the main goals of physics is to give an answer to the question - what are we made of? As technology improves we are able to study smaller and smaller pieces of our world, revealing that matter is made of atoms, atoms are made of their nuclei and electrons and so on. Nowadays modern detectors give us an opportunity to measure the distribution of quarks and gluons inside hadrons. In this work, data from ALICE is used to measure a process which is expected to be specially sensitive to the gluon distribution in lead nuclei.

Originally, the thesis should have used data from the Run 2 at the LHC. These data were collected during 2015, but they are not yet available for analyses due to unexpected problems with the calibration of the TPC. The thesis work was then developed using data from 2011 so that when the data from 2015 is finally usable, the full machinery will be ready to perform the analysis.

In this work we focus on events where only one J/ψ meson was created in a collision of lead ions and decayed to a muon pair. Our main interest is to calculate the cross section dependence of such process on the transferred momentum $|t|$, when the J/ψ was created at mid-rapidity. The data from 2011 have been already analysed by ALICE and the cross section dependence on rapidity y was measured [1, 2, 3]. Results were compared to several models and it was found that only those with mild shadowing could successfully described the measured data. The dependence of the cross section on $|t|$ maps the gluon distribution in the impact parameter plane. This measurement has never been performed for the coherent production of J/ψ. Its realization with ALICE will help to constrain even more the models and will yield a new understanding of the gluon distribution in lead nuclei.

A brief overview of the physics relevant for this measurement is given in Chapter 1 - Introduction where we explain: what are ultra-peripheral collisions, the J/ψ particle, kinematic variables used and how the STARlight model calculates the cross section. In the next chapter, which is focused on the ALICE experiment, we describe its several subdetectors and triggers used in this work. In Chapter 3 we describe the work-flow to analyse Run 1 data and in Chapter 4 we present the results we obtained. Chapter 5 is dedicated to our work on triggers for data collecting in Run 2 and to the developed tool to compute luminosity. This tool is of utility to the whole Collaboration and in particular, it will be useful to compute the luminosity for the measurement we are interested in. In Chapter 6 we explain the technical difficulties that have prevented the reconstruction of Run 2 data and we show some results on low intensity runs of Run 2 data. The last chapter contains a summary.

Contents

List of Figures

List of Tables

Chapter 1

Introduction

1.1 Structure of matter

The world around us is made of various fundamental particles, which can be combined together to create the atoms we are familiar with. According to spin, we divide these fundamental particles into so-called bosons (integer spin) and fermions (half-integer spin). An important difference between them is that bosons are allowed to occupy the same quantum state, which is not the case for two identical fermions [4].

Our current knowledge about matter is described in the Standard Model. There, as the elementary gauge bosons we identify the photon which propagates the electromagnetic field, Z and $W^{\pm}$ responsible for the weak interaction and the gluon connected with the strong force. According to this theory, one more boson is necessary to give mass to the Z and $W^{\pm}$ bosons. The famous Higgs boson recently discovered at the LHC [5, 6]. The elementary fermions are divided in leptons (electrons, muons, taus and their corresponding neutrinos and antiparticles) and quarks, which exhibit 6 flavours in Nature [7].

Within the Standard Model, the theory which describes the strong interaction is called quantum chromodynamics (QCD) [8]. This theory is a non-abelian gauge theory based on a symmetry group SU(3) [9, 10]. As the electromagnetic force has the familiar electric charge, in QCD we find a colour charge, which has 3 types, normally called red, blue and green. Each of them can take "positive" and "negative" values; the "negative" values are called anti-red, anti-blue and anti-green. The gluons are particles, which carry a pair of colour and anti-colour. The symmetry of the SU(3) gives us 8 possible configurations of gluons.

Unfortunately QCD gives us equations, which we do not know how to solve in the general case. In particular, we cannot solve the equations for the dynamics of the interaction of quarks and gluons, nor how these interact to form bound states. But using perturbative QCD we can set up equations to tell us how the structure of hadrons change when we change the energy of the interaction we use to probe the structure. These equations are only valid in the regime where we can consider that the quarks and gluons are free during the interaction. So we are interested in the study of the structure of bound states, specifically for this thesis in the QCD structure of lead nuclei. The process we are interested in is specially sensitive to the gluonic structure of lead nuclei.

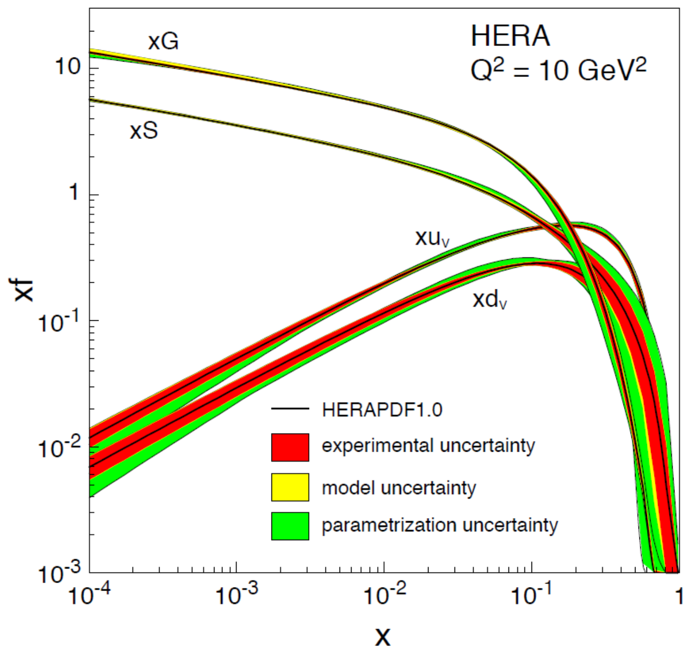

Figure 1.1: Parton distribution functions for different partons in the proton. Taken from Ref. [11].

1.2 Small-x physics

Parton distribution functions (PDF) describe the distribution of the longitudinal component (in a light cone frame) of the momentum of quarks and gluons (partons) in matter at a given energy scale given by the interaction. Before turning on the LHC facility in 2009 the proton PDF were well known in a large kinematic domain for so-called Bjorken x and scale Q^2 as they were measured with high precision at HERA in Hamburg [12, 13]. There it was found that the gluon distribution in the proton grows very fast for decreasing x at small values of x. This growth is so fast that at some point it would violate the unitarity of the cross section, so it has to be slowed down. This is called saturation. With the LHC we got an opportunity to study the PDF of lead nuclei at small values of x for perturbative scales Q^2. As there are many more gluons in nuclei than in the proton one could be more sensitive to saturation effects if they are already present at LHC energies.

1.2.1 Bjorken x

In the infinite momentum frame the Bjorken x is related to the fraction of momentum carried by a gluon or a quark in the nucleon (nucleus) to the total momentum of the nucleon (nucleus). A powerful tool for studying PDFs at small-x is deep inelastic scattering (DIS). Here, in the high energy limit, x is related to the transferred momentum via the centre-of-mass energy s as $s \sim \frac{Q^2}{x}$. From this equation it is clearly seen that small values of x correspond to large energies. In Fig. 1.1 one can see distribution functions for quarks and gluons in the proton for fixed Q^2. The strong rise of the gluon distribution at small-x is clearly seen.

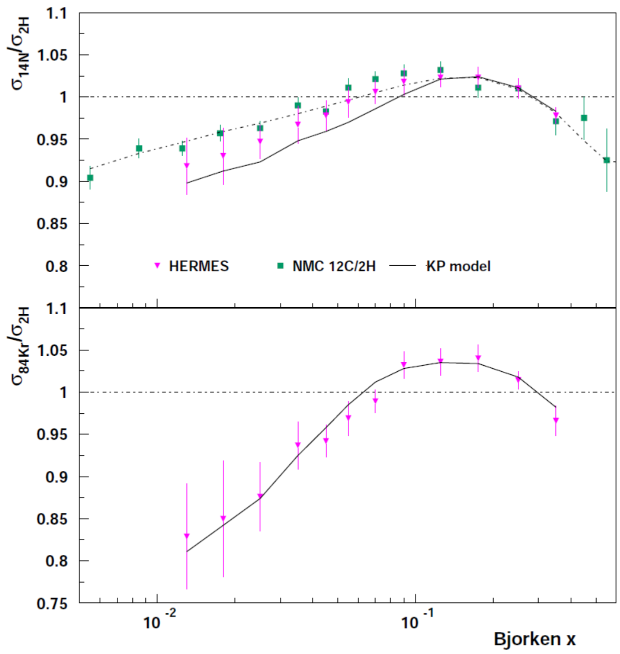

Figure 1.2: The ratio of cross sections of light nucleus and heavy nucleus. Data are obtained from the HERMES experiment (Illustrative figure). Taken from Ref. [14].

1.2.2 Gluon distribution function

The reason, why we want to study the coherent production of J/ψ is its connection with the gluon distribution function in Pb $\sigma \sim G^2(x, Q^2)$, where the scale is related to the mass of the J/ψ as $Q^2 \sim \frac{M^2_{\mathrm{J}/\psi}}{4}$ [15] and thus it is expected to be in the perturbative regime. This distribution cannot be obtained by rescaling the proton distribution function according to the nucleus nucleon number N and proton number Z. For Bjorken x below 0.1 so called shadowing appears and the ratio of structure function of nucleus to structure function of proton decreases. This is an experimental fact and the results of this work could be used to explain this behaviour. An example of the progression of this ratio is shown in Fig. 1.2

The LHC provides collisions at higher energies than ever before in the laboratory, which gives as a larger range in x for a fixed value of Q^2. The rapidity of the coherently produced J/ψ is related to the Bjorken x. At mid-rapidity the process is sensitive to $x \sim 10^{-3}$ for Run 1 energies and $x \sim 0.5 \cdot 10^{-4}$ for Run 2 energies. The $G(x, Q^2)$ distribution does not carry information about the distribution of gluons in the plane transverse to the interaction, the so called impact-parameter plane. Saturation models predict interesting signatures in this plane [16]. To access this information, we also need to measure the $|t|$-dependence of the cross section at a given rapidity. As it will be discussed later, a J/ψ meson is an ideal particle to study this distribution.

J/ψ properties	
Type	meson
Composition	charm quark and antiquark
Discovered	1974, BNL [17] and SLAC [18]
Mass	3096.916 ± 0.011 MeV/c^2
Full width	92.9 ± 2.8 keV/c^2
J^{PC}	1^{--}
Charmness	0 (hidden charm)

Table 1.1: Properties of the J/ψ particle. Taken from Refs. [19].

J/ψ decay channels	
Mode	Fraction (Γ_i/Γ)
hadrons	(87.7 ± 0.5) %
e^+e^-	(5.971 ± 0.032) %
$\mu^+\mu^-$	(5.961 ± 0.033) %

Table 1.2: The main decay channels of the J/ψ particle. Taken from Ref. [19].

1.3 J/ψ particle

The J/ψ is a vector meson. Its main attributes are listed in Tab. 1.1. States, which are composed of $c\bar{c}$ quarks, are called charmonium and the J/ψ is the lowest vector state. The whole family can be seen in Fig. 1.3. The ground state for this family is η_c(1S). Some decay channels of the J/ψ are listed in Tab. 1.2. We can see, that decays to hadrons are the most probable. Probabilities of decays to di-leptons are almost the same (with a little bit higher chance for e^+e^-). Unfortunately, decays to hadrons are quite complicated and it is difficult to reconstruct them. In this paper we focus only on the $\mu^+\mu^-$ channel, because when muons propagate through detectors, they do not radiate as easily as electrons do and therefore we should get a better resolution in $|t|$.

The beauty of this meson is its sharp peak, which can be found at $\sim$3.1 GeV/c^2. This we can compare with other vector mesons in Fig. 1.4. The mass of the J/ψ gives a scale that makes possible to use perturbative QCD at small-x. Adding the fact of the very narrow peak and the possibility to trigger on the leptonic decay channels in UPC at the LHC, we can claim that the J/ψ is an ideal particle for our analysis.

1.4 Mandelstam variables

To study the kinematics of high energy physics is useful to define new kinematic variables. Some of them are so-called Mandelstam variables [20]. These are mostly used in scattering experiments, where we have 2 particles before an interaction and 2 particles after it. All together we have 3 variables, which are labelled as channels (see Fig. 1.5) and are defined by Eq. 1.1. Their

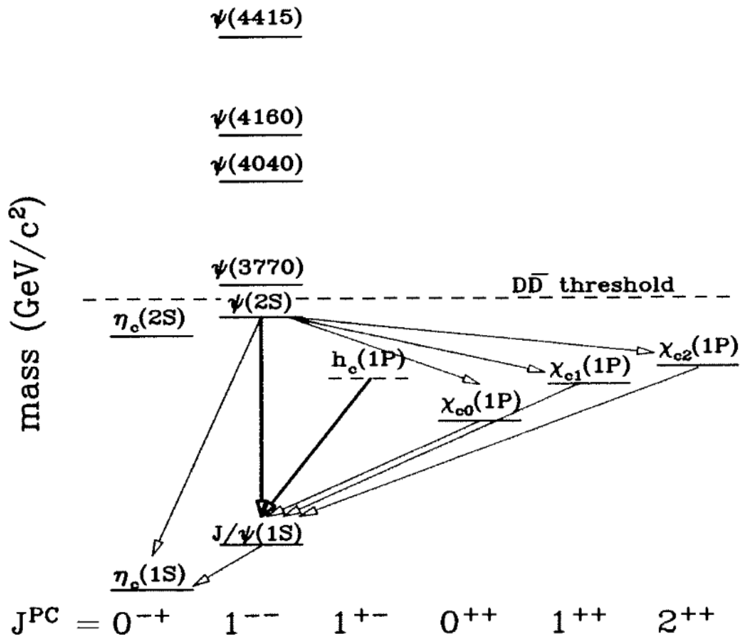

Figure 1.3: The charmonium family. Taken from Ref. [21].

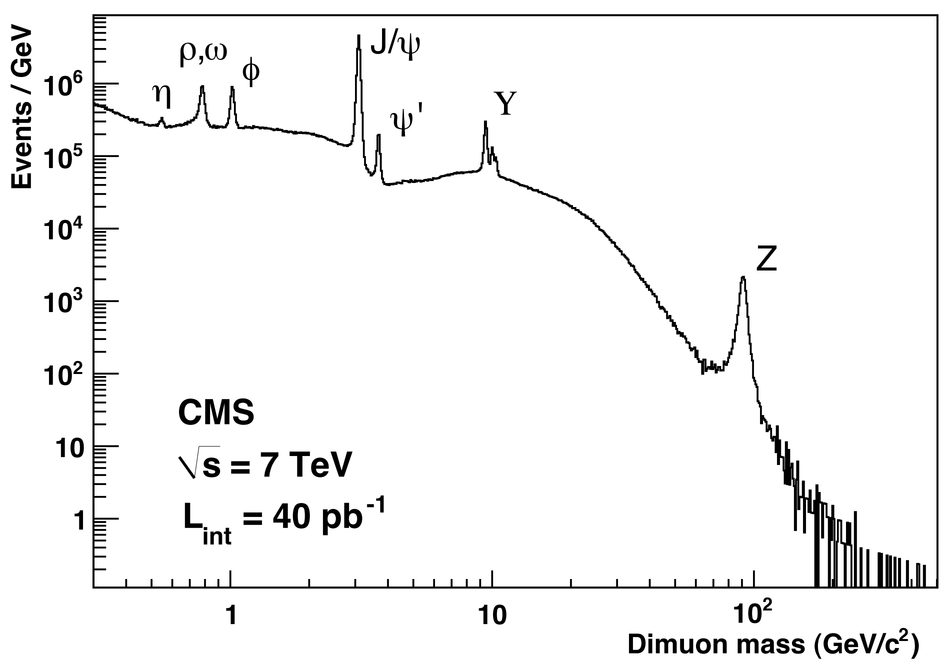

Figure 1.4: Di-muon mass distribution including the continuum and vector mesons. Note, that ψ' is the same particle as ψ(2S). Taken from Ref. [22].

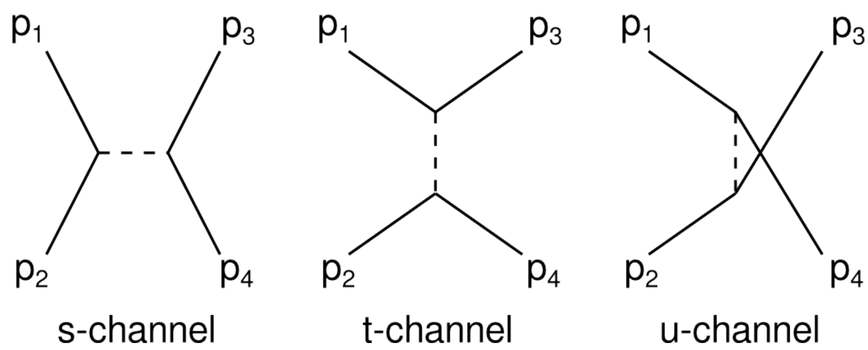

Figure 1.5: s- t- and u- channels of scattering processes.

advantage is that they are Lorentz invariant. Also in the centre-of-mass system they have a clear interpretation. The s-channel represents the square of the total energy of the incoming particles. The t-channel reflects the momentum transfer between incoming and outgoing particles. If we look to Fig. 1.7, one can clearly see, why we are interested in the t-channel.

$$
\begin{aligned}
s &= (p_1 + p_2)^2 = (p_3 + p_4)^2, \\
t &= (p_1 - p_3)^2 = (p_2 - p_4)^2, \\
u &= (p_1 - p_4)^2 = (p_2 - p_3)^2.
\end{aligned}
\tag{1.1}
$$

1.5 Ultra-peripheral collisions

An ultra-peripheral collision (UPC) is defined as a collision, where two projectiles with radii R_A and R_B pass by with an impact parameter b larger then the sum of these radii [23, 24]. A sketch of such collision is shown in Fig. 1.6. Experimental high-energy physics uses projectiles with radius of few femtometres. Because in this case the impact parameter is larger than the range of the strong interactions (their range is around or less than a femtometre) and because the weak and the gravitational interactions are very weak in comparison with other forces, UPC are mediated by electromagnetic interactions. Hence, one can imagine these collisions as an interaction of clouds of virtual photons, which surround our projectiles.

Any charged particle can be used as a projectile for UPC. But the number of surrounding photons depends on the atomic number Z, with the intensity of the interaction growing with Z^2. From this condition one can see the advantage of using heavy-ion collisions for UPC. Nowadays, the physics of UPC is studied at the RHIC and the LHC facilities using a variety of projectiles. In this report we analyse lead-lead collisions at the LHC at an energy of 2.76 TeV per nucleon pair. The goal is two-fold: on the one hand to develop the tools to perform this measurement during Run 2, where we will have many more events at our disposal and the events will be at smaller Bjorken x and on the other hand to evaluate if it is possible to perform this measurement, albeit with large errors, using existing Run 1 data.

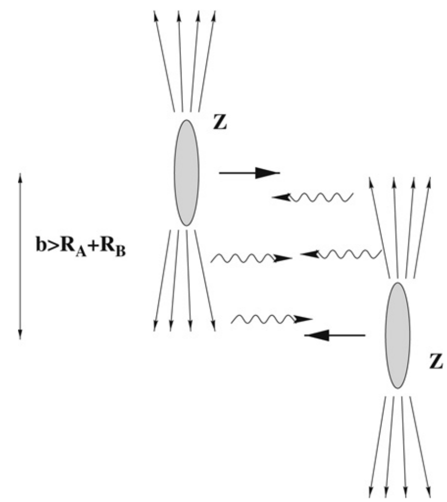

Figure 1.6: A diagram of an ultra-peripheral collision of two ions (proton number Z) with impact parameter b. Taken from Ref. [23].

In general, two types of UPC can occur. One is called photon-photon collision and in this case photons from mother nuclei interact with each other. As a result new particles appear (e.g. $\mu^+\mu^-$ pairs or $q\bar{q}$ pairs). However, due to the law of conservation of total angular momentum the creation of one vector meson cannot happen. For this we need more photons in the interaction or the second type of collision; photon-nucleus collision. A diagram for such process is shown in Fig. 1.7. Here we can see one nucleus, which emits the photon. We interpret the situation in the rest frame of the target nucleus. The photon fluctuates into a virtual $q\bar{q}$ pair. This pair is a colour dipole, which interacts strongly with the second nucleus to produce a vector meson. In this work we are interested in the case of the vector meson being a J/ψ particle. The second nucleus contributes to the momentum for the created J/ψ particle. This contribution comes from the transferred momentum $|t|$ between the initial and final nucleus acting as target. The subject of this thesis is to evaluate the possibility of measuring the cross section of J/ψ photoproduction as a function of $|t|$ at mid-rapidity using the ALICE detector. The integration over $|t|$ of this cross section yields the cross section at mid rapidity.

1.6 Exclusive photoproduction of J/ψ mesons

The exclusive photoproduction of a vector meson is the subject of study of this thesis. We have two types of this production. Coherent one, where the photon interacts coherently with almost all nucleons in nucleus (it couples with the whole nucleus), or incoherent one, where the photon interacts with a single nucleon. In our analyses we can distinguish between these two production types through the use of transverse momentum of the J/ψ, which is related to the transverse size of the target. While the coherent production is characterized by a low momentum ($p_t \approx 60$ MeV/c), the incoherent one is more probable at higher momentum ($p_t \approx 500$ MeV/c) [1]. In the first case, the nuclei usually do not break, but as the electromagnetic fields of lead nuclei are so strong, it is possible that there are other independent soft electromagnetic interactions which

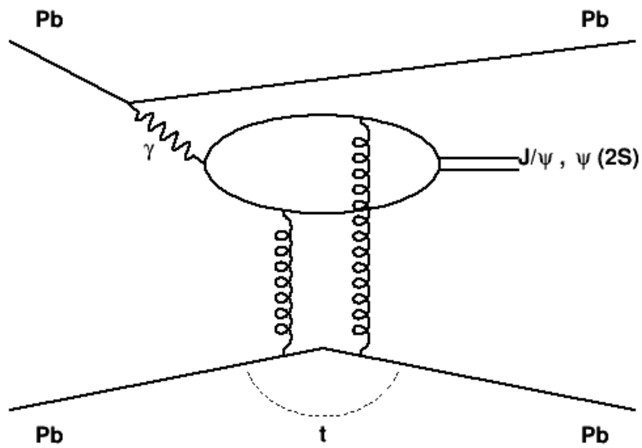

Figure 1.7: A Feynmann diagram of lead-lead ultra-peripheral collision, which produces a J/ψ particle. The t stands for the transferred momentum. The γ is a quasi-real photon emitted from the Pb nucleus.

excite one or both of the nuclei. In the second case the nucleus breaks up and emits forward neutrons which can be measured in so called zero-degree calorimeters.

1.6.1 Models for photonuclear production

There are several models, which can predict the cross section for photonuclear production at LHC energies [15, 23]. All models are based on Eq. 1.2

$$\frac{\mathrm{d}\sigma_{\mathrm{PbPb}}(y)}{\mathrm{d}y} = N_\gamma(y, M)\sigma_{\gamma\mathrm{Pb}}(y) + N_\gamma(-y, M)\sigma_{\gamma\mathrm{Pb}}(-y), \tag{1.2}$$

where N_γ is the photon flux, M is the mass of the produced vector meson, $y = \ln 2k/M$ is the rapidity (with k being the momentum of the photon) and σ_{XY} is the corresponding cross section. Each term in the sum represents one incoming nucleus.

In the semi-classical description [25] the photon flux per unit area can be written as

$$n(k, b) = \frac{\alpha Z^2}{\pi^2 b^2} x^2 \left[K_1^2(x) + \frac{K_0^2(x)}{\gamma}\right], \tag{1.3}$$

with α standing for the fine-structure constant, Z for the electric charge, K_X are Bessel functions and $x = \frac{kb}{\gamma}$. This formula is approximated with the hard sphere model or it is integrated with the convolution of the probability of no hadronic interaction [15] in the models.

The alphabetical summary of the models:

- Using the hard sphere approximation to compute the photon flux
  - **CSS:** A model by Cisek, Schäfer and Szczurek [26]
  - **GM-GDGM:** A model by Goncalves, Machado, Gay-Ducati and Griep [27]
  - **LM:** A model by Lappi and Mantysaari [28]
- Convolution of the flux with the probability of no hadronic interaction
  - **AB-AN** A model by Adeluyi, Bertulani and Nguyen [29]
  - **KN:** A model by Klein and Nystrand [30, 31]
  - **RSZ:** A model by Rebyakov, Strikman and Zhalov [32]

1.6.2 STARlight

One of the Monte Carlo generators we used in this thesis is called STARlight. This generator is using the KN model introduced by Klein and Nystrand. The KN model is based on the vector dominance model (VDM) [33]. In general, the VDM relates the process $\gamma + \mathrm{Pb} \rightarrow \mathrm{V} + \mathrm{Pb}$ to $\mathrm{V} + \mathrm{Pb} \rightarrow \mathrm{V} + \mathrm{Pb}$, where V stands for the vector meson.

The total cross section for nuclei depends on the slope of the $\mathrm{d}\sigma/\mathrm{d}t$ and is dominated by the nuclear form factor $F(t)$ [31]. The photonuclear cross section then can be expressed as

$$\sigma(\gamma + \mathrm{Pb} \rightarrow \mathrm{V} + \mathrm{Pb}) = \left.\frac{\mathrm{d}\sigma(\gamma + \mathrm{Pb} \rightarrow \mathrm{V} + \mathrm{Pb})}{\mathrm{d}t}\right|_{t=0} \int_{t_{min}}^{\infty} \mathrm{d}t |F(t)|^2. \tag{1.4}$$

Making use of the optical theorem and the eikonalization technique [15] we can find the cross section related to the nuclei as

$$\left.\frac{\mathrm{d}\sigma(\gamma + \mathrm{Pb} \rightarrow \mathrm{V} + \mathrm{Pb})}{\mathrm{d}t}\right|_{t=0} = \frac{\alpha \sigma_{tot}^2 (\mathrm{V} + \mathrm{Pb})}{4 f_v^2}. \tag{1.5}$$

Here the f_v is the vector meson-photon coupling. From a classical Glauber model [34]

$$\sigma_{tot} (\mathrm{V} + \mathrm{Pb}) = \int \mathrm{d}^2 b \left(1 - e^{[-\sigma_{tot}(\mathrm{V}+\mathrm{p}) T_{\mathrm{Pb}}(b)]}\right), \tag{1.6}$$

where T_{Pb} is the nuclear thickness function, b is the impact parameter and for $\sigma_{tot}^2 (\mathrm{V} + \mathrm{p})$ we make use of the optical theorem at the nucleon level

$$\sigma_{tot}^2 (\mathrm{V} + \mathrm{p}) = 16\pi \left.\frac{\mathrm{d}\sigma(\mathrm{V} + \mathrm{p} \rightarrow \mathrm{V} + \mathrm{p})}{\mathrm{d}t}\right|_{t=0}. \tag{1.7}$$

Using VDM leads to

$$\left.\frac{\mathrm{d}\sigma(\mathrm{V} + \mathrm{p} \rightarrow \mathrm{V} + \mathrm{p})}{\mathrm{d}t}\right|_{t=0} = \frac{f_V^2}{4\pi\alpha} \left.\frac{\mathrm{d}\sigma(\gamma + \mathrm{p} \rightarrow \mathrm{V} + \mathrm{p})}{\mathrm{d}t}\right|_{t=0}, \tag{1.8}$$

where the elementary cross section can be parametrized with the results from the measurement made at HERA [35]

$$\left.\frac{\mathrm{d}\sigma(\gamma+\mathrm{p}\rightarrow\mathrm{V}+\mathrm{p})}{\mathrm{d}t}\right|_{t=0} = b_V(XW^{\epsilon}+YW^{-\eta}), \tag{1.9}$$

where W is the centre-of-mass energy and the rest are constants, which were determined from fits to data and can be found in Table II in [31]. The first term with X represents the pomeron exchange and the Y is the meson exchange.

STARlight takes the form factor as the Woods-Saxon distribution approximated as a convolution of a hard sphere and a Yukawa potential. Then the form factor looks like

$$F(q=\sqrt{|t|}) = \frac{4\pi\rho_0}{Aq^3}[\frac{\sin(qR_A)-qR_A\cos(qR_A)}{1+a^2q^2}], \tag{1.10}$$

where A is the atomic number, ρ_0 is the nuclear density of the hard sphere, R_A is the radius of the nucleus and a is the range of the Yukawa potential. STARlight takes as input numbers $a = 0.7$ fm and $R_A = 6.62$ fm [30].

Putting all things together the photonuclear cross section we are using has the form

$$\frac{\mathrm{d}\sigma(\gamma+\mathrm{Pb}\rightarrow\mathrm{V}+\mathrm{Pb})}{\mathrm{d}t} = \mathrm{NORM}|F(t)|^2 \tag{1.11}$$

with NORM stands for the normalization of the fit function used later in this work.

Another option is to neglect the range of the interaction and use as a form factor the exponential function

$$F(t) = Ce^{\lambda|t|}, \tag{1.12}$$

where λ corresponds to a transversal nuclear size as $\lambda = \frac{1}{2}R^2$ and C is the normalization.

1.7 Previous work

The cross section dependence on y of the Run 1 data was already measured by the ALICE Collaboration [1, 2, 3]. The paper [1] focuses on the production of charmonium and e^+e^- pairs at mid-rapidity in UPC. They measured $\mathrm{d}\sigma^{\mathrm{coh}}_{\mathrm{J}/\psi}/\mathrm{d}y = 2.38^{+0.34}_{-0.24}$(sta+sys) mb for coherent J/ψ production in the rapidity interval -0.9 $< y <$ 0.9 The result is compared to the models in Fig. 1.8. This thesis extends this result adding the measurement of the $|t|$ of the cross section. In this section we pinpoint major partial results of the paper, which can be used to compare with our preliminary results, which will be explained later in our work.

1.7.1 Selection criteria

In Tab. 1.3 we have partial results of cuts applied on data. Most of them are self-explanatory, but we should definitely mention V0 offline, which rejects every event with some deposited energy in the V0 detector and the selection criteria on muons, which was done using the average of the muon $\mathrm{d}E/\mathrm{d}x$ and considering as muons the particles within 3 sigma.

Selection	**Events**
Triggered events	6 507 692
$1 \leq N_{\mathrm{TRK}} \leq 10$	2 311 056
Primary vertex	1 972 231
Two reconstructed tracks	436 720
$\max(p_t^1,p_t^2) > 1$ GeV/c	46 324
V0 offline	46 183
dE/dx consistent with muon	45 518
Opposite charge	31 529
Mass $\in$ [2.2;6.0] GeV/c^2	4 542

Table 1.3: Number of selected events in the paper (see subsection 1.7.1). Taken from Ref. [1].

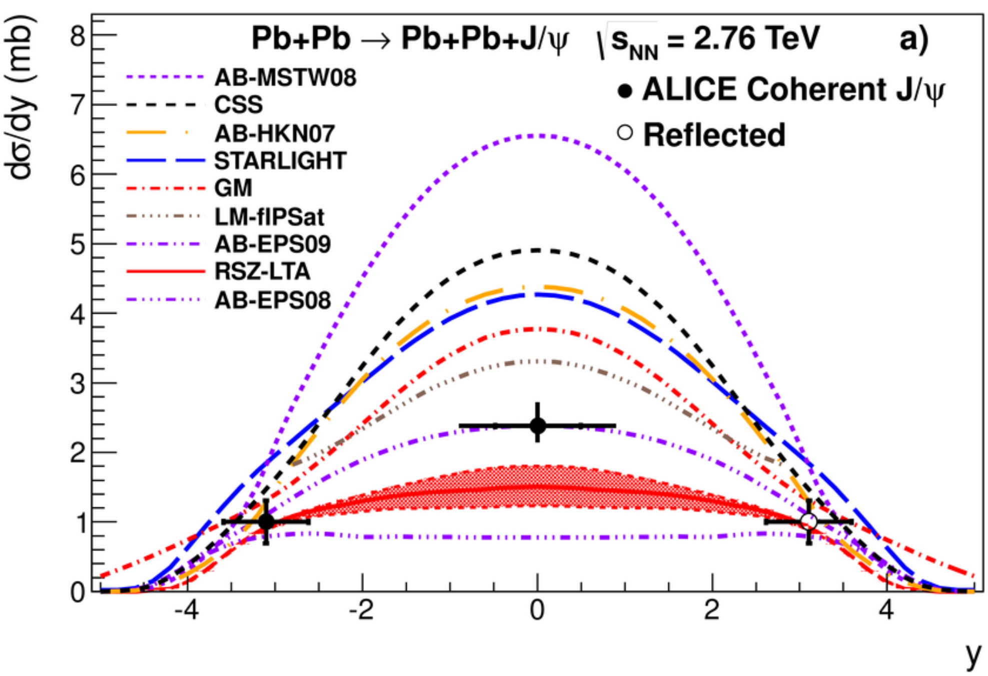

Figure 1.8: Measured differential cross section of J/ψ photoproduction in UPC compared to the theoretical calculations. The error is the quadratic sum of the statistical and systematic errors. Taken from Ref. [1].

1.7.2 Detector and physics corrections

Corrections on detector effects were computed using STARlight simulations. They applied mentioned selection criteria on reconstructed tracks and an additional cut on the transverse momentum of the J/ψ candidates $p_t < 200$ GeV/c ($p_t > 300$ GeV/c) for coherent (incoherent) samples. The average acceptance $\times$ efficiency was 4.57% (3.19%). The correction on incoherent production f_I was computed to be 0.044 ± 0.014 for di-muons. The correction on feed-down was estimated to be $0.10^{+0.05}_{-0.06}$.

1.7.3 J/ψ yield

In the quoted paper the authors claim to have 291$\pm$18(sta)$\pm$4(sys) J/ψ candidates. This number was obtained from a Crystal-Ball fit of the invariant mass spectrum. Applying physics corrections on this yield they ended up with 255$\pm$16(sta)$^{+14}_{-13}$(sys) coherent J/ψ mesons decayed to two muons with opposite charge.

Chapter 2

ALICE experiment

The Large Hadron Collider (LHC) is a scientific facility located beneath the France-Switzerland border near Geneva, Switzerland. Its circumference of 27 kilometres granted it the title of the largest particle collider in the world. It was built to accelerate protons and lead ions to relativistic energies and to collide them at four crossings, where the four main LHC experiments are situated - ALICE, ATLAS, CMS and LHCb.

From its start in 2009 to a pause in 2013 it produced a huge amount of proton-proton, proton-lead and lead-lead collisions. This period is called Run 1. After it, an almost two-year Long Shutdown 1 proceeded to give engineers an opportunity to upgrade systems and prepare the collider to deliver higher energy and luminosity. At the beginning of 2015 an ongoing period called Run 2 was started and the LHC established a new world record in the energy of collided particles to 13 TeV for p-p and 5.02 TeV per nucleon pair for Pb-Pb collisions. Later this year new p-Pb collisions are expected. The energy at which these collisions will take place has not been decided yet.

2.1 ALICE experiment

One of the experiments, which is using the LHC machine, is the ALICE experiment [36]. In contrast to the other experiments, this one was designed to look for the state of matter called quark gluon plasma (QGP) and to measure some of its properties. Because one needs large volumes with high energy densities to create the QGP, beams of lead ions are used at the LHC. As it is mentioned in Sec. 1.5, for UPC we are using these beams of lead ions. The ALICE detector consists of 18 sub-detectors (See Fig. 2.1). For the UPC trigger we will need only AD (in Run 2), TOF, V0 and ITS, while the measurement will require ITS, TPC, V0, AD (in Run 2) and ZDC.

2.1.1 Inner Tracking System

The Inner Tracking System (ITS) is located in the central part of ALICE. Its main tasks are to localize the primary and secondary vertices, to track and identify particles with low momentum and reconstruct particles traversing dead regions of the main tracking detector - the TPC. The ITS itself is a silicon based detector and it is divided in three layers each consisting of two cylinders of detectors using different technologies: SPD, SDD and SSD.

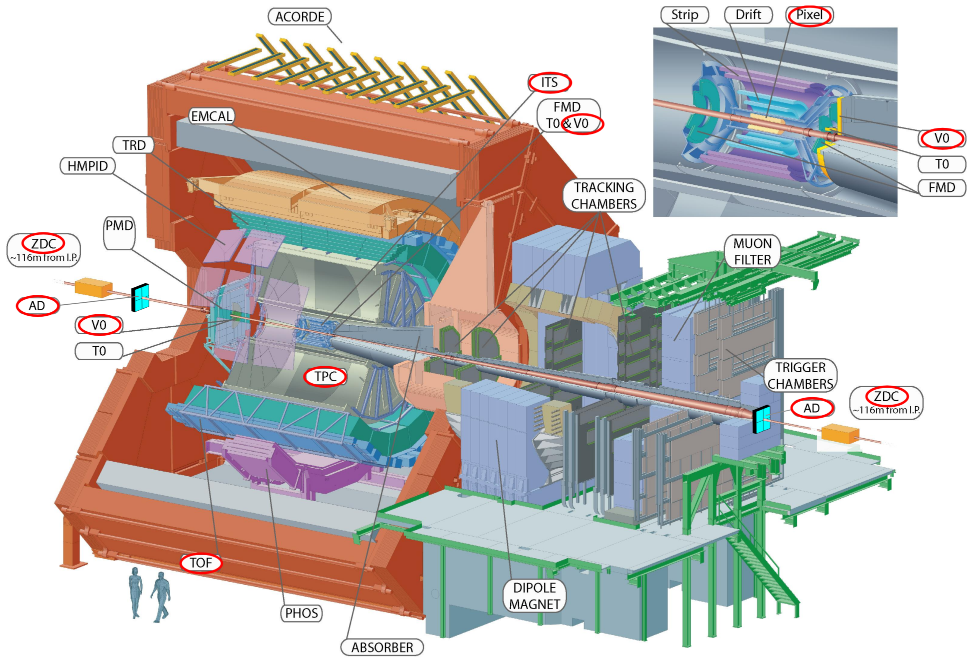

Figure 2.1: Scheme of the ALICE detector. Detectors used for UPC triggering at mid-rapidity and analysis are in the red ellipsis. Taken from Ref. [36].

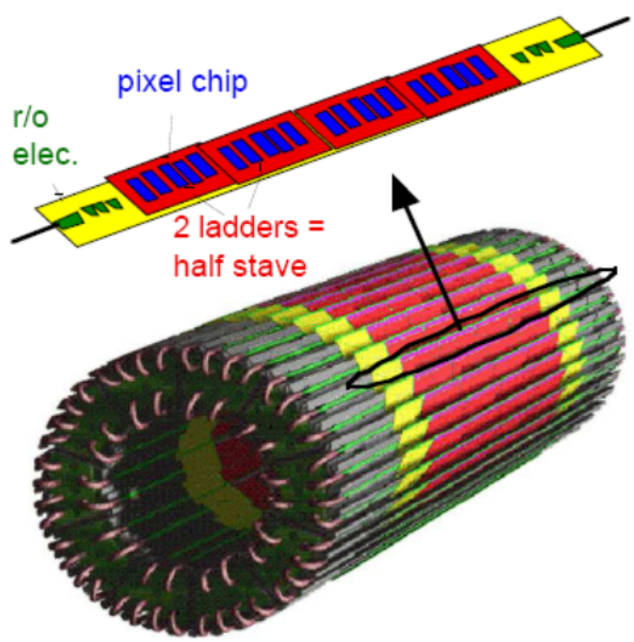

Figure 2.2: Scheme of the SPD subdetector. Taken from Ref. [36].

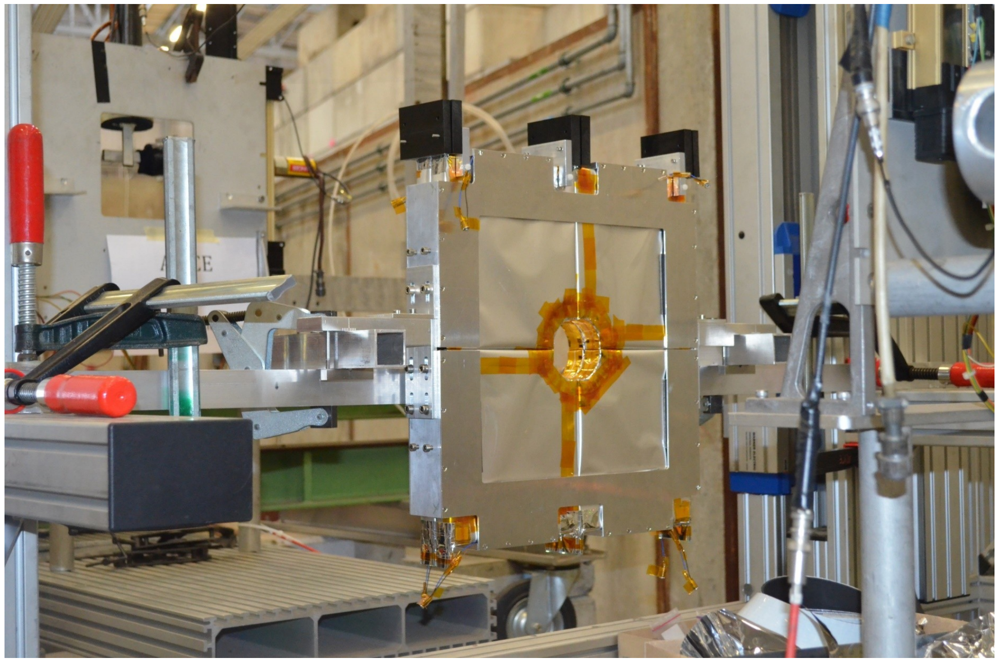

Figure 2.3: A prototype of the AD detector. Taken from Ref. [37].

For triggering purpose we need only SPD, where the abbreviation stands for the Silicon Pixel Detector. This is the innermost layer of the ITS. A sketch of the SPD is in Fig. 2.2. The SPD itself consists of the inner and outer layer, which are divided in so-called staves in the azimuthal angle. The inner (outer) layer has 20 (40) staves. Each stave is made of 4 ladders. Each ladder has 5 pixel chips and each of them contains 8192 readout cells. Together we have 1200 active chips in the SPD.

The SPD is 282 mm long in the direction of the beam and 39 (76) mm in the radius of the inner (outer) layer. A chip has a size of 13.5 mm with an average spacing of 0.6 mm.

2.1.2 Time Projection Chamber

The Time Projection Chamber (TPC) is another central barrel detector which is placed right after the ITS in radial distance. Its main purpose is to track particles and provide charged-particle momentum measurements with good two-track separation, vertex determination and particle identification. The TPC coverage in pseudo-rapidity is -0.9< η <0.9 for tracks with full radial length and in azimuth it has full coverage. It offers good momentum resolution in a large p_t range from 0.1 GeV/c to 100 GeV/c.

The TPC has a cylindrical shape. Its active volume goes from 848 mm to 2466 mm in radius and 5000 mm along the beam direction. It is split in 2 chambers in radius and each is divided into 18 sectors in azimuth. In addition, the TPC is split up in the middle by a central electrode (positioned vertically). Together it gives 72 chambers, which are read out on both ends of the detector.

The TPC is a gaseous detector filled with a mixture of neon and carbon oxide in Run 1 and a mixture of argon and carbon oxide in Run 2. When a particle propagates through the gas mixture, it ionizes its surroundings. Because this happens in an electric field, ionized particles drift to electrodes at both ends of the detector, where charge is collected. Crucial here is the drift speed, which for the neon mixture is $\sim$90 μs. Our speed of data collecting is then limited by the drift speed, so when the interaction rate is large, we will have a new event in the TPC in the moment, when the old one is still not read. Also the charge particle multiplicity density increases with an energy of collision, which makes the operation of the detector in Run 2 more difficult.

2.1.3 Time-Of-Flight detector

The Time-Of-Flight (TOF) detector is a gaseous detector which covers the central pseudo-rapidity region for particle identification in the intermediate momentum range and helps ITS and TPC to track low momentum particles. The TOF is built of the Multi-gap Resistive-Plate Chambers (MRPC) [38]. The advantage of this method is the high, uniform electric field over the full volume. A traversing charged particle causes a gas avalanche process and therefore we are not dealing with the drift time any more.

The TOF has a length of 741 cm and an internal (external) radius of 370 (399) cm. This is divided in 18 sectors in azimuthal angle and 5 segments in the beam direction.

2.1.4 V0 detector

The V0 is a scintillator based detector, which is made of two counters V0A and V0C installed on both sides of the ALICE detector. Its purpose is to measure particles in the forward region (particles, which left the interaction point under a small angle). V0A (V0C) is located 340 (90) cm on the side heading to the ATLAS (CMS) cavern. It covers the pseudo-rapidity range $2.8< \eta <5.1$ ($-3.7< \eta <-1.7$).

The V0 is the most frequently used detector for triggering. Since it consists of two parts, it can work in two modes - AND and OR. The AND mode is used for example for the Minimum Bias trigger. For the UPC photoprodution in mid-rapidity we negate the OR mode, because we want to have nothing in any of the V0 arrays - if there is something in V0A or V0C, the event does not trigger the readout detectors.

2.1.5 ZDC detector

The Zero Degree Calorimeter (ZDC) is a forward detector designed to detect spectator nucleons, which can be used to calculate the number of participants in a collision. It can also tell us about the centrality of a collision, which can be used for triggering particular centrality classes of events.

The ZDC is made of 2 sets of hadronic scintillators located 116 meters on each side of the interaction point. The sets are made of two calorimeters, where the ZN (ZP) is situated between (outside) the beam pipes and measures neutrons (protons). The protons feel the magnetic fields of the LHC and deviate, while the neutrons fly at zero degrees. In addition, electromagnetic calorimeters ZEM are placed 7 meters from the interaction point on both sides. These help to distinguish between very central and very peripheral events, where the signal in ZN is very similar.

2.1.6 AD detector

The ALICE Diffractive detector (AD) is another system installed in the forward pseudo-rapidity region of ALICE [39]. The system itself consists of 2 scintillator stations situated in 2 different places. The stations are called according to the side they are located as ADA and ADC. The ADA (ADC) is 16 (19) metres from the interaction point and covers the pseudo-rapidity range $4.8 < \eta < 6.3$ ($-7.0 < \eta < -4.9$).

This subdetector was added to ALICE during the Long Shutdown 1 and it was commissioned during p-p collisions of Run 2. In Run 1, the forward detectors were able to select about 30% of single diffractive events. With AD the selection significantly improves for diffracted mass below 10 GeV/c^2 [37]. For UPC this new detector system means that the capabilities to veto the presence of particles is increased substantially and thus we expect even less background when using the AD system.

2.2 UPC triggers

The LHC is designed to collide projectiles with a frequency of 40 MHz for protons and $\sim$ 8 MHz for ion beams [40]. However, the ALICE detectors need some time to read out electrical signals, which is in order of μs. Therefore we cannot save every single event, but we have to carefully pick the events, which have signs for the physics we are interested in. This is done with a so-called trigger. The ALICE trigger system is briefly described in Sec. 5.3.2.

For ultra-peripheral collisions at mid-rapidity during Run 1 we used the detectors SPD, TOF and V0 to build trigger signals. We were using the so-called UPC trigger CCUP4 to collect data in 2011 collisions, which focused on the photoproduction of the J/ψ. This trigger consists of the following conditions:

- **!V0$_{\mathbf{OR}}$:** Nothing was detected in the V0 detector,
- **0OMU:** More than 1 hit and less than 7 hits in the TOF detector + at least two of the hits with an opening angle $> 150°$,
- **0SM2:** More than 1 hit in the outer layer of the SPD.

Data collected in 2015 used the trigger called CCUP8 to retrieve events with photoproduction of the J/ψ. This trigger already uses the new AD detector and has slightly different conditions and higher performance with respect to the CCUP4 trigger. The conditions are:

- **!0VB$_{\mathbf{OR}}$:** Nothing was detected in the V0 detector,
- **!0UB$_{\mathbf{OR}}$:** Nothing was detected in the AD detector,
- **0STP:** More than 1 hit and less then 7 hits in the SPD detector + opening angle $> 153°$,
- **0OMU:** More than 1 hit and less than 7 hits in the TOF detector + at least two of the hits with an opening angle $> 150°$.

2.3 Data flow

The extraction of data from a collision to a tree ready for an analysis is a rather long process. When two lead ions collide a selection starts with online triggers. The UPC triggers are described in Sec. 2.2. Only a small portion of events passes these criteria not just because of the physical condition, but also due to an occupancy of the readout detectors for example. In fact, there are several trigger levels. When a positive decision is made, detector signals are stored as RAW data in the ALICE clusters, where the data are compressed. Detector settings are saved as well. These settings are then used to reconstruct physics events from the RAW data, which are stored again at so-called ESD level. The last step is to use physics selection on the ESD data, which rejects some background and focus on interesting physics signatures. These data are called AOD and are further used to create objects, which can be used in an analysis. In our case, this last step of the process takes the form of a file with ROOT trees and histograms [41], which is produced by the official LEGO train of the PWG-UD [42].

Chapter 3

Analysis of Run 1 data

In this chapter we describe all technical aspects needed for the analysis of Run 1 data. The results of the analysis are presented in next chapter.

3.1 Experimental cross section

A cross section is related to the probability of occurrence of a particular event per unit of area. In particle physics it is usually meant as a measure of the probability of interaction between two particles. In this thesis we study the dependence of the cross section on rapidity y and t for the reaction

$$\mathrm{Pb} + \mathrm{Pb} \rightarrow \mathrm{Pb} + \mathrm{Pb} + \mathrm{J}/\psi.$$

As we discussed above, this process describes an interaction with a photon, therefore we speak about photoproduction.

The coherent J/ψ differential cross section, which can be obtained from the measured data, is for one bin in p_t^2 and a given rapidity range Δy given by

$$\frac{\partial^2 \sigma^{\mathrm{coh}}_{\mathrm{J}/\psi}}{\partial y \partial p_t^2} = \frac{N^{\mathrm{coh}}_{\mathrm{J}/\psi}}{(\mathrm{Acc} \times \epsilon)^{\mathrm{coh}}_{\mathrm{J}/\psi} \cdot BR(\mathrm{J}/\psi \rightarrow \mu^+\mu^-) \cdot \mathscr{L}_{int} \cdot \Delta p_t^2 \cdot \Delta y}, \tag{3.1}$$

where $(\mathrm{Acc} \times \epsilon)^{\mathrm{coh}}_{\mathrm{J}/\psi}$ is the correction on detector effects, $BR(\mathrm{J}/\psi \rightarrow \mu^+\mu^-)$ is the branching ratio ($(5.961 \pm 0.033)\%$ according to [19]), $\mathscr{L}_{int}$ is the total integrated luminosity of UPC triggers, which was $22.4^{+0.9}_{-1.2}$ $\mu\mathrm{b}^{-1}$ [43], Δp_t^2 is the size of the bin and finally, $N^{\mathrm{coh}}_{\mathrm{J}/\psi}$ is the number of coherent J/ψ candidates. The last introduced variable can be obtained from Eq. 3.2, where N_{yield} is the number of candidates obtained from the fit of the mass spectra using a Crystal-Ball function, f_I is the fraction of the incoherent production of J/ψ and f_D is the fraction of events, where the J/ψ was produced from the decay of the heavier resonance of the $c\bar{c}$ pair, $\psi(2\mathrm{S})$.

$$N^{\mathrm{coh}}_{\mathrm{J}/\psi} = \frac{N_{yield}}{1 + f_I + f_D}. \tag{3.2}$$

The influence of the incoherent production can be calculated as

$$f_I = \frac{{}^{\mathrm{gen}}N^{\mathrm{inc}}_{\mathrm{J}/\psi}}{{}^{\mathrm{gen}}N^{\mathrm{coh}}_{\mathrm{J}/\psi}} = \frac{\sigma^{\mathrm{inc}}}{\sigma^{\mathrm{coh}}} \cdot \frac{(\mathrm{Acc} \times \epsilon)^{\mathrm{inc}}_{\mathrm{J}/\psi}}{(\mathrm{Acc} \times \epsilon)^{\mathrm{coh}}_{\mathrm{J}/\psi}} \cdot \frac{BR(\mathrm{J}/\psi \rightarrow \mu^+\mu^-)}{BR(\mathrm{J}/\psi \rightarrow \mu^+\mu^-)}, \tag{3.3}$$

where the cross sections σ^{x} are obtained from STARlight as well as the corrections on the detector effects and numbers of generated particles ${}_{\mathrm{gen}}N_Y^X$. In our analysis we will work with several bins in p_t^2. Therefore we will rewrite Eq. 3.3 into the form (we take just the numerator as an example)

$$ {}^{\mathrm{bin}}_{\mathrm{gen}}N^{\mathrm{inc}}_{\mathrm{J}/\psi} = \sigma^{\mathrm{inc}}_{\mathrm{bin}} \cdot (\mathrm{Acc} \times \epsilon)^{\mathrm{inc}}_{\mathrm{bin}} = \frac{{}_{\mathrm{gen}}N^{\mathrm{inc}}_{\mathrm{bin}}}{{}_{\mathrm{gen}}N^{\mathrm{inc}}_{\mathrm{all}}} \sigma^{\mathrm{inc}}_{\mathrm{tot}} \cdot (\mathrm{Acc} \times \epsilon)^{\mathrm{inc}}_{\mathrm{bin}}. \tag{3.4} $$

The J/ψ is not the only charmonium produced. Another visible resonance is $\psi(2\mathrm{S})$ (see Fig. 1.3), which decay to J/ψ with $BR(\psi(2\mathrm{S}) \to \mathrm{J}/\psi + \pi^+\pi^-) = (34.46 \pm 0.30)\%$ [19]. If the pions are not detected for some reason this decay would mimic the signature we are looking for. This effect (called feed-down) is introduced to the Eq. 3.2 as f_D and can be calculated similarly as

$$ f_D = \frac{{}_{\mathrm{gen}}N^{\mathrm{coh}}_{\psi(2\mathrm{S})}}{{}_{\mathrm{gen}}N^{\mathrm{coh}}_{\mathrm{J}/\psi}} = \frac{\sigma^{\mathrm{coh}}_{\psi(2\mathrm{S})}}{\sigma^{\mathrm{coh}}_{\mathrm{J}/\psi}} \cdot \frac{(\mathrm{Acc} \times \epsilon)^{\mathrm{coh}}_{\psi(2\mathrm{S})}}{(\mathrm{Acc} \times \epsilon)^{\mathrm{coh}}_{\mathrm{J}/\psi}} \cdot \frac{BR(\psi(2\mathrm{S}) \to \mathrm{J}/\psi + \pi^+\pi^-) \cdot BR(\mathrm{J}/\psi \to \mu^+\mu^-)}{BR(\mathrm{J}/\psi \to \mu^+\mu^-)}, \tag{3.5} $$

where the cross section fraction can be rewritten as

$$ \frac{\sigma^{\mathrm{coh}}_{\psi(2\mathrm{S})}}{\sigma^{\mathrm{coh}}_{\mathrm{J}/\psi}} = \frac{{}^{\mathrm{bin}}_{\mathrm{gen}}N^{\mathrm{coh}}_{\psi(2\mathrm{S})} / {}^{\mathrm{all}}_{\mathrm{gen}}N^{\mathrm{coh}}_{\psi(2\mathrm{S})}}{{}^{\mathrm{bin}}_{\mathrm{gen}}N^{\mathrm{coh}}_{\mathrm{J}/\psi} / {}^{\mathrm{all}}_{\mathrm{gen}}N^{\mathrm{coh}}_{\mathrm{J}/\psi}} \cdot \frac{\sigma^{\mathrm{tot}}_{\psi(2\mathrm{S})}}{\sigma^{\mathrm{tot}}_{\mathrm{J}/\psi}}. \tag{3.6} $$

From the number of $\psi(2\mathrm{S})$ we are interested only in those, which decays through J/ψ, so we multiply this number with the corresponding branching ratio. In addition the fraction of BRs of decays of both vector mesons to two muons has to be included and we finish with the equation

$$ f_D = \frac{{}^{\mathrm{bin}}_{\mathrm{gen}}N^{\mathrm{coh}}_{\psi(2\mathrm{S})}}{{}^{\mathrm{bin}}_{\mathrm{gen}}N^{\mathrm{coh}}_{\mathrm{J}/\psi}} \cdot \frac{{}^{\mathrm{all}}_{\mathrm{gen}}N^{\mathrm{coh}}_{\mathrm{J}/\psi}}{{}^{\mathrm{all}}_{\mathrm{gen}}N^{\mathrm{coh}}_{\psi(2\mathrm{S})}} \cdot \frac{(\mathrm{Acc} \times \epsilon)^{\mathrm{coh}}_{\psi(2\mathrm{S})}}{(\mathrm{Acc} \times \epsilon)^{\mathrm{coh}}_{\mathrm{J}/\psi}} \cdot \frac{\sigma^{\mathrm{tot}}_{\psi(2\mathrm{S})}}{\sigma^{\mathrm{tot}}_{\mathrm{J}/\psi}} \cdot BR(\psi(2\mathrm{S}) \to \mathrm{J}/\psi + \pi^+\pi^-). \tag{3.7} $$

In principle we should have use the decays $\psi(2\mathrm{S}) \to \mathrm{J}/\psi$+ANYTHING, but at the moment of doing the analysis for this thesis we did not have access to the right simulated MC. This will be corrected for the final measurement.

To measure the dependence on $|t|$ we have to use the correction on the photon momentum η_{SL} in Eq. 3.1 as in Eq. 3.8

$$ \frac{\partial^2 \sigma^{\mathrm{coh}}_{\mathrm{J}/\psi}}{\partial y \partial t} = \frac{1}{\eta_{SL}} \cdot \frac{\partial^2 \sigma^{\mathrm{coh}}_{\mathrm{J}/\psi}}{\partial y \partial p_t^2}. \tag{3.8} $$

This correction is needed, because $|t|$ is only approximated by p_t^2. The precision of this approximation depends on the average p_t of the quasi-real photon in a given $|t|$ interval and it is strongly dependent on $|t|$. This will be shown later on in this thesis.

3.2 Analysis

To study the cross section of production of a vector meson in UPC we have to choose good data. An opportunity to measure such events at nowadays highest energy possible (at the LHC facility) appeared in 2011. That year several runs with Pb-Pb collisions had active triggers for ultra-peripheral collisions. The data we analyse were prepared using the LEGO train framework of the PWG-UD. Specifically we used the AOD train PWGUD/UD_PbPb_AOD/75_20160322-1524. The LEGO train ran over 6 610 590 CCUP4 triggers (the exact list of runs can be found in the page corresponding to this train) and made a first pre-selection of events with only two tracks. The requirements for the tracks were quite relaxed and were strengthen by the selection described below. The output ROOT file contains a tree with 1 189 614 pre-selected events.

Besides these data also Monte Carlo simulations (MC) were used. Three different processes were simulated. The channel with a di-muon pair coming from the J/ψ decay (J/$\psi \rightarrow \mu^+\mu^-$) was generated twice. Once for the coherent production of J/ψ and once for the incoherent production of J/ψ. Another channel that was simulated corresponds to the reaction of two photons producing two muons ($\gamma\gamma \rightarrow \mu^+\mu^-$). This process represents the main irreducible background to our measurement. The last simulated channel is the decay of the ψ(2S) meson to pions and muons ($\psi(2S) \rightarrow \mu^+\mu^-\pi^+\pi^-$). In this case only the coherent production was simulated.

The MC productions have the ALICE labels (in mentioned order) LHC12a19a, LHC12a19b, LHC12a19f and LHC14b1d.

3.2.1 Data selection

In order to find out the right events for the measurement, we had to apply additional selection criteria. We used three different types of selections. For measured data we used the following cuts:

- the event has been triggered with CCUP4,
- it has exactly two good tracks reconstructed,
- the criteria for a good track are the following:
  - the track exists,
  - filter bit 0 set,
  - the track has been refitted with the TPC and the ITS,
  - the track in TPC has at least 50 clusters,
  - it has at most a χ^2 of 2 per degree of freedom,
  - it has at least a point in the SPD;
- at least one track has $p_t > 1$ GeV/c,
- there is nothing in the V0 according to the offline processing,
- the muon identification made by the TPC in units of significance σ for both particles fulfills the condition $4 > \sqrt{\sigma^2_{\text{track1}} + \sigma^2_{\text{track2}}}$,
- the tracks have opposite charge,
- the invariant mass is between 2.2 GeV and 6.0 GeV,
- $p_t^{\mu\mu} < 0.11$ GeV/c,
- the energy in each neutron ZDC < 8000 GeV.

Selection	**Events**
Trigger CCUP4	6 610 590
Pre-selected data	1 189 614
2 reconstructed good tracks	1 175 664
max(p_t^1,p_t^2)$>$ 1 GeV/c	135 446
V0	64 390
Muon PID	54 483
Opposite charge	35 697
Mass $\in$ (2.2;6.0) GeV/c^2	4 473
$p_t < 0.11$ GeV/c	1 557
ZNA and ZNC $<$ 8000 GeV	1 390

Table 3.1: Number of selected events after the application of each criterion for measured data.

The reasons for the application of each criterion are straightforward. We will mention only the condition for the cut of transverse momentum, which exclude the region where diffraction peaks in the coherent production appear according to the STARlight and the cut on ZDC energy, which ensures that not more than 6 neutrons were detected. The impact of these criteria on the number of events can be found in Tab. 3.1. After the cut on mass we have 4 473 events. This number is compatible with the number of events obtained in the published analysis shown in Tab. 1.3

For MC simulations we have two different selection criteria. One for generated particles and the second one for reconstructed particles. For the generated sample we used these criteria:

- at least 2 generated particles,
- rapidity of $\mu^+\mu^-$ is within (-0.9,0.9).

The last selection criteria were used for MC reconstructed particles and are listed here:

- application of the same selection criteria as for generated particles,
- application of the same selection criteria as for measured data.

As one can see, they are composed of criteria introduced before. Because we want to use the MC simulation to compute the correction for acceptance and efficiency of the detector, we had to inherit the same selection criteria as for measured data. The impact of these selection processes on the number of events are in Tab. 3.2 and 3.3. It is important to mention (and it can be seen in Tab. 3.3), that the output ROOT files of MC productions do not contain information about the trigger. We will come to this issue later on.

We have to note, that the number of events in the MC Coherent sample differs from the incoherent and background ones. In fact, these numbers have only informational character and we will not use all of them here.

Selection	**Events**
Pre-selected data	1 382 193
2 generated particles	1 381 792
Rapidity $\in$ (-0.9;0.9)	1 249 819

Table 3.2: Number of selected events after the application of each criterion for MC Coherent sample - generated particles.

Selection	**Events**
Pre-selected data	1 382 193
Criteria for generated particles	1 249 819
Trigger CCUP4	1 249 819
2 reconstructed good tracks	168 783
max(p_t^1,p_t^2)$>$ 1 GeV/c	168 783
V0	168 738
Muon PID	166 770
Opposite charge	166 769
Mass $\in$ (2.2;6.0) GeV/c^2	166 768
p_t $<$ 0.11 GeV/c	155 732
ZNA and ZNC $<$ 8000 GeV	155 732

Table 3.3: Number of selected events after the application of each criterion for MC Coherent sample - reconstructed particles.

3.3 Work-flow

In this paragraph we will briefly describe each part of the analysis we did. The conclusion and results of the analysis will be presented in the next chapter.

3.3.1 Basic plots

In the beginning of our analysis we had to decide, which selection criteria we will use. For this reason it is crucial to study some basic distributions. Our main goal is to study the J/ψ particle, so we have to select a mass range of our data. For this we looked at the mass distributions. As an example of this, here we only show the main distributions that we studied. These can be found in Figs. 3.1 and 3.2. In Fig. 3.1 one can see the di-muon distribution for measured data. There is a strong peak around 3.1 GeV/c^2 which is considered to be a sign of J/ψ particles. But there is also background which we have to understand. The other channels have information about generated particles, in other words the input parameters for our simulations. In Fig. 3.2 we show already processed data. For measured data it means that cuts on mass and p_t were applied. The MC data show reconstructed particles. With reconstructed particles we mean data, which would be collected by the ALICE detector. Therefore a "J/ψ peak" for coherent and incoherent sample change its shape from a sort of delta function at the generated level to a Gaussian distribution at the simulated reconstructed level.

The next quantity we focused on is the transverse momentum, displayed in Figs. 3.3 and 3.4. The first interesting thing in Fig. 3.3 is the top right panel, where the sample of the coherent production of J/ψ particles is shown. This process displays a strong diffraction pattern, which is an unwanted effect for the studies we wanted to perform, because it produces structures in the efficiency distributions. Methods, how to deal with this problem, exist, but due to low statistics for coherent production at larger $|t|$ and the stronger contribution from incoherent production in this region we are more interested in low p_t and therefore we added the p_t cut in our selection criteria. One more thing we can obtain from Fig. 3.3 is the fact, that our measured data actually are the sum of all three MC samples. In Fig. 3.4 we present the measured data with p_t cut. The transverse momenta of all mentioned processes populate this p_t region. Therefore we have to be careful, extract the background in further analysis and remember effects of remaining events from these processes during an interpretation of our results.

At last we have the main goal of our study - transferred momentum $|t|$. Neglecting the momentum of the photon in Fig. 1.7 we can replace $|t|$ with the transverse momentum squared of the J/ψ. Appropriate plots are in Fig. 3.5 and 3.6. Those are the data we want to use. The left top panel of Fig. 3.6 are our measured data before the subtraction of background. Now we have around 454 events which should decrease a little bit. This predicts, that the final measurement will have a substantial statistical error, once this sample is separated in 5 $|t|$ bins.

3.3.2 Acceptance $\times$ efficiency procedure

As it was pointed before the reason why we have Monte Carlo simulations is to have samples with larger statistics, where we can test our methods. Our MC data are divided in two groups - generated particles and reconstructed particles. Because we want to correct our measured data for imperfect efficiency of our detector, we have to somewhat compare these two groups.

The acceptance × efficiency is a simple procedure, where we divide the p_t^2 distribution of reconstructed particles by the p_t^2 distribution of generated particles. Applying this ratio to our measured data we should get back the corrected distribution.

In our analysis we follow quite straightforward steps. Both distributions had to undergo the selection criteria mentioned above. Then a new histogram is made. And finally, a fraction of both distributions is stored in it to be used later on to correct the data.

3.3.3 Taking into account photon momentum

In theory in Sec. 3.1 we are talking about obtaining the dependence of the cross section on the transferred momentum of the lead projectile $|t|$. What we have actually measured is the ${}_{\mathrm{J}/\psi}p_t^2$ of the J/ψ particle, which originates from the process shown in Fig. 1.7. There one can see, that ${}_{\mathrm{J}/\psi}p_t^2$ is a sum of $|t|$ and ${}_{\gamma}p_t^2$, where the second corresponds to the transverse momentum squared of the quasi-real photon.

To study, if the momentum of the photon is negligible, we had to understand the tool, which was used to create our simulations - STARlight, mentioned in Sec. 1.6.2. STARlight itself proceeds as follow: First, it generates the momenta of the photon and the so-called pomeron (represented by the two gluons in Fig. 1.7) which mediates the strong interaction, and then it calculates the momentum of the created J/ψ.

To correct our measurement from a p_t^2- to a $|t|$-dependence we have simulated the coherent photoproduction of the J/ψ particle and for each event saved $|t|$ and ${}_{\mathrm{J}/\psi}p_t^2$. The ratio of these two quantities was calculated and stored.

3.3.4 Efficiency and purity procedure

Because we have only a few hundred events, we plan to extract the p_t^2 distribution using only a few p_t^2-ranges. It means that we have to sort our events into several bins. Because our distribution has exponential character, we expect a strong migration from the low p_t region to higher p_t regions. Therefore we used this procedure to choose the most appropriate binning to mitigate migrations.

What we want to study is by how much the transverse momentum squared of a generated particle (GP) and the corresponding reconstructed particle (RP) differ in one event. Therefore we prepared a sample, where we have the same number of RP and GP - on both were applied selection criteria for GP and RP. The next step is to put everything in a 2D histogram.

First we studied the efficiency. An example is shown in the upper plot of Fig. 3.7. In this figure both axes are divided according to the binning. The x-axis represents p_t^2 of the GP, while the y-axis stands for a combination of the GP and the RP. For example in box [2,1] is stored the fraction of events, where the GP p_t^2 was in the bin 2, but the RP p_t^2 was in bin 1. In other words we have a fraction of events, where p_t migrates from bin 2 to bin 1 during the reconstruction.

The estimation of the purity follows the same procedure, but on the x-axis we have p_t^2 of the RP instead. As the name of it suggests, these numbers show, how pure our reconstruction is. An instance is in the bottom plot of Fig. 3.7.

Ideally we would like to have the boxes in the diagonal showing 100% both in efficiency and in purity. The ideal case does not occurs in normal experiments, but for this measurement we could live with a number around 1-σ, this is in the range 60% to 70%. The numbers in Fig. 3.7 are far from it. This shows that the use of same-sized bins is not optimal. In Sec. 3.4 a scheme with bins of different sizes will be discussed.

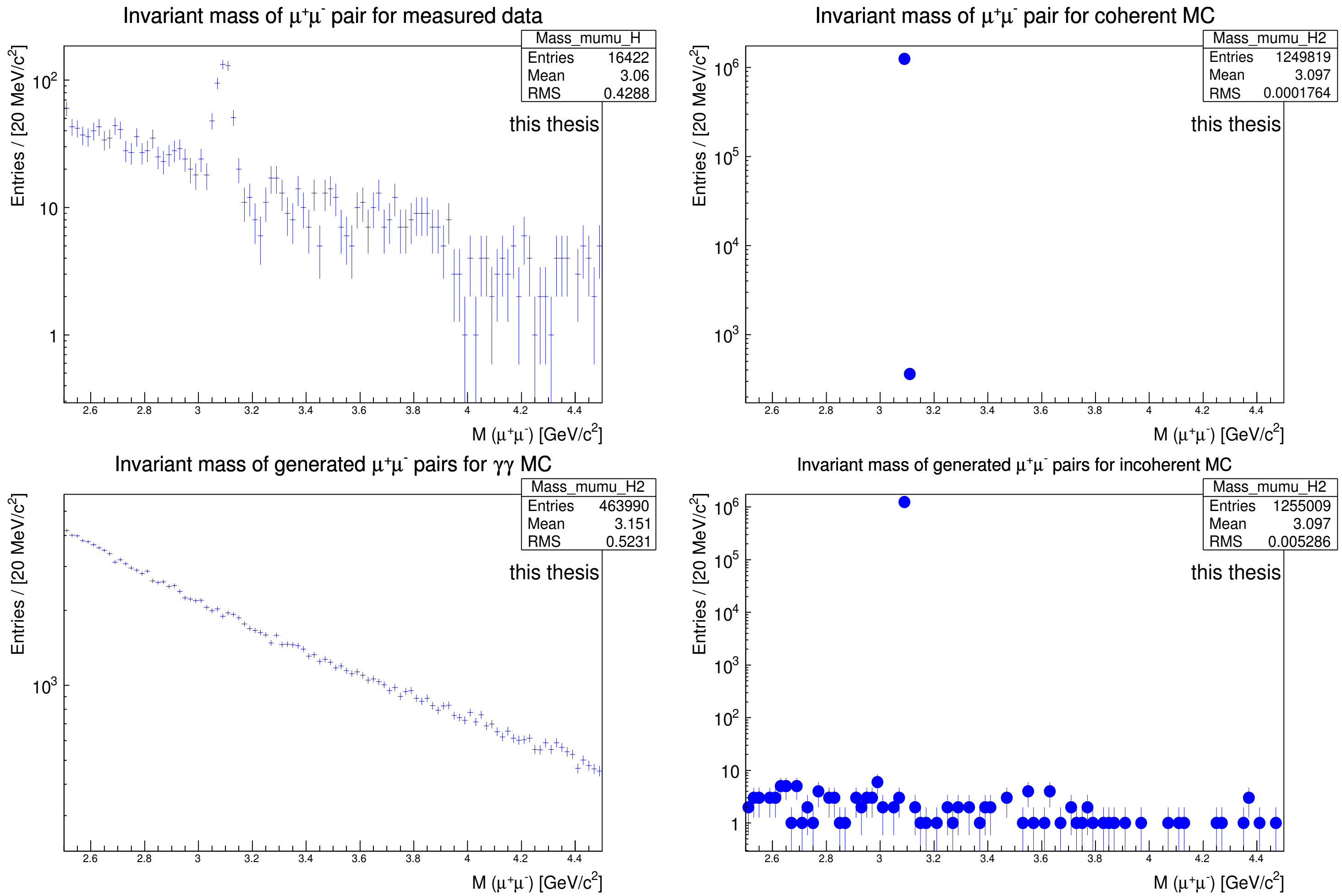

Figure 3.1: Plots of mass distributions for measured data, MC J/ψ coherent production, MC $\gamma\gamma$ production and MC J/ψ incoherent production. MC distributions show generated particles. A different marker was used for the right panels to improve the visibility.

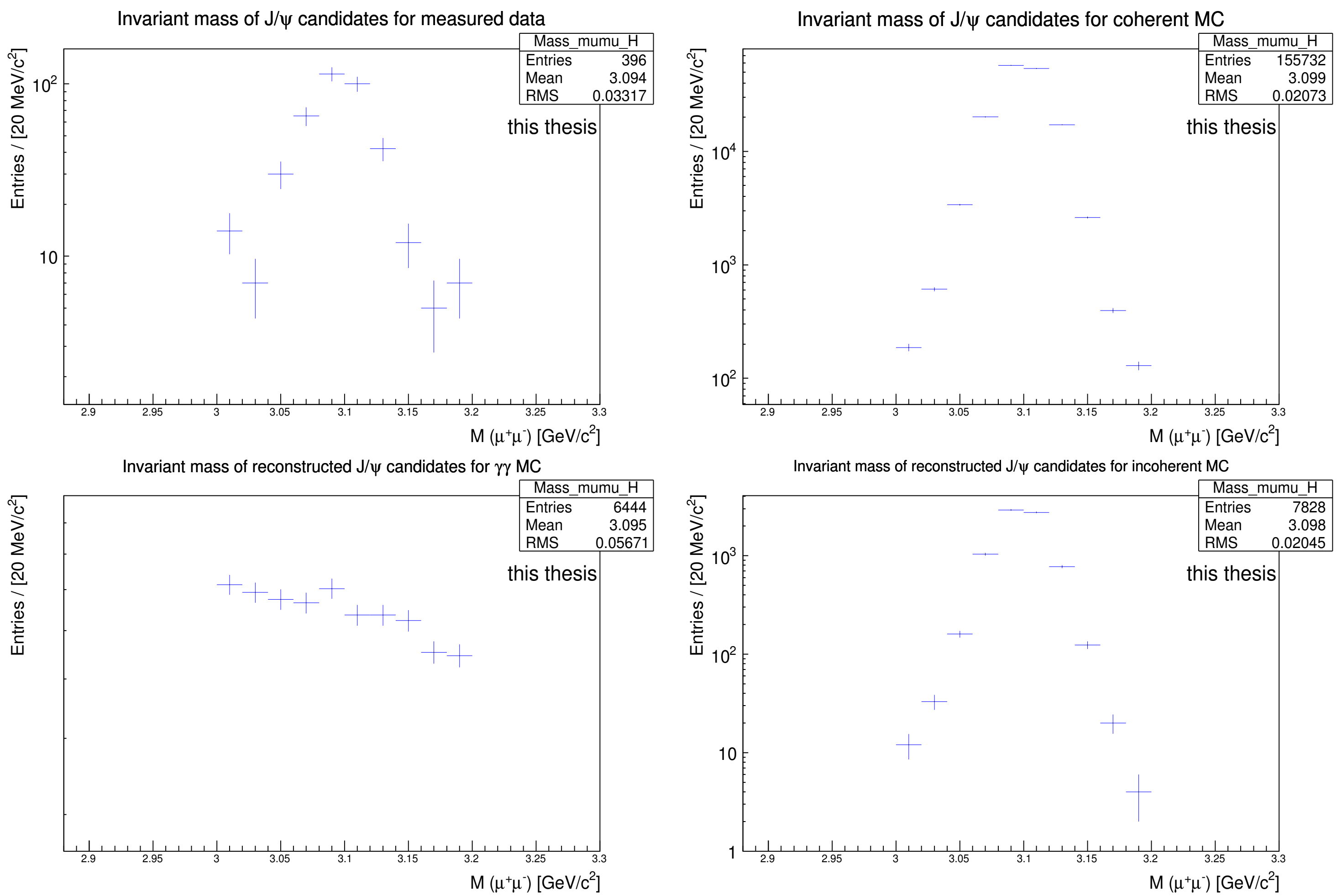

Figure 3.2: Plots of mass distributions for measured data, MC J/ψ coherent production, MC $\gamma\gamma$ production and MC J/ψ incoherent production. The mass and p_t selection criteria were used. MC distributions show reconstructed particles.

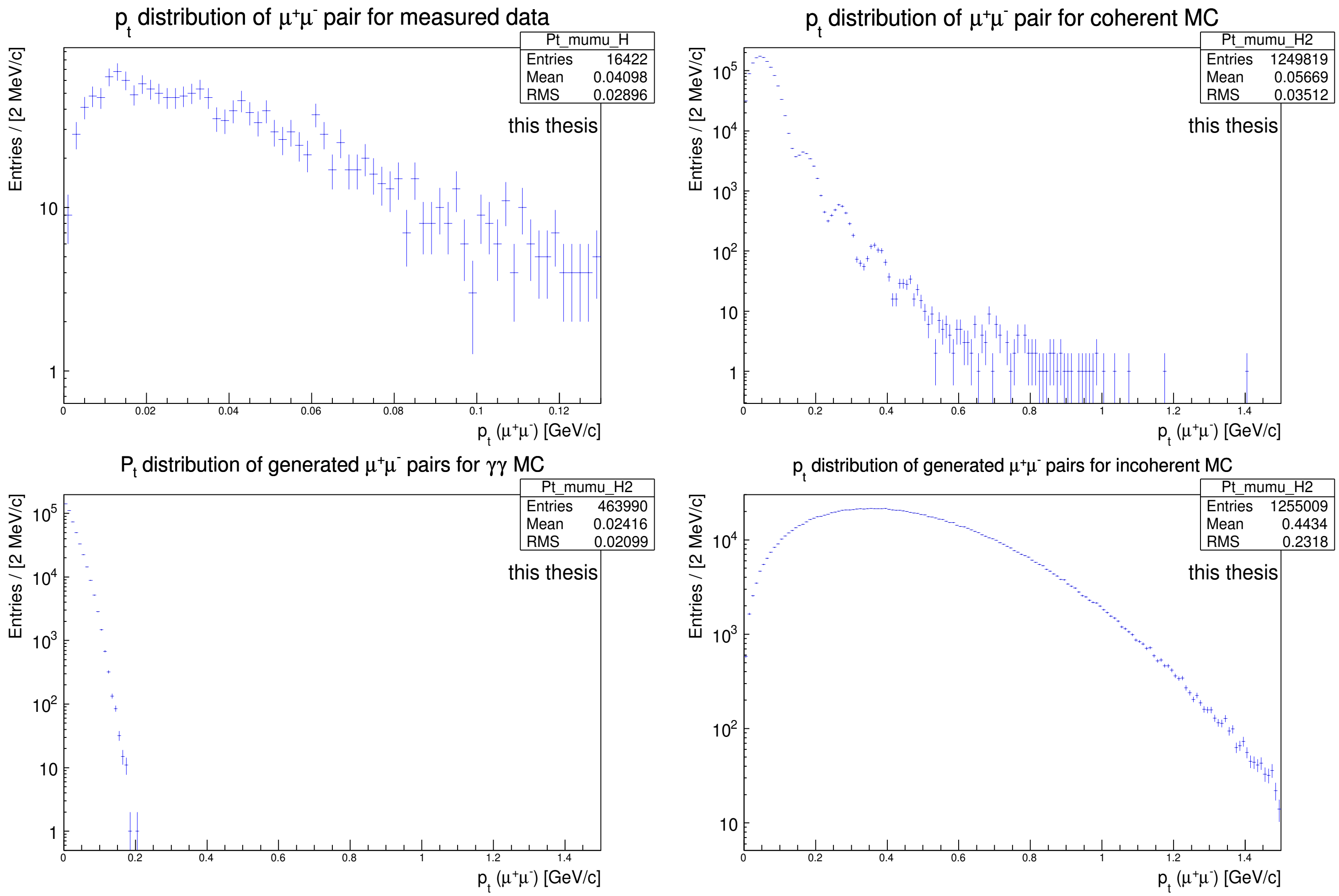

Figure 3.3: Plots of p_t distributions for measured data, MC J/ψ coherent production, MC $\gamma\gamma$ production and MC J/ψ incoherent production. MC distributions show generated particles. No p_t cut used.

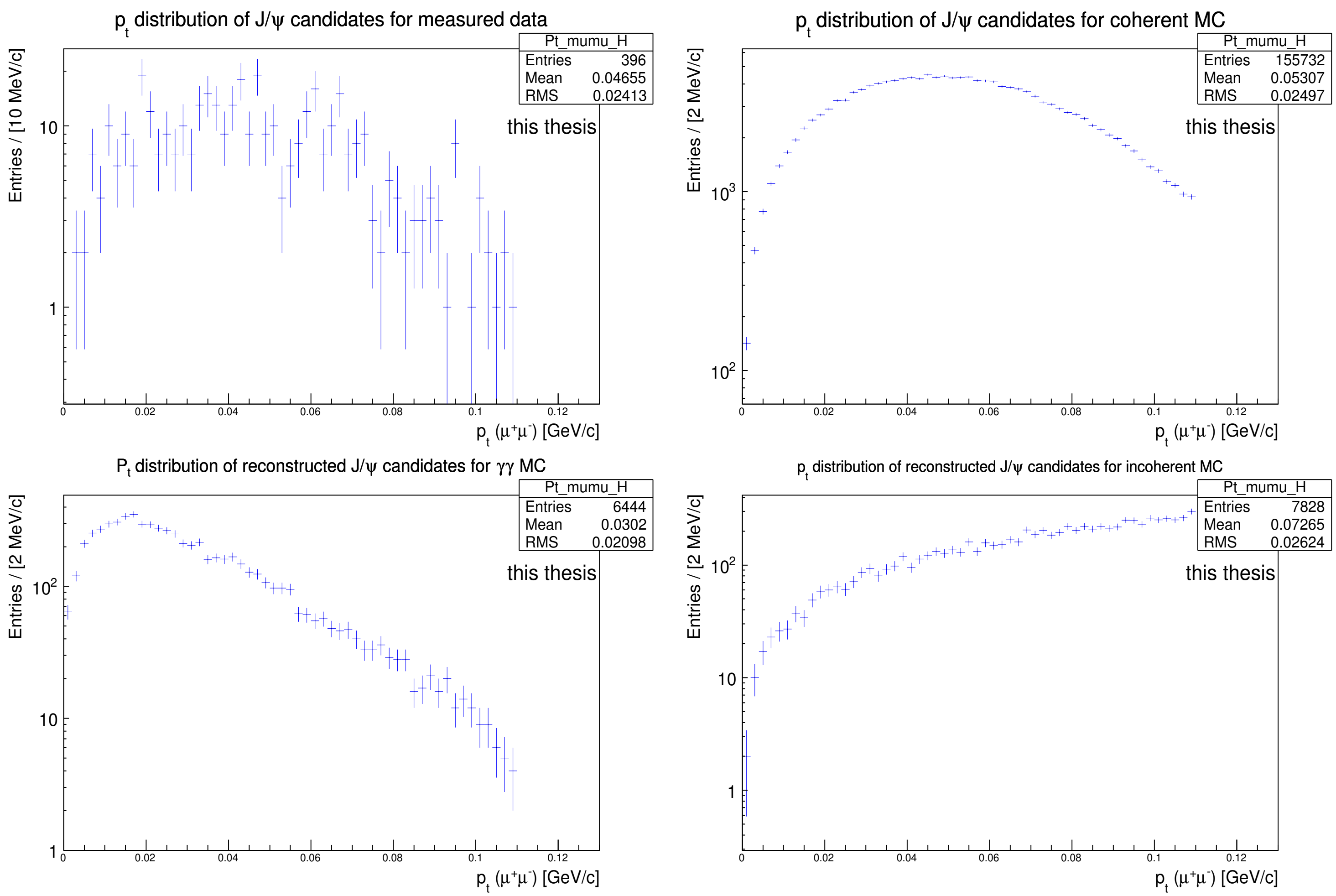

Figure 3.4: Plots of p_t distributions for measured data, MC J/ψ coherent production, MC $\gamma\gamma$ production and MC J/ψ incoherent production. The mass and p_t selection criteria were used. MC distributions show reconstructed particles.

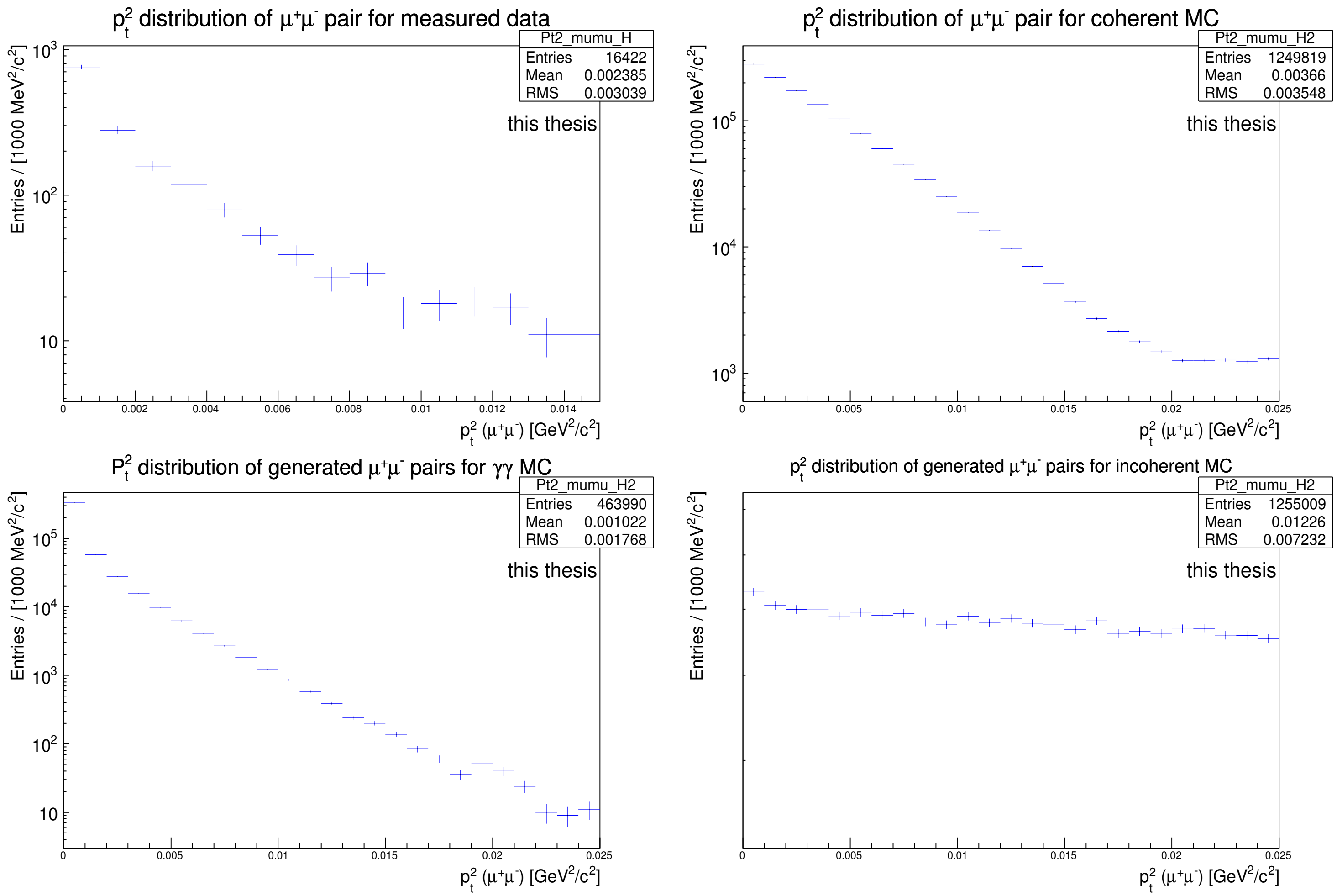

Figure 3.5: Plots of p_t^2 distributions for measured data, MC J/ψ coherent production, MC $\gamma\gamma$ production and MC J/ψ incoherent production. MC distributions show generated particles.

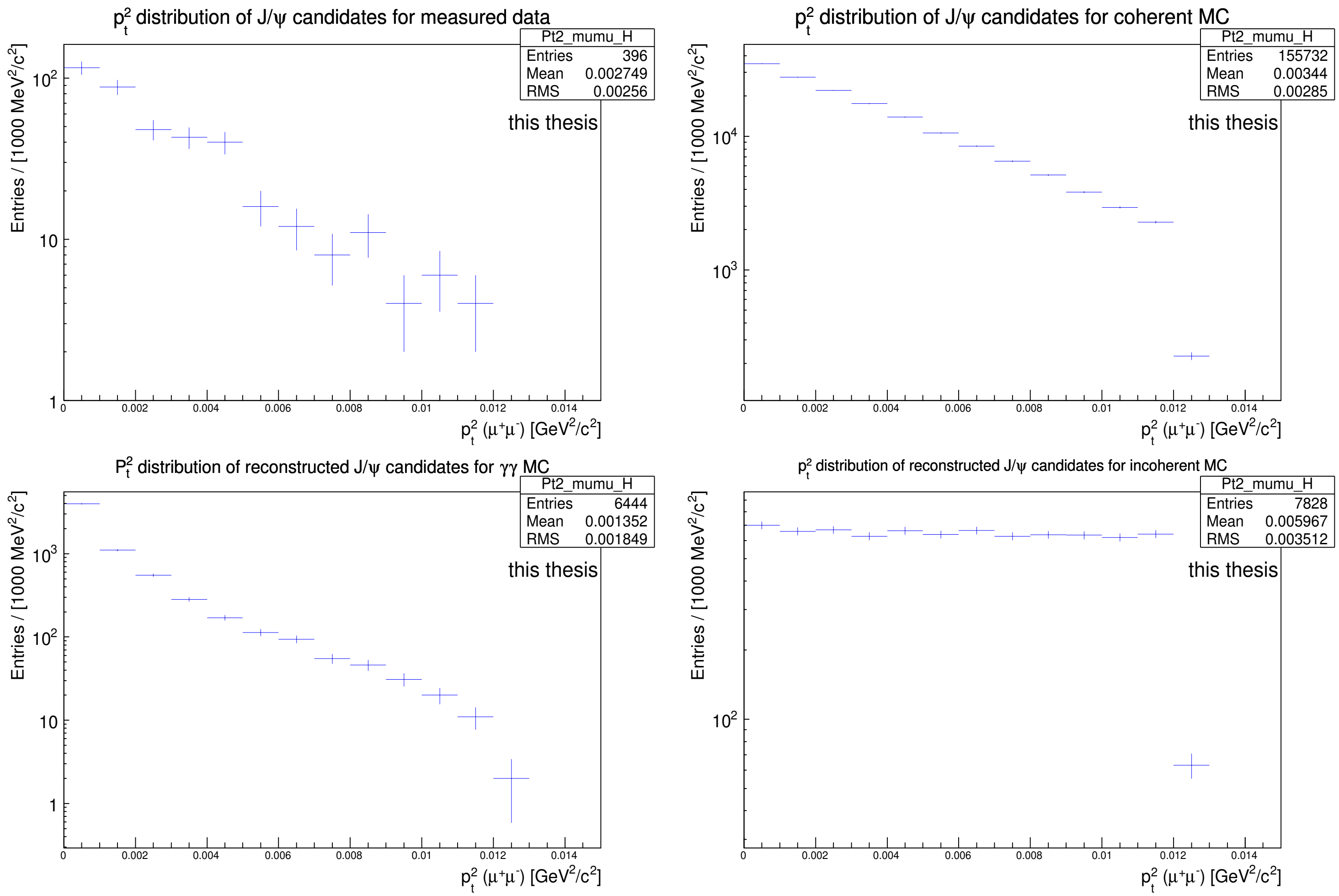

Figure 3.6: Plots of p_t^2 distributions for measured data, MC J/ψ coherent production, MC $\gamma\gamma$ production and MC J/ψ incoherent production. The mass and p_t selection criteria were used. MC distributions show reconstructed particles.

3.3.5 Fitting $|t|$-distribution with Monte Carlo procedure

The following study is performed using MC events from the coherent sample. The end goal of our measurement is to learn something about the transverse distribution of gluons in the lead nucleus. To do this, we have to fit the measured cross section as a function of $|t|$ to a model and obtain parameters which can be interpreted. We want to test this procedure using MC events, where we know the parameters used in the model and can thus check if the fitting procedure recovers them.

In principle, one should select candidates in a given bin, fit the mass distribution and subtract the contribution from background and finally apply the correction for detector effects (the acceptance $\times$ efficiency procedure) and the correction on the photon momentum. As we are using a MC without background it is easier to just count the number of events per bin and use this to fit the $|t|$ distribution.

The fit cannot be obtained directly from the histogram, because ROOT proceeds as follow: It takes the middle of the bin as a point for the fit and calculate horizontal errors as the width of the bin. This is not correct, because of the exponential behaviour of the expected fit. There is more events in the left half (lower p_t) of the bin than in the right one. Therefore we have to store all data using a TGraph function. This procedure slightly differs for generated particles and reconstructed particles.

The first part is the same for both. We applied appropriate selection criteria and classified the data according to their p_t^2 to several boxes. In each box we stored the number of events and the sum of all transferred momenta divided by the number of events. The first is for computation of the vertical error, the second serves as our fitting point.

To prepare a graph we sort the events in the p_t^2 boxes. Values in the bins have to be divided by their width to get the correct numbers. To corrected for the efficiency of the detector, we had to add the information we got from the acceptance $\times$ efficiency procedure. This is simple as it sounds. After the first step described in the previous paragraph we took the efficiency of the reconstruction for each bin and divided by it. At the end, we have to correct for the photon momentum, when we again divided each bin by the corresponding ratio.

Once these graphs are stored, we only have to fit them to get results. As a fit function we used 1.11 with a form factor 1.10. We had 3 free parameters - a, R_A and NORM - with options to fix R_A and/or a.

At the beginning we wanted to fit the coherent sample, divide it in several smaller samples and check, if we are able to get the correct values given by STARlight itself (written in Sec. 1.6.2). Once we succeed, we should have ready a solid tool for the analysis of the measured data.

3.3.6 Measurement procedure

The dependence of the cross section on transferred momentum p_t^2 from measured data can be obtained using Eq. 3.1. We want to fit this dependence, therefore we need to compute the cross section for several p_t^2 regions. The number and size of the regions is established from the efficiency and purity procedure mentioned in Sec. 3.3.4.

The number of coherently produced J/ψ mesons for each bin is a number calculated using Eq. 3.2. This number is corrected for the fraction of incoherent production and the feed down caused by ψ(2S). The yield of J/ψ candidates from the measured data is taken from the integral

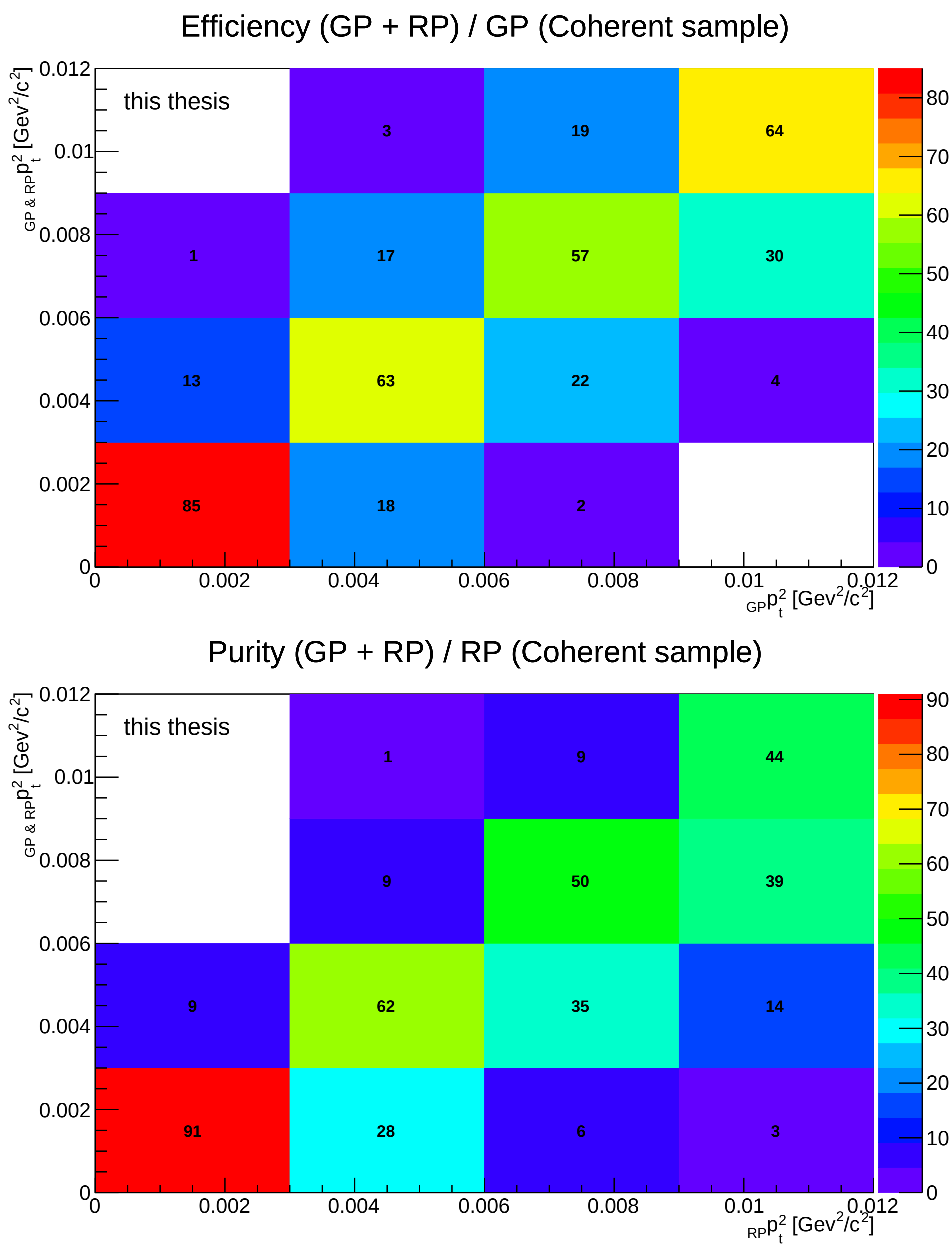

Figure 3.7: The efficiency and the purity with a fix-width binning for the coherent J/ψ sample. An example with 4 bins is shown. Numbers in the boxes are percent values.

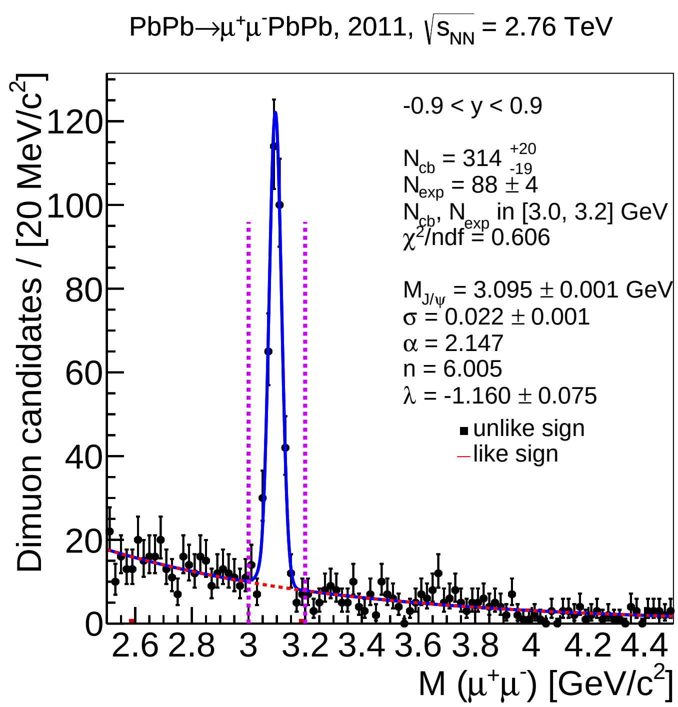

Figure 3.8: A fit of the invariant mass of measured data for $p_t^2 < 0.11$ GeV$^2/c^2$.

of a Crystal Ball function fitted to the mass distribution in the given p_t^2 bin. An example for the measured data for $p_t^2 < 0.11$ GeV$^2/c^2$ is in Fig. 3.8.

The acceptance × efficiency needed were gained using the acceptance × efficiency procedure discussed in Sec. 3.3.2 as well as the correction on the quasi-real photon (Sec. 3.3.3). Other numbers are constants taken from STARlight or PDG tables.

3.4 Selection of p_t^2 binning

Another feature we were interested in was the size of the bins we would use for the measurement. The efficiency and purity procedure was used for this.

In Fig. 3.9 we can see the result of this analysis with a variable-width binning consisting of 4 bins. As we can see for the efficiency, we have around 70% of particles on the diagonal. This is the best result we achieved after we tried many other configurations. Therefore we chose the binning to be: 1000 MeV$^2/c^2$, 3000 MeV$^2/c^2$, 4000 MeV$^2/c^2$, 8000 MeV$^2/c^2$. If we look at the purity, we have a strong migration of the particles, which were reconstructed in the last bin, to the third bin. This could be an issue given by the low statistics in the last bin and we should expect a large systematic error in the higher p_t^2 bin.

We have also studied the variable-width binning made of 5 bins. The best bin distribution can be seen in Fig. 3.10 and namely is: 600 MeV$^2/c^2$, 1800 MeV$^2/c^2$, 2800 MeV$^2/c^2$, 3600 MeV$^2/c^2$ and 3200 MeV$^2/c^2$. Again, for the efficiency we have roughly 64% on the diagonal, which corresponds approximately to a significance of 1 σ. Looking at the purity, we see, that we will have a problem in the last bin as was the case with 4 bins. In the following we will use 5 bins.

3.5 Correction for photon momentum

We mentioned before that we had to look at the momentum of the J/ψ particle from our process in comparison with the magnitude of $|t|$. We have generated 500 000 events and computed the ratio of the momenta shown in Fig. 3.11. Here we can see that for lower momenta the ratio is around 0.9. But with increasing momentum the ratio grows. To see what happened we have plotted the momentum distributions of the J/ψ and $|t|$. The results are in Fig. 3.12. We can easily see that the generated $\sqrt{|t|}$ hits the zero value in a range from 130 MeV to 140 MeV, but the computed p_t of the J/ψ has non-zero value in that range. This is caused by the generation of $|t|$, which is done by STARlight and it uses a form factor mentioned in Eq. 1.10, while the photon momentum is generated differently [44]. We use this ratio to correct the p_t^2 distributions to $|t|$ distributions before we fitted them.

3.6 Correction for acceptance × efficiency

As it was described above, we had to use our Monte Carlo data to correct measured data. Results can be found in Fig. 3.13. The efficiency of the detector varies around 12%. In the previous measurement mentioned in Sec. 1.7 the authors quoted a 4 times less efficient detector for both the coherent and incoherent samples. This difference could be caused by the missing trigger information in the reconstructed MC files, so we are not taking into account trigger efficiency

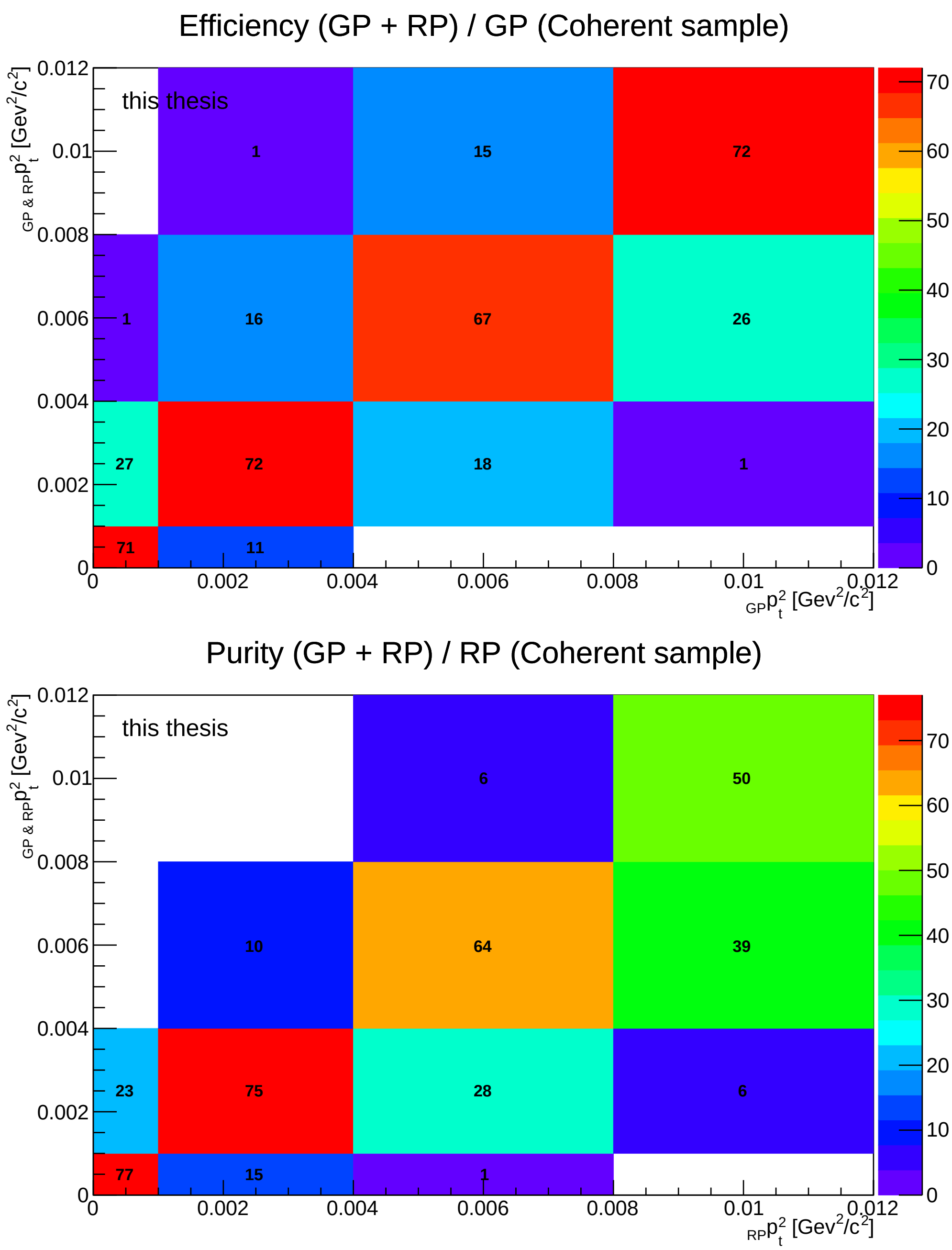

Figure 3.9: The efficiency and the purity with a variable-width binning for the coherent J/ψ sample. An example with 4 bins is shown. Numbers in the boxes are percent values.

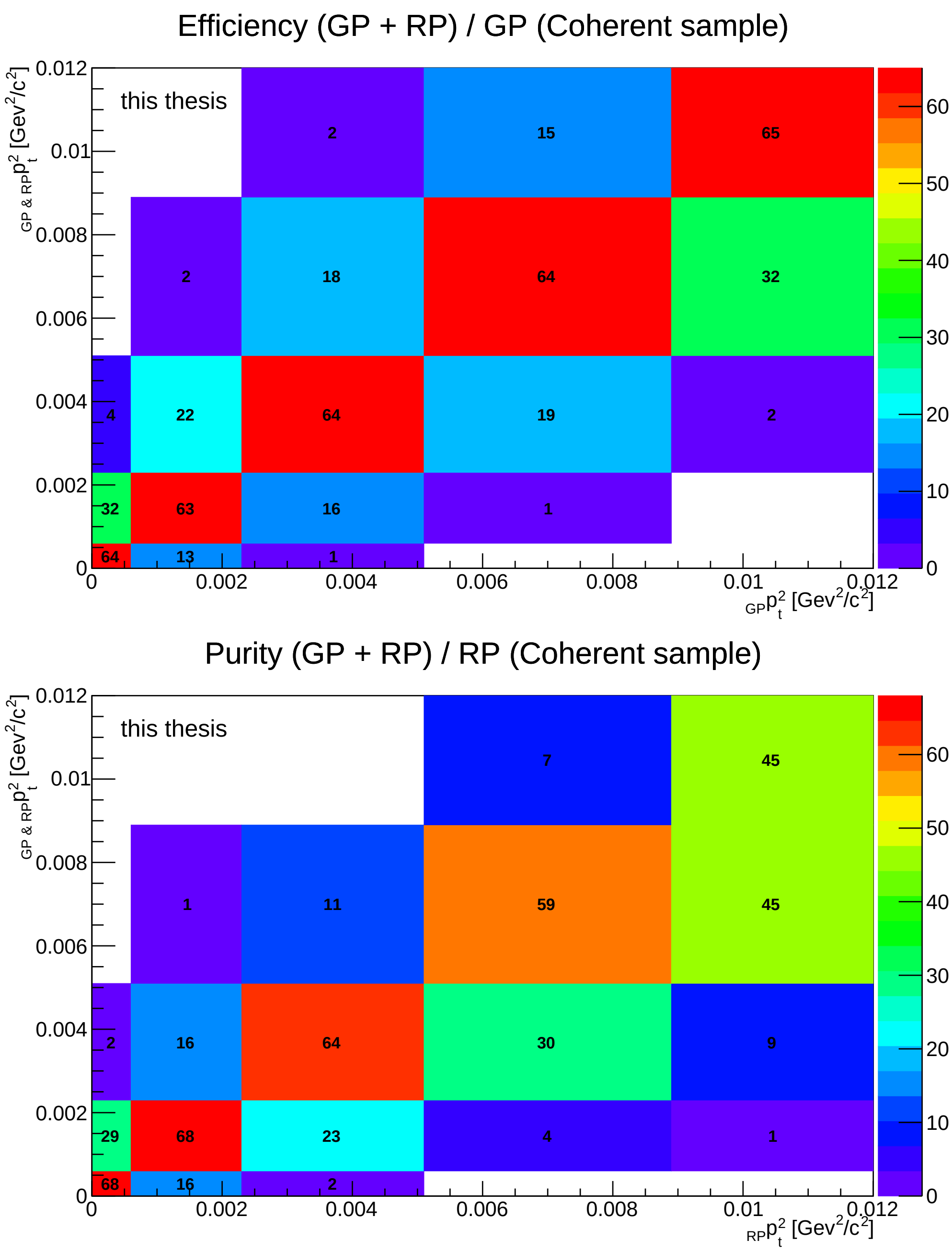

Figure 3.10: The efficiency and the purity with a variable-width binning for the coherent J/ψ sample. An example with 5 bins is shown. Numbers in the boxes are percent values.

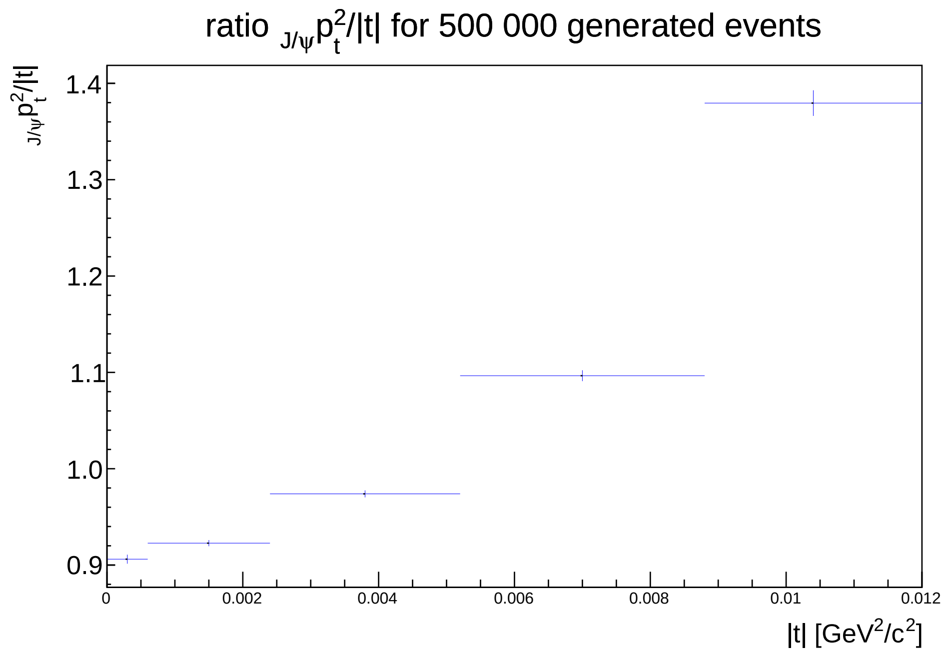

Figure 3.11: A plot of the ratio of the p_t^2 distribution of the J/ψ calculated by STARlight over the $|t|$ distribution generated by STARlight. We have generated 500 000 events.

(The authors do). The reason why the trigger is not correctly simulated and its effect on the correction for acceptance $\times$ efficiency is not fully understood and it is under investigation now.

The best shape of the ratio would be a flat distribution. If we take into account the errors, the ratio of incoherent samples fulfils this expectation. The other samples are a different story. As we can see, the detector is more efficient for higher p_t. For the coherent sample the explanation could be, that one of the muons from low-p_t J/ψ did not hit the detector, because these muons should be more back-to-back (their momenta should be more equal with opposite sign). But this is not a problem for our analysis. As we can see, we have more reconstructed particles in the high-p_t region than generated particles. The behaviour of the sample at large p_t is explained by the very few events generated there and migrations from lower p_t where there are many events, producing an efficiency larger than one, i.e. we are measuring events where no event was produced. As the p_t^2 distribution for incoherent events is flatter in this region, migration effects are less in this sample and the distribution is almost flat within errors. The proper estimation of the acceptance $\times$ efficiency correction taking into account migrations is work in progress.

3.7 Fit of Monte Carlo coherent J/ψ production

To compare several fits we have decided to split this sample into several smaller ones. Because we want to also examine the possibility of fitting our measured data, we prepared MC samples with a similar number of entries as found in data. Figure 3.8 tells us to fit samples with 314 entries which bring us to the final number of 534 (100) samples of generated particles (reconstructed

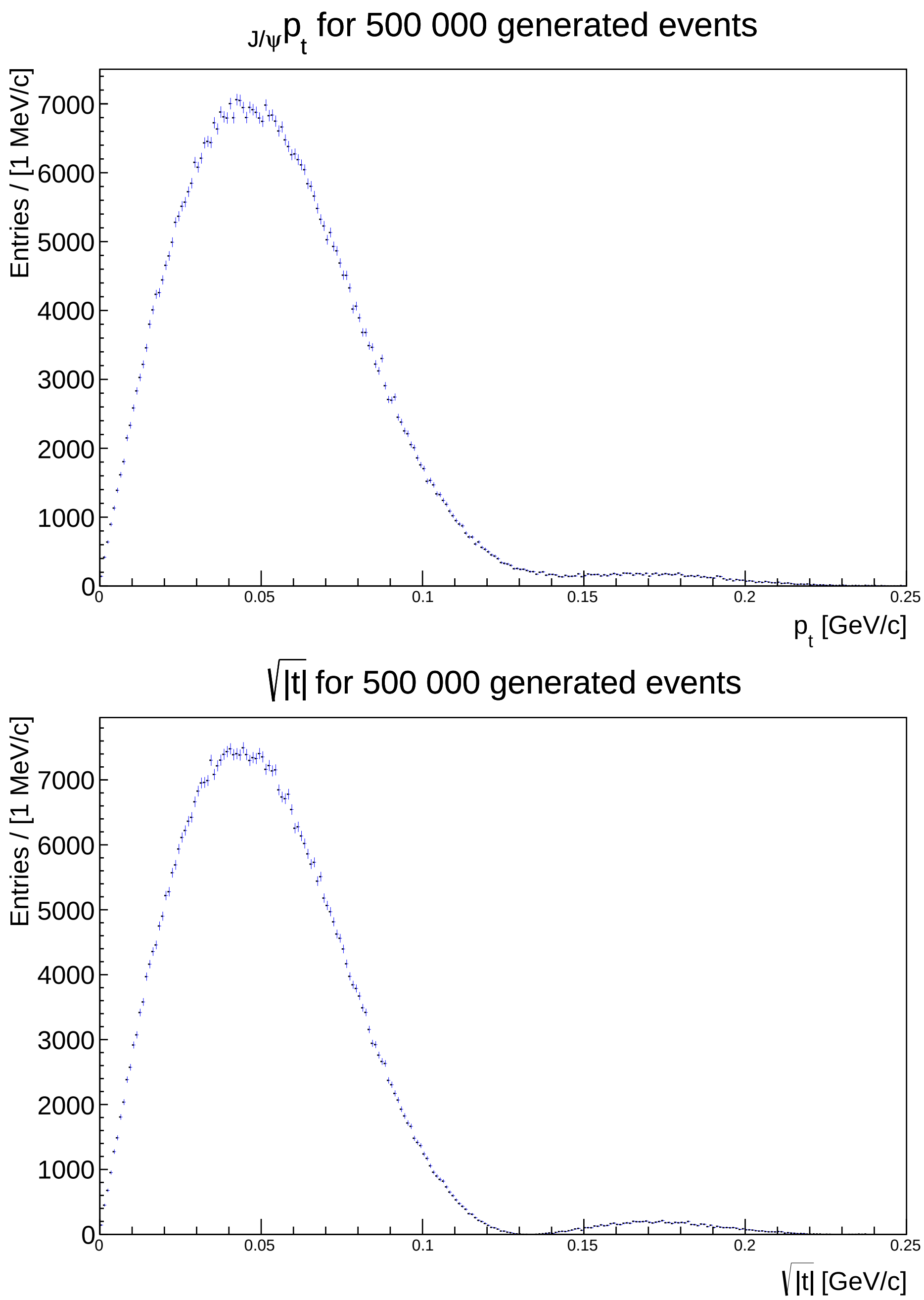

Figure 3.12: Plots of the p_t distributions for the J/ψ calculated by STARlight and of the $\sqrt{|t|}$ distribution generated by STARlight. We have generated 500 000 events.

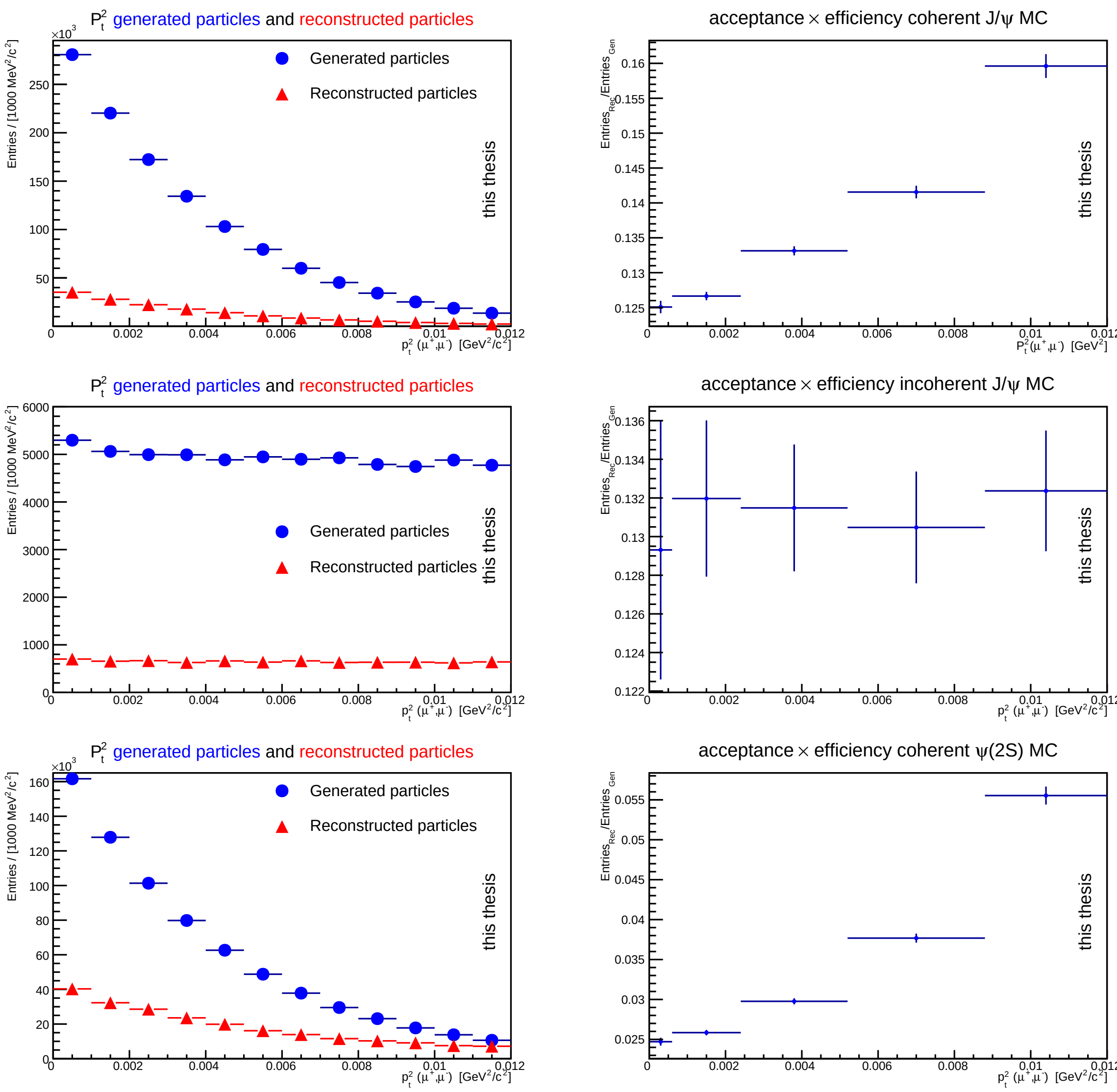

Figure 3.13: Plots of the p_t^2 distributions for generated particles and reconstructed particles (left panels) and their ratios (right panels) for (from top to bottom) coherent J/ψ, incoherent J/ψ and coherent ψ(2S) samples. On the left panels the ψ(2S) distribution for reconstructed particles is scaled up by a factor of 10.

particles). The number of entries in each bin is increased due to the application of the correction for the detector effect (acceptance $\times$ efficiency procedure) and the correction for the photon momentum. Examples of these fits are shown in Figs. 3.14, 3.15 and 3.16. To satisfy the used model (Eqs. 1.10 and 1.11) we wanted to achieve the values $a = 0.7$ fm and $R_A = 6.62$ fm. We should also state that all used fits converged.

In the top plot of Fig. 3.14 we show a fit of the sample of generated particles from the Monte Carlo coherent sample as a representative example. We fitted the sample with fixed a and R_A and we see, that the fit is with a good agreement with data points. In the bottom part we plot R_A results of the fits with only fixed a for all samples. The mean value is (6.67 ± 0.12) fm. This value is comparable with the correct value within the error. Also if we look to the plot, the green line, which represents the expected value of 6.62 fm, actually describes the data well. From this we conclude, that our corrections are good enough to get back the values, which were generated by STARlight for the case of fixed a.

The next step is to fit the samples with reconstructed particles. We applied all our corrections. Examples of fits with all parameters free for cases with 4 bins and 5 bins can be found in Fig. 3.15. From this we have learnt that we can fit the data, but with large errors. For the parameter a the relative error goes over 50%. We have decided to fix this value on 0.7 fm to give more stability to the fit. In Fig. 3.16 one can see instances of such fits. In general, we could get the R_A with a relative error around 5%.

As it was done for the generated particles, we fit the fitted values of R_A for the cases with 4 bins and 5 bins. These results are in the Fig. 3.17. If we choose to fit samples with 4 bins, we get $R_A = (6.72 \pm 0.26)$ fm and if we choose 5 bins, the resulting number is $R_A = (6.70 \pm 0.26)$ fm. The errors are obtained from the fit. Because the errors of both cases are comparable and we want to reach the STARlight value 6.62 fm, we have decided to work with the data distributed in 5 bins.

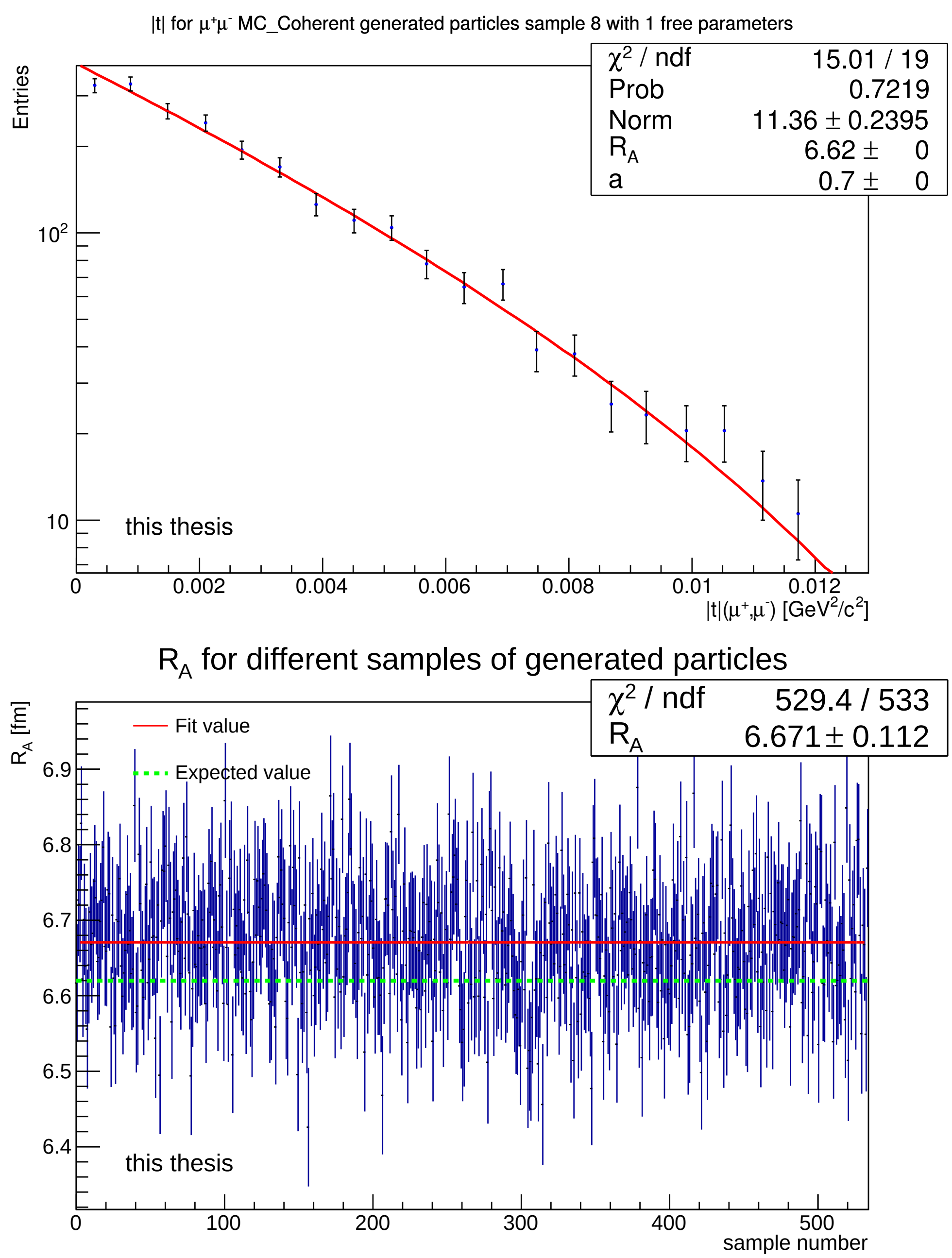

Figure 3.14: (top) A fit of the $|t|$ distribution of the coherent J/ψ sample for generated particles using Eq. 1.11 with fixed parameters a and R_A. (bottom) A fit of the average of the R_A parameter over all samples of generated particles. In the bottom case the fits had fixed only the a parameter.

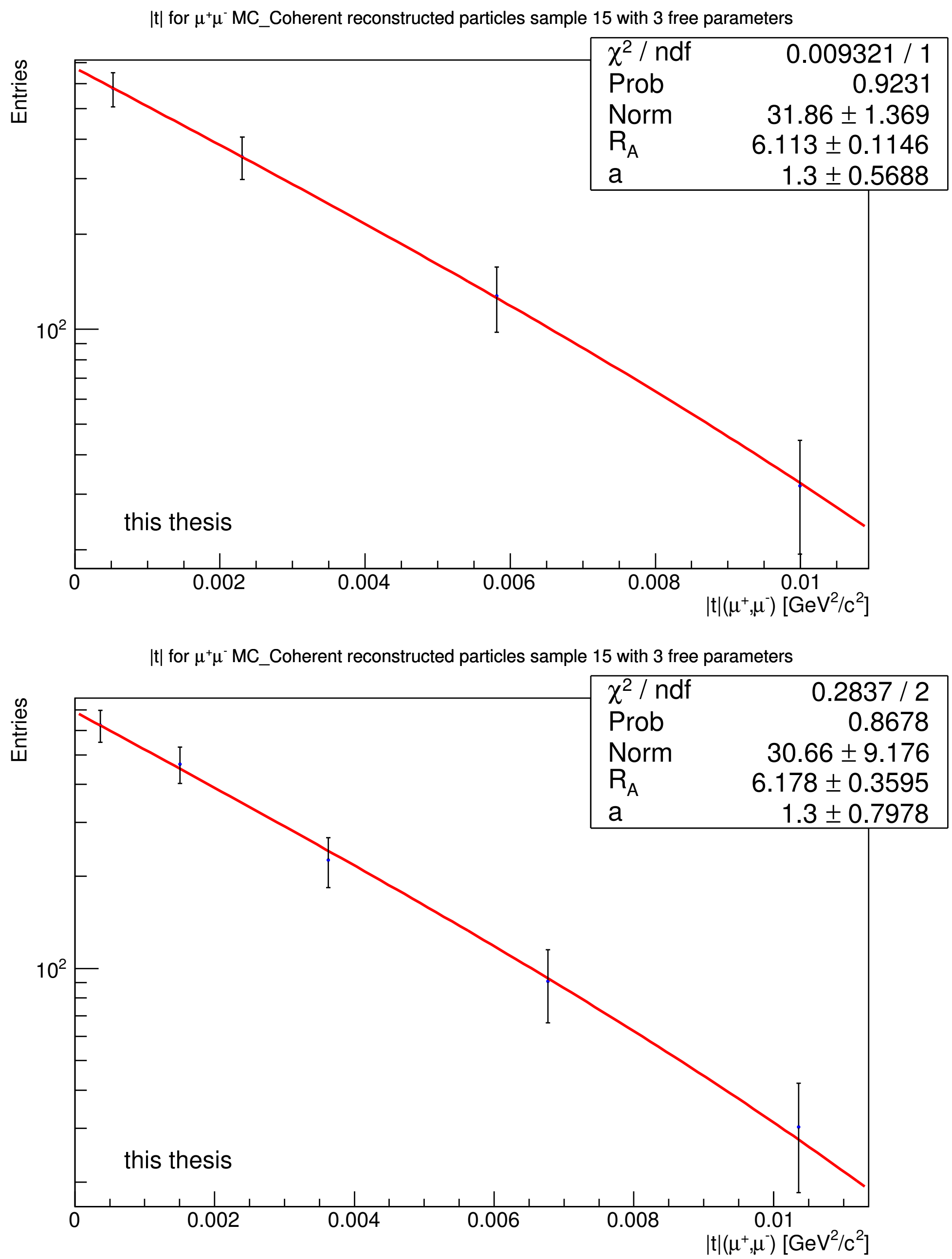

Figure 3.15: A fit of the $|t|$ distribution of the coherent J/ψ sample for reconstructed particles using Eq. 1.11 with all parameters free with 4 bins (top) and 5 bins (bottom).

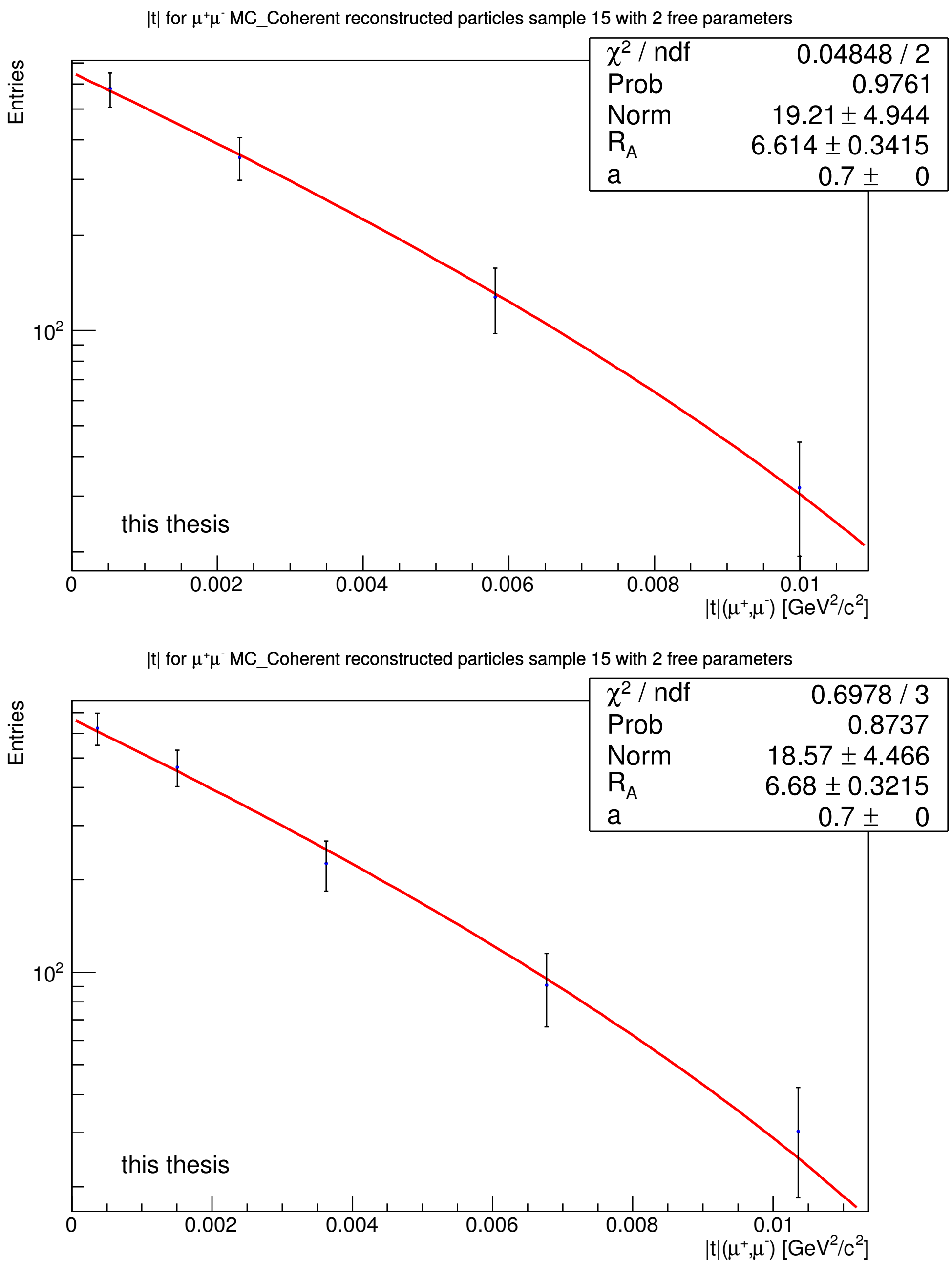

Figure 3.16: A fit of the $|t|$ distribution of the coherent J/ψ sample for reconstructed particles using Eq. 1.11 with fixed parameter a with 4 bins (top) and 5 bins (bottom).

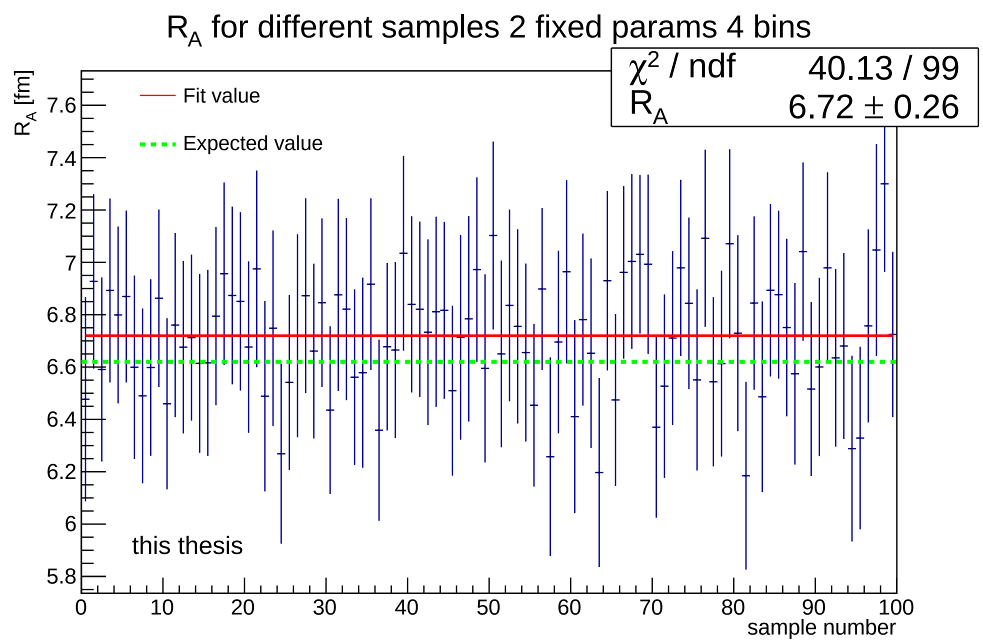

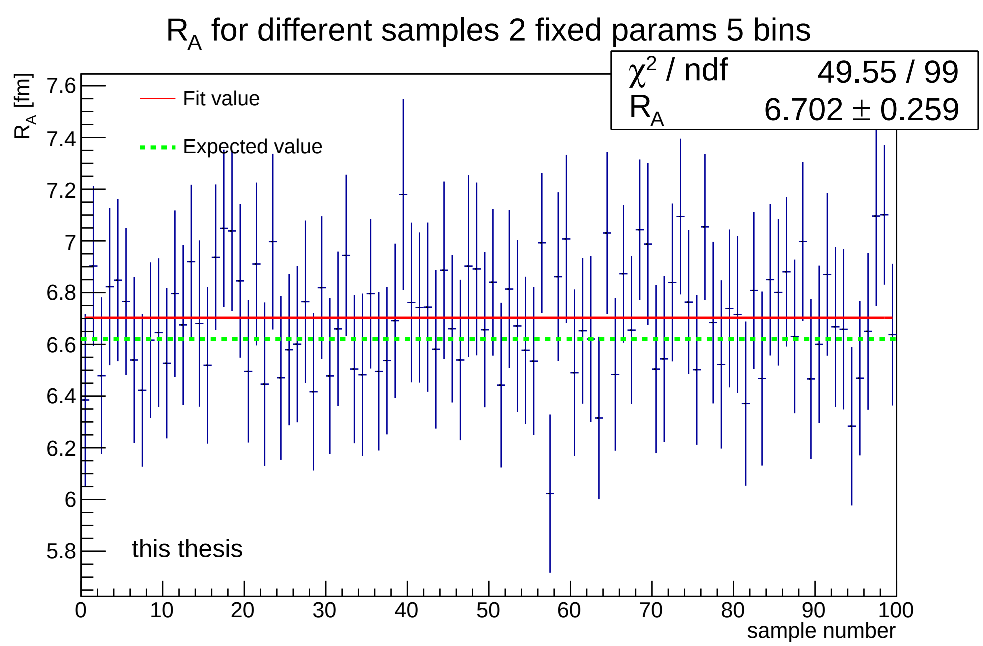

Figure 3.17: A fit of the average of the R_A parameter over all samples of reconstructed particles with 4 bins (top) and 5 bins (bottom). All fits had fixed only the a parameter.

Chapter 4

Measurement with Run 1 data

In this chapter we will present and discuss the main result of this thesis.

4.1 Yield of J/ψ candidates

The first important task of the measurement itself is to obtain the yield of J/ψ candidates. As we described in Sec. 3.3.6, we used Crystal Ball and exponential functions to fit the invariant mass distribution. The Crystal Ball parametrization has four parameters. Two of them, so called n and α parameters are very sensitive to fluctuations and to background, so they cannot be determined correctly from data alone when the number of available events is small. Because of this, we fit pure MC samples and used the fitted values to fix these parameters when fitting data. Since the pre-selected data are a mixture of coherent and incoherent production, we looked at the fits of both samples, as it is shown in the top plots of Fig. 4.1. The difference between parameters is not large and because the coherent production dominates over the incoherent one in the p_t region of our interest, we used the coherent MC production to fix these two parameters.

The yield retrieved from the first bin can be found in the bottom plots of Fig. 4.1. The resulting number is $N^{\rm Yield}_{\rm bin1} = (48\ ^{+9}_{-8})$ candidates. Next two bins are in Fig. 4.2 and the yields are $N^{\rm Yield}_{\rm bin2} = (118\ ^{+12}_{-11})$ and $N^{\rm Yield}_{\rm bin3} = (99\ ^{+11}_{-10})$ candidates. The last two bins are shown in Fig. 4.3 and we have $N^{\rm Yield}_{\rm bin4} = (34 \pm 6)$ and $N^{\rm Yield}_{\rm bin5} = (16\ ^{+5}_{-4})$ candidates from them. The fit to the full p_t^2 range is shown in Fig. 3.8 and the corresponding yield is $314\ ^{+20}_{-19}$, which is a comparable number to the number mentioned in Sec. 1.7.3.

These numbers served as an input to the numerator of Eq. 3.2.

4.2 Correction for incoherent production

As mentioned above, we need to correct our yield for the incoherent production of J/ψ mesons. How to compute this number is derived in Eqs. 3.3 and 3.4. Some input values are in Tab. 4.1, which should be complemented with the value of the total cross section of coherent (incoherent) production $\sigma^{\rm coh}_{{\rm J}/\psi} = 26.1$ mb ($\sigma^{\rm inc}_{{\rm J}/\psi} = 12.4$ mb) taken from STARlight.

Calculated fractions of incoherent J/ψ (in Tab. 4.1) are ranging from 8.4‰ to 11.1% for different bins. The fractions are increasing with higher p_t^2, which is the expected behaviour, if we compare with Fig. 3.4, where we have plotted the p_t distributions of both samples.

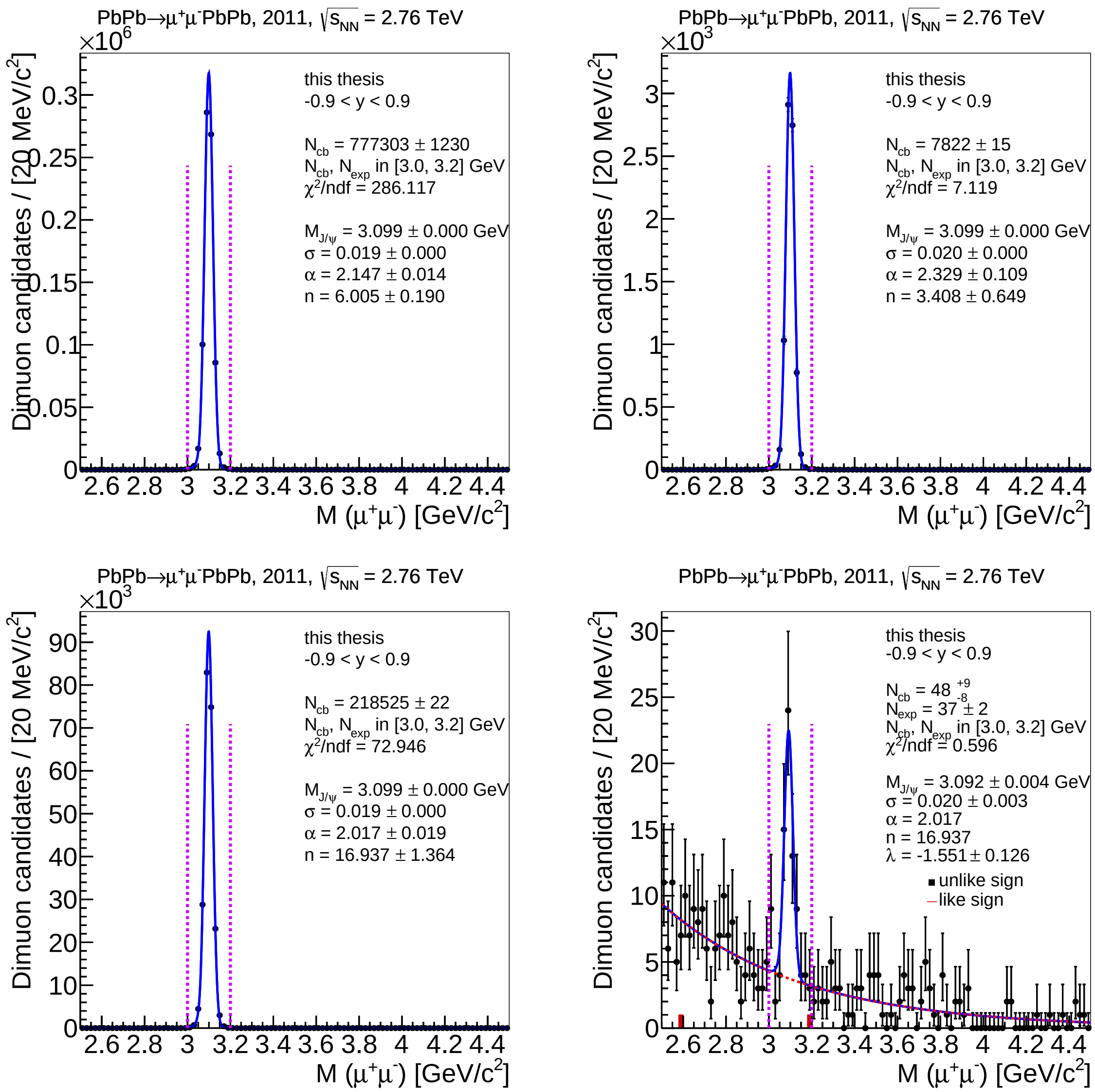

Figure 4.1: (top) Fits of the mass distribution of coherent (left) and incoherent (right) MC in $p_t^2 \in [0; 12000]\ \frac{\mathrm{MeV}^2}{\mathrm{c}^2}$; (bottom) fits of the mass distribution of coherent MC (left) and coherent J/ψ candidates (right) in $p_t^2 \in [0; 600]\ \frac{\mathrm{MeV}^2}{\mathrm{c}^2}$.

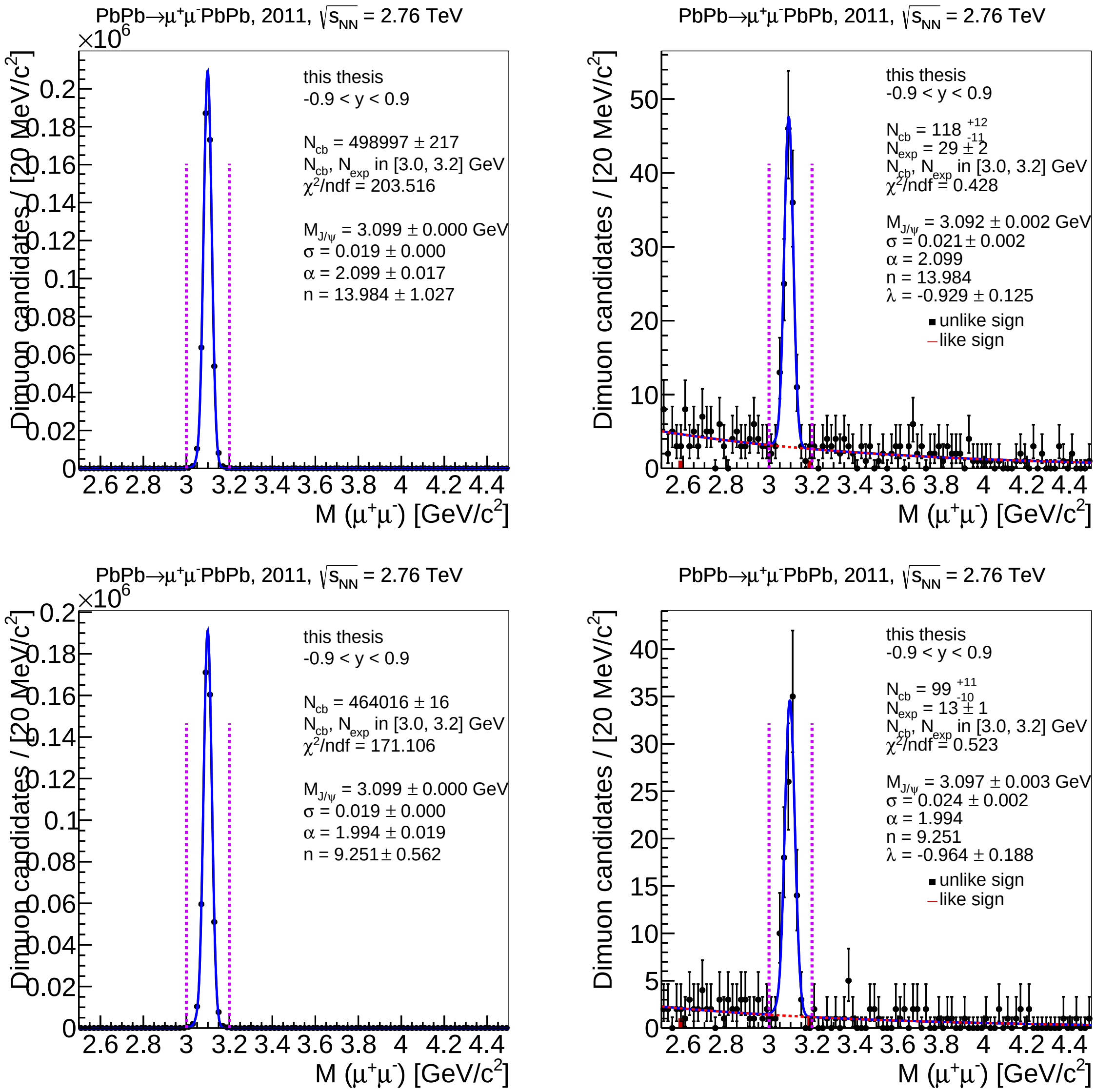

Figure 4.2: Fits of the mass distributions of coherent MC (left) and coherent J/ψ candidates (right) in $p_t^2 \in [600; 2400]\ \frac{\mathrm{MeV}^2}{\mathrm{c}^2}$ (top) and $p_t^2 \in [2400; 5200]\ \frac{\mathrm{MeV}^2}{\mathrm{c}^2}$ (bottom).

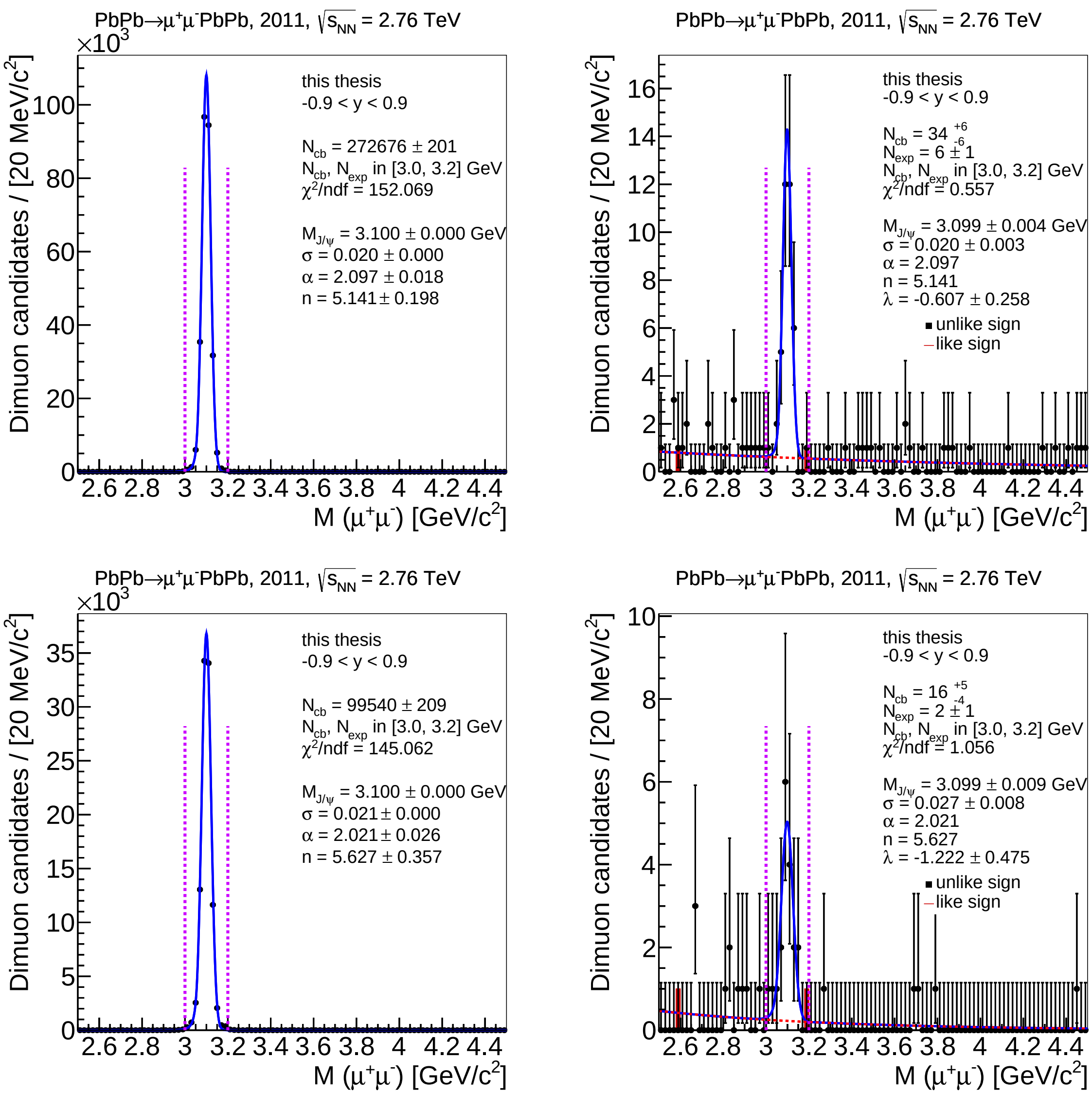

Figure 4.3: Fits of the mass distributions of coherent MC (left) and coherent J/ψ candidates (right) in $p_t^2 \in [5200; 8800]\ \frac{\mathrm{MeV}^2}{\mathrm{c}^2}$ (top) and $p_t^2 \in [8800; 12000]\ \frac{\mathrm{MeV}^2}{\mathrm{c}^2}$ (bottom).

Our percentage of incoherent events is 2-3 times larger than measured by [1] and stated in Sec. 1.7. This difference could be caused by the absence of the trigger information in the MC, which produces a difference in the computed acceptance $\times$ efficiency.

4.3 Correction for feed-down

The last correction needed for our measurement is the correction for the feed-down, which can be calculated from Eq. 3.7. Input numbers for different bins are in Tab. 4.2. The branching ratio was already mentioned in Sec. 3.1 and the total cross section of the process used by STARlight is $\sigma^{\mathrm{tot}}_{\psi(2\mathrm{S})} = 1.6$ mb.

The size of the feed-down varies from 1.20 to 2.35 ‰. These contributions are quite small in comparison with the results from [1] which are around 10%. In our analysis we use a MC simulation of a specific $\psi(2\mathrm{S})$ decay to J/ψ and $\pi^+\pi^-$. This decay accounts only for about half of the of decays through J/ψ. The main reason why we used this MC is the unavailability of simulations of other decays. So we can correct only for a part of the feed-down. Furthermore the influence of the missing trigger efficiency in the MC simulations in the value of f_D is unknown.

We computed the cross section dependence on p_t^2 for three different feed-down factors - $f_D =$ 10%, factors from Tab. 4.2 and $f_D = 0$. We found that all three results are compatible within statistical errors. Therefore we will repeat this process, when proper MC simulations will be available, but for our calculations we used our results.

4.4 Cross section p_t^2-dependence

To get the p_t^2-dependence of the coherent cross section, we make use of Eq. 3.1. Numerators for each bin are calculated from the values mentioned in the previous subsections and Eq. 3.2. The Acc$\times\epsilon$ are taken from the acceptance $\times$ efficiency procedure (Sec. 3.3.2) applied on incoherent MC production, which we trust more than the case of coherent MC production. The branching ratio is $(5.961 \pm 0.033)\%$ according to [19], the total integrated luminosity $\mathscr{L}_{int}$ was $22.4^{+0.9}_{-1.2}$ $\mu\mathrm{b}^{-1}$ [43] and the used binning is in Sec. 3.4.

If we put all these results together, we can build a plot of the cross section dependence on p_t^2, which is in Fig. 4.4. The measurements are also reported in Tab. 4.3. We see that the cross section drops with increasing p_t^2. This is the expected behaviour. The errors of the first and the last bins are relatively large, because in these bins we have fewer events. The error of the first bin could be reduced by enlarging the interval of the first bin, which would affect other bins. A more precise measurement of the last bin needs larger statistics which would be available in the data taken in Run 2.

Integrating the measurements shown in Fig. 4.4 over their p_t^2 range, we can compute the cross section dependence on rapidity y. Our calculations gives $\mathrm{d}\sigma^{\mathrm{coh}}_{\mathrm{J}/\psi}/\mathrm{d}y = 0.98^{+0.07}_{-0.06}(\mathrm{sta})$ mb. We can compare this result with the number originally reported in [1] and written in Sec. 1.7. Our number is smaller by 1.40 mb. The reason for the difference is not known (although we suspect an influence from the missing trigger information in the MC simulations) and currently is under investigation.

4.5 Cross section $|t|$-dependence and fit

Using the correction for the photon momentum η_{SL} according to Eq. 3.8, we can obtain $|t|$-dependence of the coherent cross section. The η_{SL} are taken from a private STARlight generated sample. The resulting factors are shown in Fig. 3.11 and Fig. 3.12. The results are in Tab. 4.3.

In addition, we tried to fit our measurement with two models - the general exponential model defined by Eq. 1.12 and the model used by STARlight and mentioned in Eq. 1.11. First, we needed to use a correction according to Eq. 3.8. The first fit is in Fig. 4.5 and as a result we have $\lambda = 349 \pm 24$, which would correspond to a nuclear radius of (5.2 ± 0.2) fm. The second model is fitted in Fig. 4.6 and the transversal nuclear radius goes from (7.13 ± 0.23) fm to (7.23 ± 0.10) fm when the parameter corresponding to the range of the Yukawa potential was fixed to $a = 0.7$ fm or not. These fits are just a first attempts to see, if we can make the fits. We are not going to extract any conclusion about the models based on these fits at this moment. In the future, the goal of this measurement is to compare results of Run 1 and Run 2 and see if the parameters change when Bjorken x is changed, which is one of the signatures of saturation effects.

p_t^2 $\left[\frac{\mathrm{MeV}^2}{\mathrm{c}^2}\right]$	$N^{\mathrm{inc}}_{\mathrm{J}/\psi}$	$(\mathrm{AxE})^{\mathrm{inc}}_{\mathrm{bin}}$	$N^{\mathrm{coh}}_{\mathrm{J}/\psi}$	$(\mathrm{AxE})^{\mathrm{coh}}_{\mathrm{bin}}$	f_I [‰]
$[0; 600]$	418 ± 21	0.129 ± 0.007	21 852 ± 148	0.1237 ± 0.0009	8.4 ± 0.6
$[600; 2400]$	1 205 ± 35	0.132 ± 0.004	49 895 ± 224	0.1252 ± 0.0006	10.5 ± 0.5
$[2400; 5200]$	1 811 ± 43	0.131 ± 0.003	46 398 ± 216	0.1316 ± 0.0007	17.9 ± 0.6
$[5200; 8800]$	2 297 ± 48	0.130 ± 0.003	27 262 ± 166	0.1398 ± 0.0009	41 ± 2
$[8800; 12000]$	2 026 ± 46	0.132 ± 0.003	9 945 ± 100	0.158 ± 0.002	111 ± 4

Table 4.1: Input numbers and results of Eq. 3.3. $N^{\mathrm{inc}}_{\mathrm{J}/\psi}$ is the number of reconstructed particles from incoherent MC in a bin, $(\mathrm{AxE})^{\mathrm{inc}}_{\mathrm{bin}}$ is the correction on detector effects from incoherent MC in a bin, $N^{\mathrm{coh}}_{\mathrm{J}/\psi}$ is the number of reconstructed particles from coherent MC in a bin, $(\mathrm{AxE})^{\mathrm{coh}}_{\mathrm{bin}}$ is the correction on detector effects from coherent MC in a bin and f_I is the calculated correction on incoherent production in a bin. All errors are statistical.

p_t^2 $\left[\frac{\mathrm{MeV}^2}{\mathrm{c}^2}\right]$	$N^{\mathrm{coh}}_{\psi(2\mathrm{S})}$	$(\mathrm{AxE})^{\mathrm{coh}}_{\psi(2\mathrm{S})}$	$N^{\mathrm{coh}}_{\mathrm{J}/\psi}$	f_D [‰]
$[0; 600]$	89 443 ± 300	0.0233 ± 0.0005	176 733 ± 421	1.199 ± 0.003
$[600; 2400]$	204 984 ± 453	0.0241 ± 0.0004	398 553 ± 632	1.246 ± 0.003
$[2400; 5200]$	187 472 ± 433	0.0273 ± 0.0004	352 981 ± 595	1.387 ± 0.003
$[5200; 8800]$	110 145 ± 332	0.0333 ± 0.0005	195 482 ± 443	1.691 ± 0.004
$[8800; 12000]$	41 116 ± 203	0.0453 ± 0.002	63 382 ± 252	2.345 ± 0.007

Table 4.2: Input numbers and results of Eq. 3.7. $N^{\mathrm{coh}}_{\psi(2\mathrm{S})}$ is the number of generated particles from coherent $\psi(2\mathrm{S})$ MC in a bin, $(\mathrm{AxE})^{\mathrm{coh}}_{\psi(2\mathrm{S})}$ is the correction on detector effects from coherent $\psi(2\mathrm{S})$ MC in a bin, $N^{\mathrm{coh}}_{\mathrm{J}/\psi}$ is the number of generated particles from coherent J/ψ MC in a bin and f_D is the calculated correction on feed-down in a bin. All errors are statistical.

p_t^2 $\left[\frac{\mathrm{MeV}^2}{\mathrm{c}^2}\right]$	[0;600]	[600;2400]	[2400;5200]	[5200;8800]	[8800;12000]
$\frac{\mathrm{d}\sigma}{\mathrm{d}p_t^2}$ $\left[\frac{\mathrm{mb}}{\mathrm{GeV}^2}\right]$	$255\ ^{+48}_{-43}$	$204\ ^{+21}_{-20}$	$110\ ^{+13}_{-12}$	29 ± 6	$14\ ^{+5}_{-4}$
η_{SL}	0.906 ± 0.005	0.923 ± 0.003	0.974 ± 0.004	1.097 ± 0.006	1.380 ± 0.013
$\frac{\mathrm{d}\sigma}{\mathrm{d}t}$ $\left[\frac{\mathrm{mb}}{\mathrm{GeV}^2}\right]$	$282\ ^{+48}_{-43}$	$222\ ^{+21}_{-20}$	$113\ ^{+13}_{-12}$	26 ± 6	$10\ ^{+4}_{-3}$

Table 4.3: Measured cross sections for the different bins on $|t|$ and p_t^2. η_{SL} shows the correction for photon momentum. All errors are statistical.

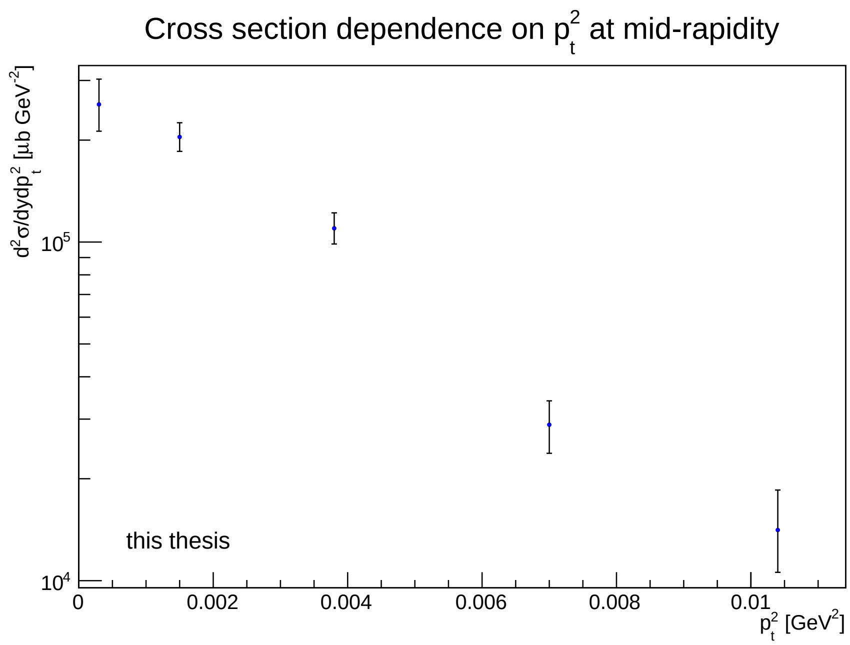

Figure 4.4: Measured cross section dependence on p_t^2 at mid-rapidity.

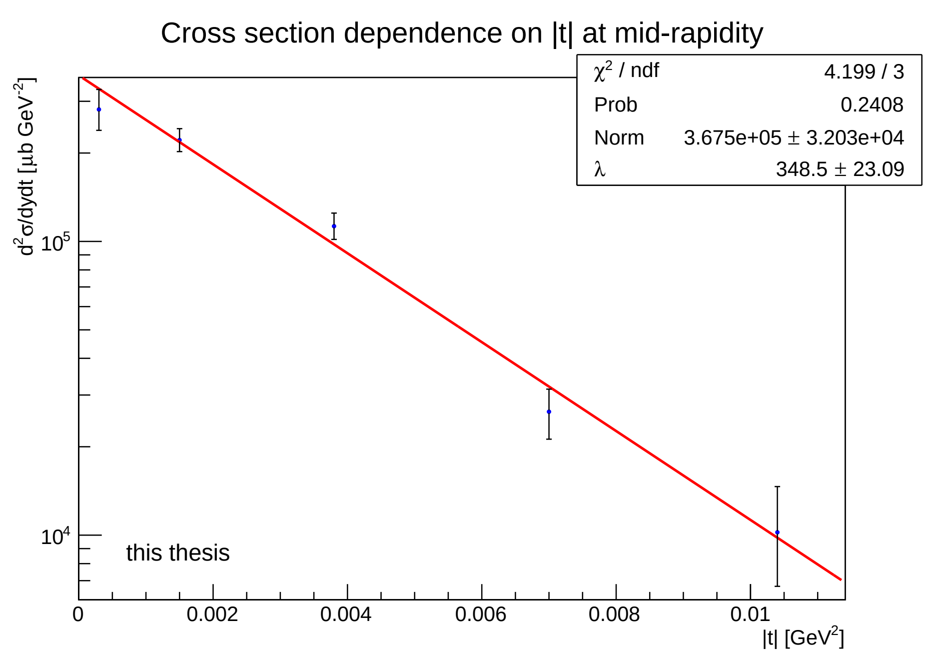

Figure 4.5: An exponential fit of the measured cross section dependence on $|t|$ at mid-rapidity.

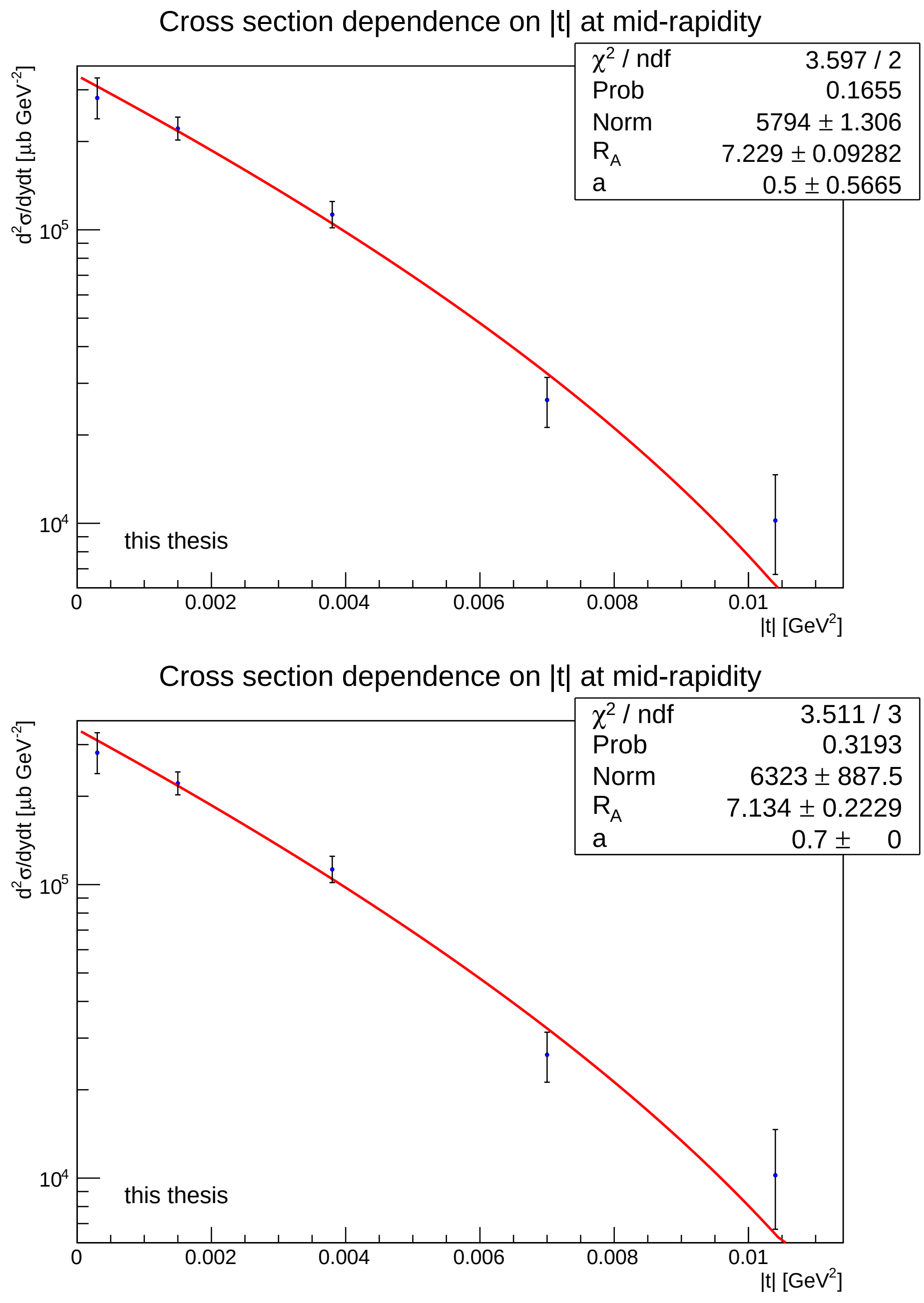

Figure 4.6: Fits of a measured cross section dependence on $|t|$ at mid-rapidity using Eq. 1.11 with no fixed parameter (top) and fixed parameter a (bottom).

Chapter 5

Preparation work on Run 2 data

In this chapter we describe our work on preparations for triggering data in Run 2 UPC and the framework used to calculate luminosity, which we developed for the ALICE collaboration. Both topics go beyond UPC physics. The 0STP trigger is also one of the basic parts of triggers for central diffraction in p-p collisions, while the framework for luminosity can be used for any analysis that requires this information.

5.1 Description of 0STP topological trigger

As we said in Sec. 2.2, the 2015 data were triggered using the 0STP trigger (in the text we will refer to it as the original 0STP). The trigger uses the pixel signals in SPD projected into the (r,ϕ) plane. It tries to build so-called tracklets matching a pixel in the inner SPD layer with one in the outer SPD layer in the same azimuthal region. If at least two of these tracklets are found, it checks if the tracklets are back-to-back in azimuth - the opening angle ϕ must be bigger than 153°. The trigger logic is the following (see Fig. 5.1 for an example):

- there are 2 loops:
  - the outer loop goes over 10 elements (index i),
  - the inner loop goes over 2 elements (index j),
- in every step a new index k is calculated: k = 2*i+j
- the trigger is fired if:

(innerStave[i] OR innerStave[i+1])
AND
(innerStave[i+10] OR innerStave[i+11])
AND
(outerStave[k] OR outerStave[k+1] OR outerStave[k+2])
AND
(outerStave[k+20] OR outerStave[k+21] OR outerStave[k+22])

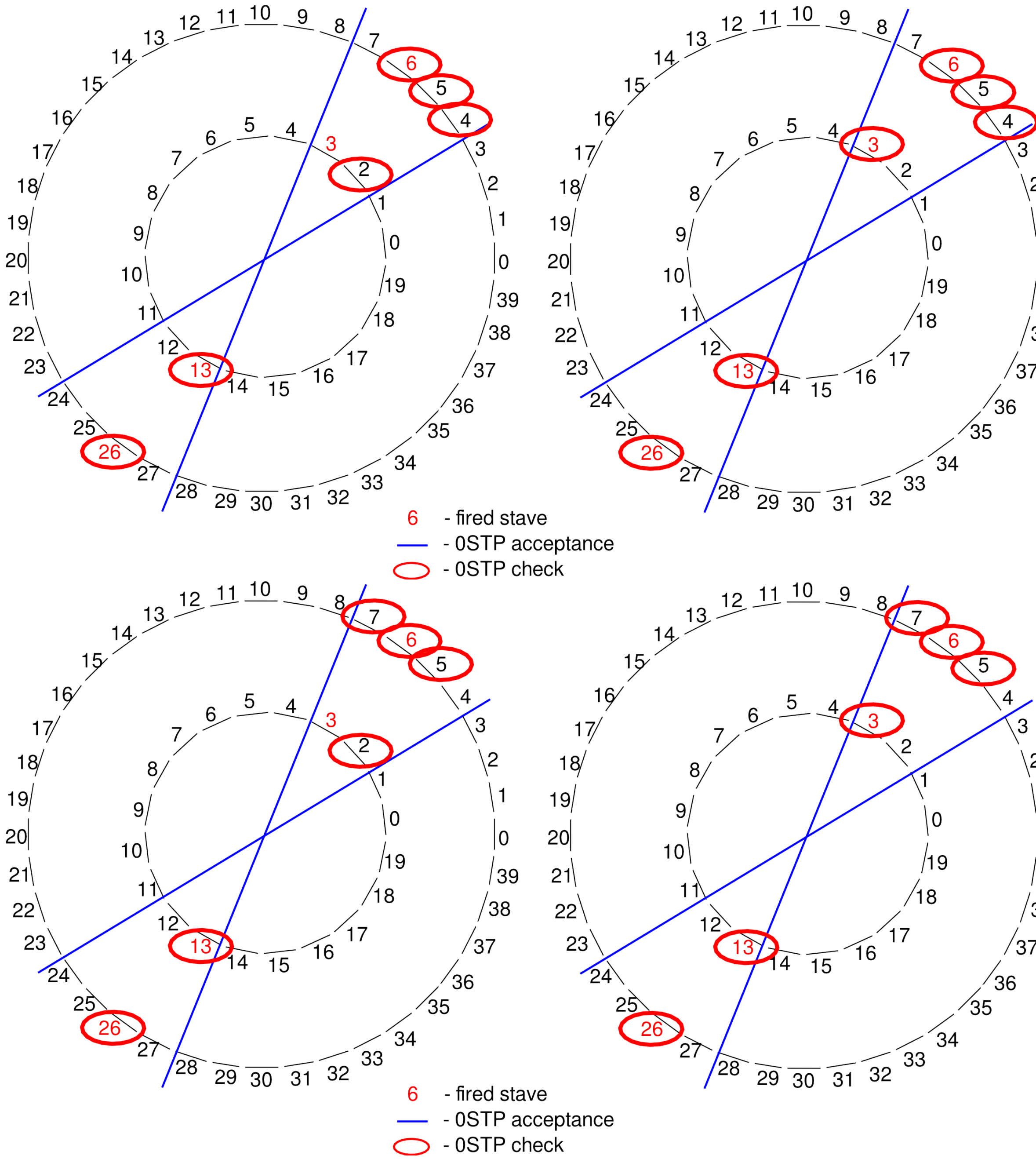

Figure 5.1: An example of the topological 0STP. From left top to right bottom we see, how the algorithm matches the fired staves marked with a red number.

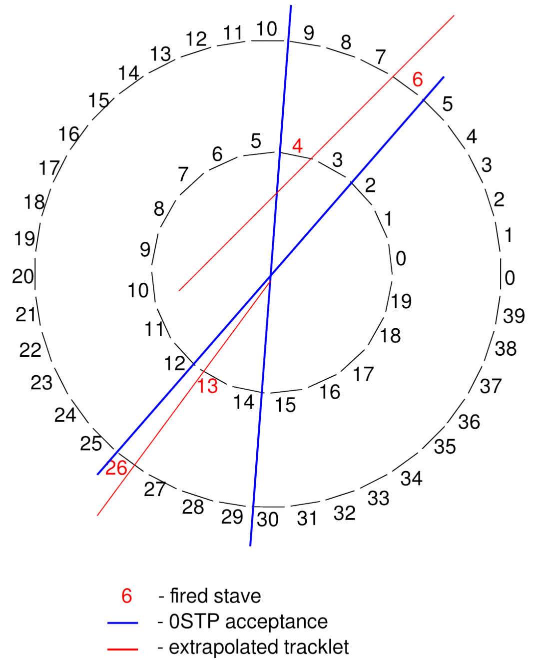

Figure 5.2: An example of an non-physical event, which triggers the 0STP.

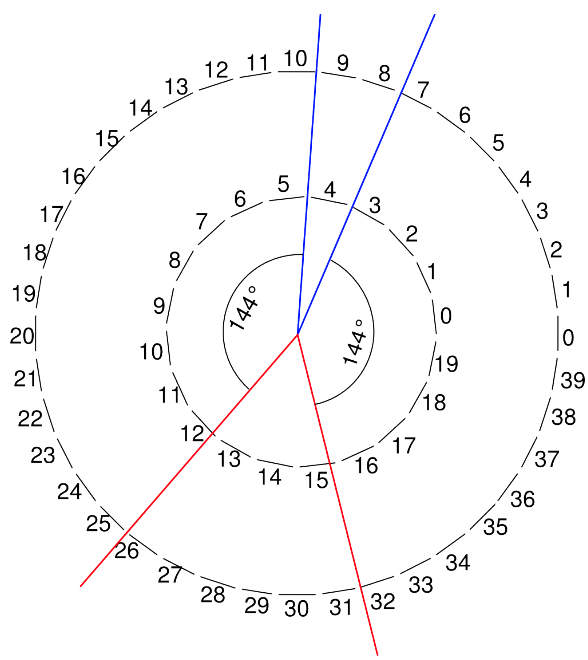

Figure 5.3: The acceptance of the new 0STP logic.

5.1.1 Problems with online Z-vertex trigger

To improve the efficiency of the UPC triggers, we wanted to add a condition on the online Z-vertex, which means, that we do not project all the information into the (r, ϕ) plane, but try to use the full 3D information. We select events, which have tracklets originating from the same position in the Z direction. The first idea was to recover tracklets from the hits in the SPD detector using the 0STP as a first stage of the trigger. Unfortunately, we found two problems, which do not affect the physics obtained from the 0STP trigger, but make it difficult to generalize it.

The first problem is double counting in the 0STP. If we look at Fig. 5.1, we see an example, where inner staves 3 and 13 and outer staves 6 and 26 were fired. Every subfigure shows a part of the algorithm. If all 4 fired staves are in the red ellipses, the algorithm counts it as one pair of tracklets. But as we can convince ourselves on this example, the algorithm will count this one pair twice.

The second problem is illustrated with the help of Fig. 5.2. Here the combination of triggered inner stave 4 and outer stave 6 clearly gives an non-physical event - caused by electrical noise, cosmic radiation or beam-gas hit. But this still fulfils the original 0STP criteria and it will be triggered as an event with a pair of back-to-back particles.

5.1.2 Description of proposal of new 0STP topological trigger

To avoid the problems mentioned in the previous section, we have decided to investigate a change of the logic of the original 0STP. It should go as follows:

- we loop over the first 10 inner staves one-by-one (looking for an 'upper tracklet'),
- if there is a hit, we check the corresponding outer staves, e.g. 2*(inner stave number = i) or 2*(i)+1,
- if we have a coincidence, we start to look for a 'lower tracklet',
- we check, if there is a hit in inner staves, so we look for i+9 or i+10 or i+11,
- if yes, we check corresponding outer staves using the same logic, so e.g. 2*(i+9) or 2*(i+9)+1,
- if all conditions are satisfied, the event passed the new 0STP.

The acceptance of the new logic is shown in Fig. 5.3.

5.2 Testing new trigger logic

Since we have two trigger logics, which we want to compare, we need to test them on an example. We have simulated every possible combination of 4 hits in the SPD detector to study the behavior of both algorithms. Since we are looking for back-to-back tracks, we split the hits in SPD detector in 2 groups. One group represents 'upper tracklets' $(0^\circ < \phi < 180^\circ)$ and the other group stands for 'lower tracklets' $(180^\circ < \phi < 360^\circ)$. In each group we have simulated a hit in the inner layer and a hit in the outer layer.

In other words, the simulation makes a combination of 4 numbers. The numbers represents a hit of the upper tracklet in the inner layer, a hit of the upper tracklet in the outer layer, a hit of the lower tracklet in the inner layer and a hit of the lower tracklet in the outer layer. These combinations are given to both triggers, the original 0STP and the new 0STP.

We have also prepared a small dataset of data measured in lead-lead collisions at 5.02 TeV in run 244918 with the ALICE detector. In this sample we have reconstructed only information from the ITS detector and in total we have 9 231 events.

5.2.1 Results and discussion

Non-physical events

From the total amount of 40 000 combinations, 39 520 did not pass the original criterion. Rejecting 98.8% is not a surprise, since most of the simulated events have no physical meaning. From the rest of the events we checked, if they have a physical meaning. Our condition was, that if there is a hit in the inner layer (i), than there has to be a hit in the outer layer (2i) or (2i+1). If not, than this event has no physical meaning.

At the end we had only 126 good events out of 312 events, which were triggered only once (more in the next subsection). So from the simulated combinations we are picking up around 60% of wrong events. However, in real collisions the ratio of physical and non-physical events could be totally different, so we also repeated the process for measured data. Out of 9231 we had 3438 wrong events. That makes 37.3% of noise or whatever. This is not a negligible number and the new 0STP should fix this problem.

Double counting

Testing the original 0STP on our simulation gave us the exact number of events, which were counted more then once. If we look at the events, which survived the original 0STP criteria, we see, that we have 312 events triggered once, 148 were triggered twice and 20 events even three-times. We also see, that if we would like to use the original 0STP as a base for the online Z-vertex trigger, we will have to face a problem of double counting in 35% of all triggered events.

When we tested the new 0STP, we got some interesting numbers. In total, we have triggered only 112 events, but all of them were triggered once. That means, that this new logic would be a good first stage of the online Z-vertex trigger, but we are clearly missing some events, which the original 0STP do not miss.

In Fig. 5.4 we can see an example of a wanted event, which was triggered by the original 0STP but not by the new logic. As we can see, the new logic compares the minimal possible cone made by one stave of the inner layer and two staves of the outer layer with other 3 small cones on the other side of the SPD detector. This was originally designed to reject non-physical events. But as we can see, we miss events, which would normally fulfil the topological condition. This explains most (maybe all) of the missing events and gives a strong reason to reconsider the logic of the proposed trigger. This work is in progress.

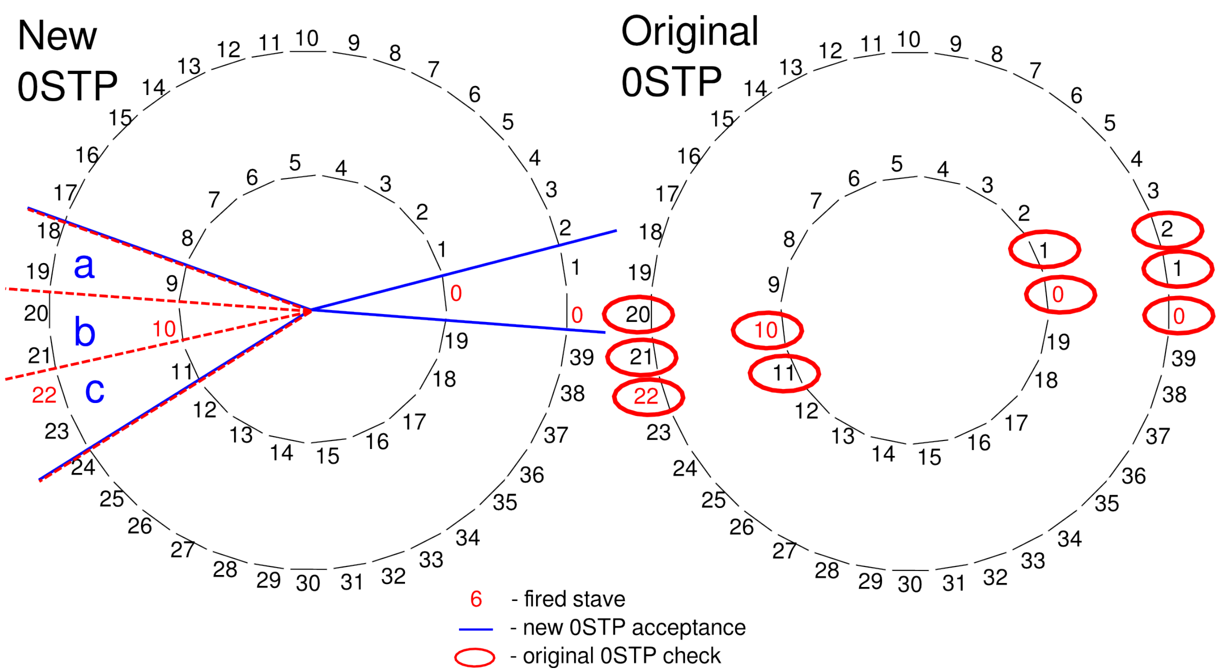

Figure 5.4: A comparison of the new 0STP and the original 0STP.

5.3 Luminosity computation framework

During the summer 2015 we developed a luminosity computation framework for the ALICE collaboration under the supervision of ALICE trigger coordinator Evgeny Kryshen. Next lines document this work.

5.3.1 Introduction

Since the LHC became operational in 2010, the experiment ALICE gathered a lot of physics data, which needed to be analysed. One of the intrinsic inputs for the physics analyses is the luminosity for different trigger classes. Unfortunately, in LHC Run 1 this was not provided to the Collaboration centrally and everyone had to spend extra time on this topic. For the LHC Run 2 we have prepared a new luminosity calculation framework.

The motivation for this effort is to provide a unified and precise luminosity source for ALICE analyses, which can be easily accessed in various formats. This needs a sort of automatic program, which will be periodically launched. A unix-based software utility Cron is used to manage it. Also run/trigger coordinators need up-to-date information. The goal is to provide them with current summaries on collected statistics for different LHC periods.

5.3.2 Theory

To understand the whole concept of this work, we have to describe the ALICE trigger system. The main part of the system is the Central Trigger Processor (CTP), which receives signals (input) from triggering detectors, makes a decision and sends a signal to readout detectors. There are

4 levels of decisions (LM, L0, L1, L2). The application of each of them depends on the speed of propagation of the signal from the triggering detectors to the CTP. Each level has two sets of counters. First, the CTP counts the number of events, LXB, satisfying logical combinations of trigger inputs in a predefined subset of bunch crossings (BC mask). Then an electronic veto, mainly due to busy detectors or downscaling, is applied and results are stored as LXA. Note, that B and A stand for (B)efore and (A)fter veto and X for the level of decision [36].

A well-arranged organization of these signals is crucial for handling these data. Objects, which group readout detectors, are called **clusters**. These have various names and due to hardware conditions we can have only 6 of them per run. Other objects called **classes** group trigger information like descriptor (logical combination of trigger inputs), BC-mask or cluster name. Each class contains informations about LXX counters, which is used for the luminosity calculation. In order to improve this calculation new objects called **aliases** are introduced in the developed framework. Their job is to point to a class with the most precise triggers counts in the trigger cluster [45].

$$L_{Class} = \frac{R^B_{REF}}{\sigma_{REF}} F(\mu_{REF}) \frac{R^A_{Class}}{R^B_{Class}} D \tag{5.1}$$

Eq. 5.1 shows the formula which is used for luminosity calculation. To calculate luminosity one has to know a cross section. Unfortunately a cross section is not known for every subdetector of the ALICE detector, therefore we have to use a reference detector T0, from which we extract reference trigger counts R^B_{REF}, which are connected with L0B or LMB decisions, and the reference cross section $\sigma_{REF} = 39$ [mb], which was estimated for proton-proton collisions at 13 TeV. In August 2015 the Van der Meer scan for the energy of 13 TeV was done and its results will be added to the code once they are available.

The reference trigger counts have to be also corrected for pile-up, which is done by the pile-up function $F(\mu_{REF}) = N\frac{\mu_{REF}}{R_{REF}}$, where N stands for the number of bunch crossings and μ_{REF} is an average number of collisions per bunch crossing. In addition, a correction for fake coincidences in T0A and T0C is applied.

Because we want to calculate the luminosity for each class, we have to compute so-called lifetime of the class first. This is done by the ratio $\frac{R^A_{Class}}{R^B_{Class}}$, where trigger counts of the L2 decision level are taken. We have introduced the aliases in our framework, which means that for each class we replace the used trigger counts with different, more precise ones. But the classes from the same cluster can have a different downscaling factor. Therefore a variable D is also defined in Eq. 5.1 and stands for the ratio of downscalings of the original class and the alias class.

5.3.3 Implementation

A program which can extract informations from OCDB files, calculate luminosity and produce graphical output in various format was built. This consists of several macros written mostly in C++ language. Their dependency tree is shown in Fig. 5.5. A control macro, which inherits all files is named *runCollectTriggerInfo.C*. It can be run in 4 different modes, depending on which value of the argument (switch) is used. The default argument '0' is used to run standard mode, where a list of runs, which will be analysed, is extracted automatically to the file *addtolist.txt*. An argument '1' uses as an input a list of preselected runs, which are written in a file *selecte-drunlist.txt*. The other two switches can be used for testing, where the program with an input

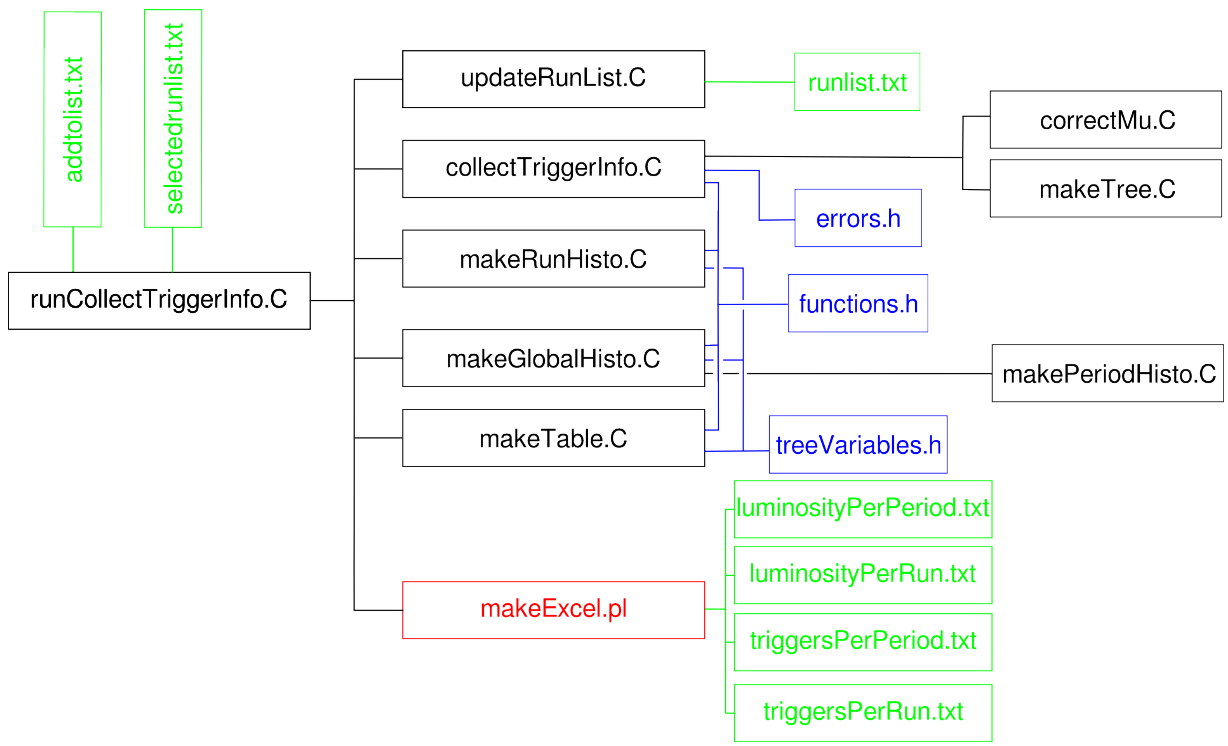

Figure 5.5: Dependency tree of the code. Object functionalities are explained in the text.

argument '2' uses a short list of chosen runs (from different periods) and the argument '3' serves only for a single run level diagnostic.

The most important is the default setting of the program. This will first run an *updateRunList.C* macro. Its job is to mount a source of OCDB files via cvmfs, extract names of all runs in the source folder, using a list of already analysed runs from *runlist.txt* choose non-analysed (new) ones and return a list of them in the file *addtolist.txt*.

Next a loop over new runs is initialized. For each new run a macro *collectTriggerInfo.C* is started. This is the part of the code, where the luminosity calculation is done. The OCDB files are used as a source of information needed for the calculation as mentioned above. In order to make the code better readable headers *errors.h* and *functions.h* are provided, which contain error messages and various subprocess functions respectively. A macro *correctMu.C*, provided by Martino Gagliardi, is used for the computation of the pile-up. In the end this macro calls *makeTree.C*, which saves all extracted and computed informations to a ROOT file in a TTree structure on a run level [41].

Another macro called *makeRunHisto.C* is triggered in the loop. The purpose of this one is to make a run level output, which means, that it creates a folder, where all files connected with the specific run will be stored and run level plots are made. Here, headers *functions.h* and *treeVariables.h* are used, where the second one serves as a global source of variables, which can be found in the ROOT file. At the end of the loop the ROOT file is moved to the created folder.

When the analysis of new runs is done, all run level ROOT files are merged to a global ROOT file called *triggerInfo.root*, which is used as a source for a global analysis, which is executed in a

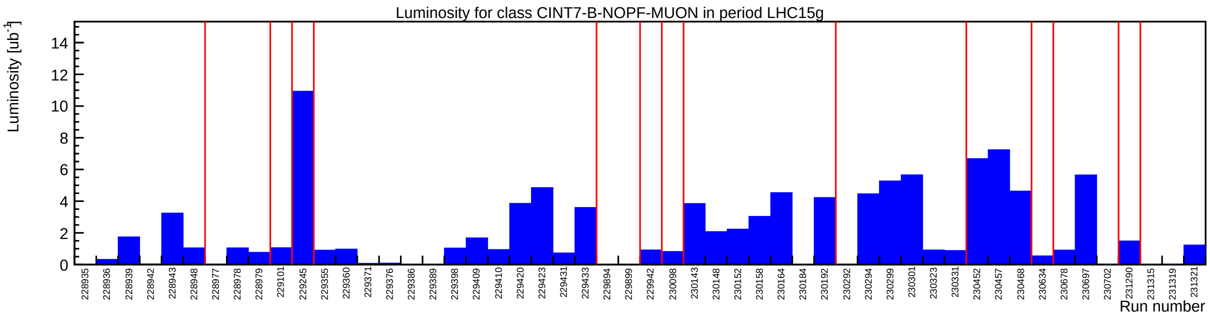

Figure 5.6: Luminosity of a specific class per run in a period LHC15g. Red lines surround runs obtained from the same LHC fill.

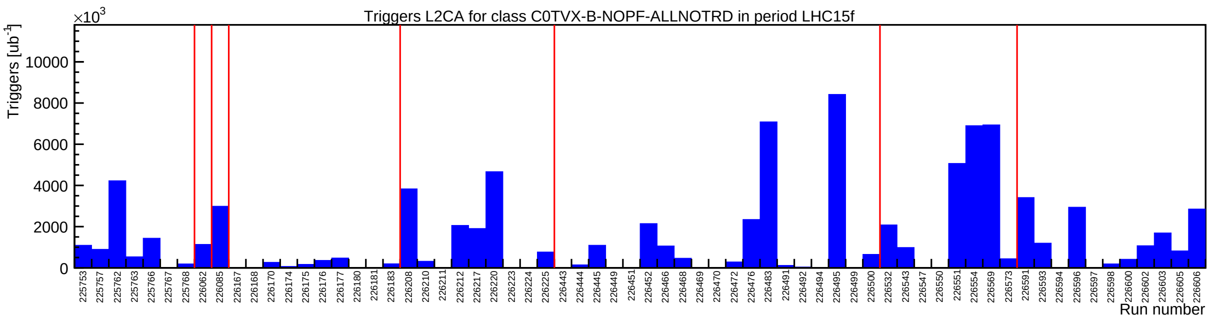

Figure 5.7: Triggers L2A per run in the period LHC15f. Red lines surround runs obtained from the same LHC fill.

macro *makeGlobalHisto.C*. Results of this macro are plots of different variables dependent on a run number, which are printed in pdf files. At the end of the macro another macro *makePeriodHisto.C* is initialized in a loop over periods and makes similar plots, but delimited on the specific period runs only.

Macros *makeTable.C* and *makeExcel.pl* serve to create summaries of the luminosity and the triggers in a period. The first one loads the global ROOT file, sums luminosity and L2A triggers through runs of one period for each period and stores it to text files. Similar text files are also produced for the luminosity and the triggers for each run. These text files are used as source files for the second macro, written in perl language [46]. Its only purpose is to transform the text files to one xls file *triggerInfoTable.xls* in a form of excel tables.

5.3.4 Results

One of the most important results is the automatisation of the whole process. The cronjobs, which trigger a script at a specific time, were used for this purpose. In our case, we use 2 shell scripts. The first one called *newruncheck* starts the program, which performs the analysis. The second one called *croncopy* copies the whole folder with the program and its results to my personal web page [47], where results are available for an external usage. We should also mention, that this is just a temporary solution and in the future we would like to provide luminosity and collected statistics class-by-class and run-by-run in OADB and Monalisa.

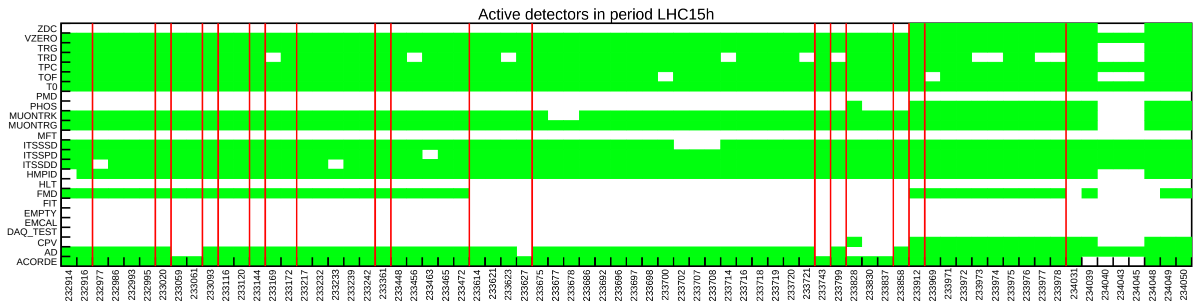

Figure 5.8: A list of active detectors per run in period LHC15h. Red lines surround runs obtained from the same LHC fill.

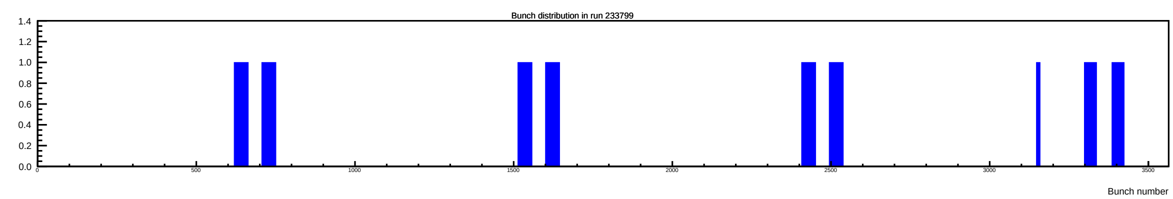

Figure 5.9: An example of a run level analysis. The bunch distribution for the run 233799.

	List of ALICE Trigger Codes			Version no. 31_7_2015					
	Luminosity [ub^-1] per run (for each class)								
Run	mu	Bunches	Start_date	Start_time	Run_duration	Period	CTRUE-B-NOPF-ALLNOTRD	C0TVX-B-NOPF-ALLNOTRD	CINT5-B-NOPF-ALLNOTRD
225753	0,0217032	6	2015-06-07	21:42:12	4559	LHC15f	0,03	28,44	28,44
225757	0,0224442	6	2015-06-07	23:02:32	3663	LHC15f	0,02	23,37	23,37
225762	0,022902	6	2015-06-08	00:08:45	6691	LHC15f	0,05	54,84	45,64
225763	0,0218501	6	2015-06-08	02:04:27	962	LHC15f	0,01	7,01	5,88
225766	0,0227351	6	2015-06-08	02:28:08	2284	LHC15f	0,02	18,67	15,55
225767	0,0236907	6	2015-06-08	03:10:58	8	LHC15f	0	0	0
225768	0,0240617	6	2015-06-08	03:14:48	386	LHC15f	0	2,51	2,1
226062	0,000953197	15	2015-06-10	00:27:32	5928	LHC15f	0,01	14,64	14,61
226085	0,00243139	15	2015-06-10	05:43:07	7707	LHC15f	0,01	38,47	38,47
226167	0,00447607	15	2015-06-10	22:08:25	122	LHC15f	0	0	0
226168	0,00450087	15	2015-06-10	22:15:21	131	LHC15f	0	0	0
226170	0,00438547	15	2015-06-10	22:24:46	639	LHC15f	0	3,51	3,51
226174	0,00475168	15	2015-06-10	22:46:54	232	LHC15f	0	0,91	0,91
226175	0,0044179	15	2015-06-10	22:58:01	403	LHC15f	0	2,23	2,23
226176	0,00484228	15	2015-06-10	23:09:54	1485	LHC15f	0	9,38	0
226177	0,0110955	15	2015-06-10	23:39:37	1592	LHC15f	0	12,35	0
226180	0,0107484	15	2015-06-11	00:25:23	10	LHC15f	0	0	0
226181	0,0132279	15	2015-06-11	00:31:40	7	LHC15f	0	0	0
226183	0,0109334	15	2015-06-11	00:36:50	720	LHC15f	0	5,23	0
226208	0,0114322	15	2015-06-11	05:05:31	12551	LHC15f	0,02	98,84	0
226210	0,0112023	15	2015-06-11	08:47:40	1079	LHC15f	0	8,35	0
226211	0,0117202	15	2015-06-11	09:11:24	9	LHC15f	0	0	0
226212	0,0116086	15	2015-06-11	09:18:06	6711	LHC15f	0,01	53,11	0
226217	0,0112205	15	2015-06-11	11:15:33	6369	LHC15f	0,01	49,23	0
226220	0,0115657	15	2015-06-11	13:08:43	7706	LHC15f	0,01	60,32	60,32
226223	0,0113416	15	2015-06-11	15:32:16	11	LHC15f	0	0	0
226224	0,0134721	15	2015-06-11	15:44:46	8	LHC15f	0	0	0
226225	0,0114779	15	2015-06-11	15:51:26	1332	LHC15f	0	9,94	9,94
226443	0,0116601	11	2015-06-12	22:25:01	7	LHC15f	0	0	0
226444	0,0112453	11	2015-06-12	22:32:32	382	LHC15f	0	1,94	1,94
226445	0,0122066	11	2015-06-12	22:45:04	1883	LHC15f	0	14,19	14,19
226449	0,0126376	11	2015-06-12	23:30:07	6	LHC15f	0	0	0
226451	0,0119481	11	2015-06-12	23:36:10	7	LHC15f	0	0	0
226452	0,0130134	11	2015-06-12	23:41:28	3627	LHC15f	0,01	27,76	27,76
226466	0,0121064	11	2015-06-13	00:53:24	1830	LHC15f	0	13,72	13,72
226468	0,012815	11	2015-06-13	01:36:42	807	LHC15f	0	6,07	6,07
226469	0,0134082	11	2015-06-13	01:55:26	21	LHC15f	0	0,13	0,13
226470	0,0131488	11	2015-06-13	02:00:49	10	LHC15f	0	0	0
226472	0,0126281	11	2015-06-13	02:06:23	768	LHC15f	0	3,73	3,73
226476	0,0126357	11	2015-06-13	02:34:18	3954	LHC15f	0,01	30,32	30,32
226483	0,0126672	11	2015-06-13	03:48:24	11944	LHC15f	0,02	91,49	91,49
226491	0,0127673	11	2015-06-13	07:11:41	210	LHC15f	0	1,57	1,57
226492	0,0125613	11	2015-06-13	07:19:42	79	LHC15f	0	0,56	0,56
226494	0,0117259	11	2015-06-13	07:43:51	10	LHC15f	0	0	0

Figure 5.10: An example of summary statistics in an excel table. The luminosity of each class per run with additional informations.

As mentioned before, the main task is to calculate luminosity for each class and provide these results in various formats. An example of a graphical output is shown in Fig. 5.6. On this plot one can see the calculated luminosity for class CINT7-B-NOPF-MUON for runs from the LHC15g period only. Our framework provides these plots for every class per every LHC period.

Another important information is the number of collected triggers per class extracted from L2A counts. A nice example can be seen in Fig. 5.7, where class C0TVX-B-NOPF-ALLNOTRD serves as a demonstration. Again, such plots are made for all classes and all periods.

The last but not least product of global statistics are plots of miscellaneous variables and their dependencies on the run number. Fig. 5.8 serves as an example of this. Green fields represent ALICE subdetectors, which were on during a specific run. The program makes these plots for every LHC period.

Not only global statistics are made, but also run level information is obtained and stored in the form of histograms. An example bunch crossing distribution is shown in Fig. 5.9, which is created for every run. Many other plots can be made on request.

Run/trigger coordinators will appreciate the last important result of this program - a summary of luminosities and triggers for each class per run or per LHC period organized in well-arranged excel tables. A snapshot of this file is shown in Fig. 5.10 and the original file can be found on the mentioned webpage under the name *triggerInfoTable.xls*. As the file is periodically updated, the coordinators have fresh information on the collected statistics.

Chapter 6

Analysis of Run 2 data

In this chapter we explain the technical problems that have delayed the calibration of Run 2 data and impeded a full analysis of these data now. In the next section we show our results on the first low intensity runs of Pb-Pb collisions in 2015.

6.1 Data acquisition in autumn 2015

As it is written in more detail before in this thesis, we want to study UPC Pb-Pb collisions to measure coherent J/ψ production off nuclear targets. The experiment ALICE at the LHC collected data with UPC triggers twice - in the years 2011 and 2015. The main difference between these two data taking periods is the total incident energy and the luminosity delivered by triggers. While the total energy was 2.76 (5.02) TeV in 2011 (2015), the total luminosity in 2011 for the trigger CCUP4 was $22.4^{+0.9}_{-1.2}$ μb^{-1} [43] and in 2015 for the trigger CCUP8 was 138.8 μb^{-1} [48]. The recorded growth of delivered luminosities for some relevant triggers is in Fig. 6.1.

First, we were analyzing the 2011 data and the complete software implementation was done with these data. We also present results of our measurement on these data in this thesis. One of our tasks was to measure the data collected in 2015, but due to technical problems described in Sec. 6.1.1, we cannot do our measurement yet with the full delivered luminosity. What we can is to roughly predict the total yield of J/ψ particles we want to analyze. Based on luminosity the yield should increase by factor 6.2. Furthermore the higher energy implies a higher flux of photons at mid-rapidity, which increases the UPC cross section in some 60%. Finally we have the AD detector which rejects better background events and helps with the stability of the trigger. All together we expect to have approximately 8 times higher statistics in 2015 data.

6.1.1 TPC distortions

The reconstruction of events measured at mid rapidity needs a full understanding of central barrel detectors, such as TPC. As the TPC is a gaseous type detector and depends on the drift speed of ions in the medium, it needs a lot of corrections for distortions caused by slow ions. Due to the higher energy, the larger rate and a new gas mixture we have 4-6 times larger distortions in Run 2 [49, 50].

In Fig. 6.2 we can see an example of runs with different interaction rates. The green areas exhibit small distortions (which can be scaled as predicted in simulations) but red and blue

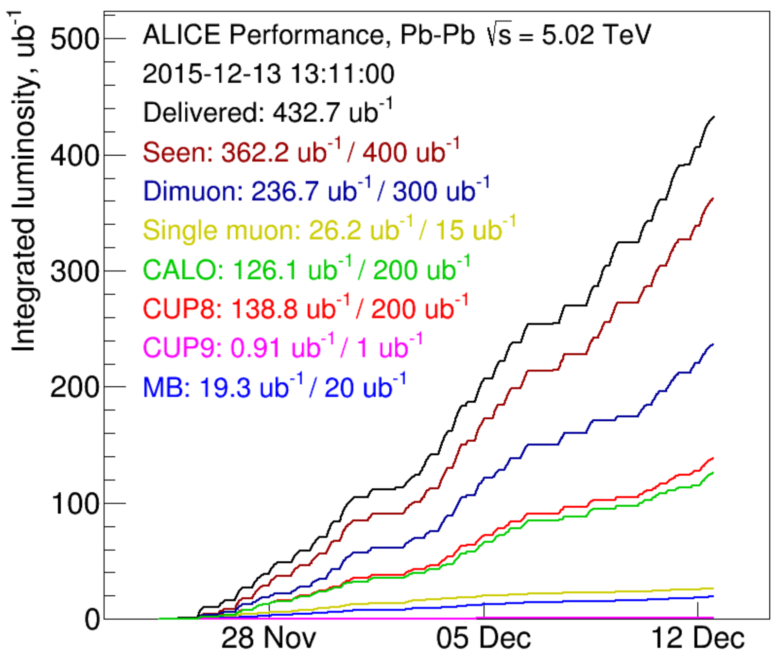

Figure 6.1: Integrated luminosities as a function of time for selected triggers. The trigger CCUP8 is designed for the type of UPC studies described in this thesis. Taken from Ref. [48]

regions represent large distortions. There are two types of large distortions. The first type is in the outer TPC cylinder in the middle of the sub-volume and it is explained by a floating gating grid wire. The second type is close to the sector edges of the inner TPC cylinder and cannot by linked with static distortions from wrong potential setting or a floating object.

The only explanation for the second type of distortions is leakage of ions to the detector volume. A team delegated to investigate the difference of measured distortions and expected distortions came with a possible explanation based on an incident from July 4, when the gas mixture in TPC was contaminated. The contaminant may lead to the creation of ionized heavy objects in the amplification region. These objects slowly drift to cathodes, which in leaky regions produce a deposit on the central electrode. This modifies the quantum efficiency of the surface of the central electrode.

The ALICE PWG-PP team is performing a correction method, which is based on interpolation of a track from detectors surrounding the TPC (this is shown in Fig. 6.3). First, the method reconstructs a TPC track with large road-widths. Then it matches the track with ITS and TRD/TOF signals (marked as red dots in the figure). Next it refits ITS-TRD-TOF points and interpolates a TPC true track (red line) with TPC reference points (green dots). In the end it saves a correction made by differences between reference points and distorted clusters (blue dots). In addition, distortions are changing with time due to the change on the interaction rate with time, so this procedure needs to be repeated in short time intervals. Currently, maps of corrections are done for each 20 min interval of the 2015 data taking period. This is a time consuming process and explains, why we can fulfill only partially the last assignment of this thesis.

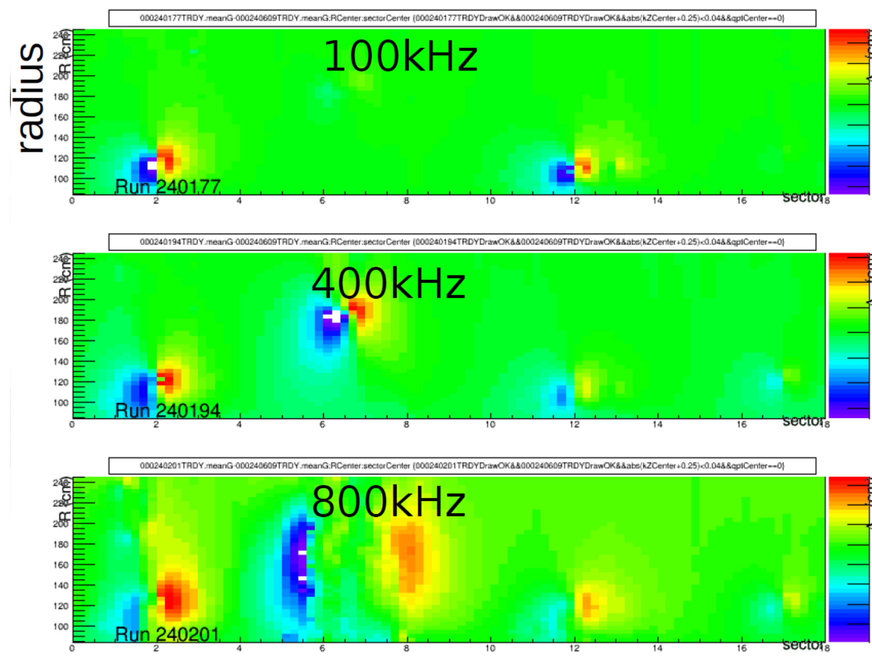

Figure 6.2: Interaction rate scans of proton-proton 2015 collisions. Blue and red spots show large distortions in the TPC detector. Taken from Ref. [49].

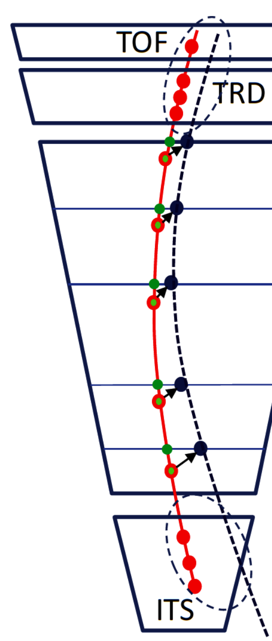

Figure 6.3: Scheme of the correction method based on interpolation using signals from ITS and TRD/TOF detectors. Taken from Ref. [50].

6.1.2 Low intensity runs

In May 2016 we have available uncorrected data from low intensity runs only. It has been seen that the distortions are not so large in this data set. We were able to reconstruct tracks from these runs due to the low interaction rate. But it has to be stressed that the analysis has to be repeated once the data is properly calibrated. To show that our framework is ready, we took a data set, which was prepared in AOD train PWGUD/UD_PbPb_AOD/72_20160317-1648. This sample contains 56 888 pre-selected events. Our only selection criteria were conditions on CCUP8 trigger, which was described in Sec. 2.2, $p_t < 200$ MeV/c to restrict ourselves to coherent production and the mass of the di-lepton being larger than 1.8 GeV/c^2. These cuts accept 64 events.

Due to the low statistics we did not apply any condition on identification of particle. In Fig. 6.4 we show the energy loss of one particle against the energy loss of the other particle in each event. As we can see, points are roughly grouped in two regions. The region with a lower energy loss should represent muons, while the other region should stand for electrons. These two regions are populated approximately equally, which is in agreement with their branching ratios, which are comparable [19]. Similar figures have been shown in previous UPC analysis. See for example Fig 1. of [1].

In Fig. 6.5 we have the invariant mass distribution. In the mass region [3.0;3.2] GeV/c^2 we see 13 events, which can be considered to be J/ψ candidates. The fit with the Crystall-Ball function of the mass distribution is shown in Fig. 6.6. It gives us 9 J/ψ particles in total. The delivered luminosity for these low intensity runs was calculated to be 0.6 μb^{-1}. It is worth noting the one event with mass around 9.5 GeV/c^2, which is compatible with Υ, but in this region we also expect a sizeable contribution from $\gamma\gamma \rightarrow \mu\mu$ events.

In Figs. 6.7 and 6.8 we show p_t and p_t^2 distributions of the low intensity runs. The reason why we show them is nothing less than to prove, that the built machinery is ready to produce results when it gets an input.

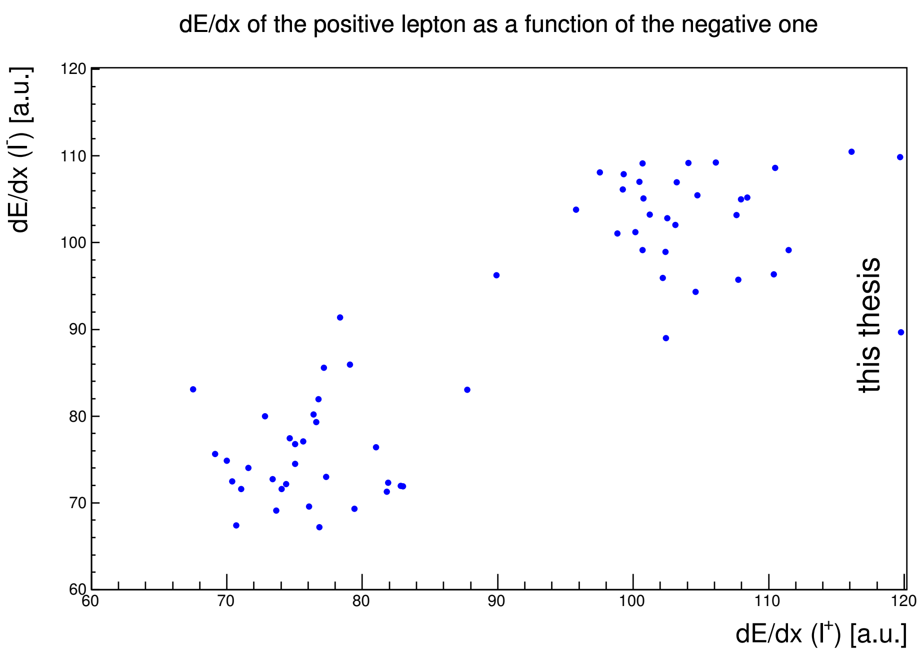

Figure 6.4: Energy loss $\mathrm{d}E/\mathrm{d}x$ in TPC for the low intensity runs in Pb-Pb collisions in 2015 for the CCUP8 sample..

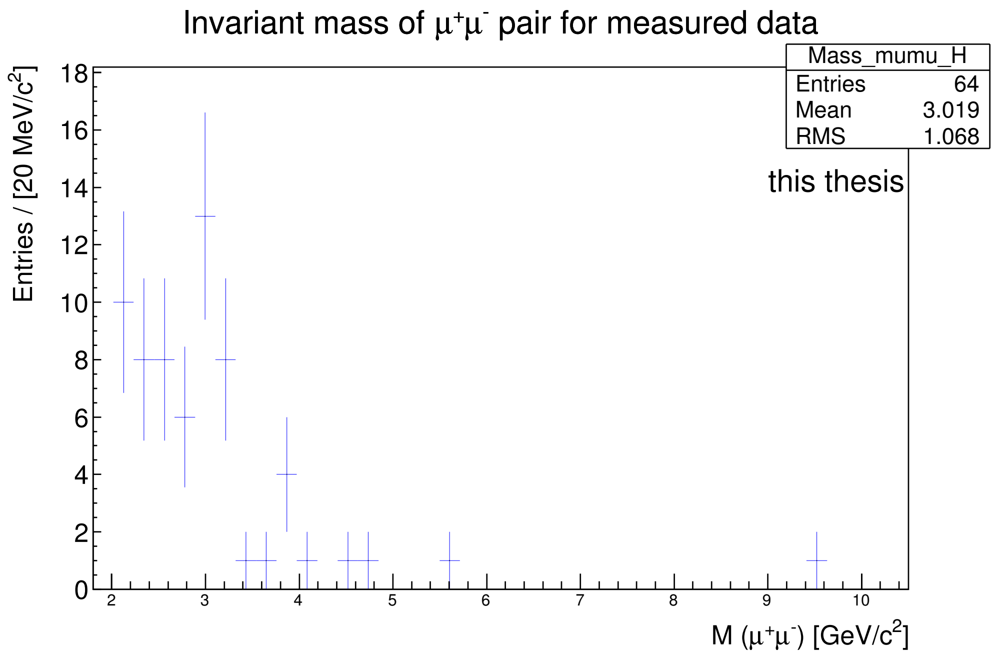

Figure 6.5: Mass distribution of di-muon candidates recorded with the CCUP8 trigger in the low-intensity runs from 2015 Pb-Pb collisions.

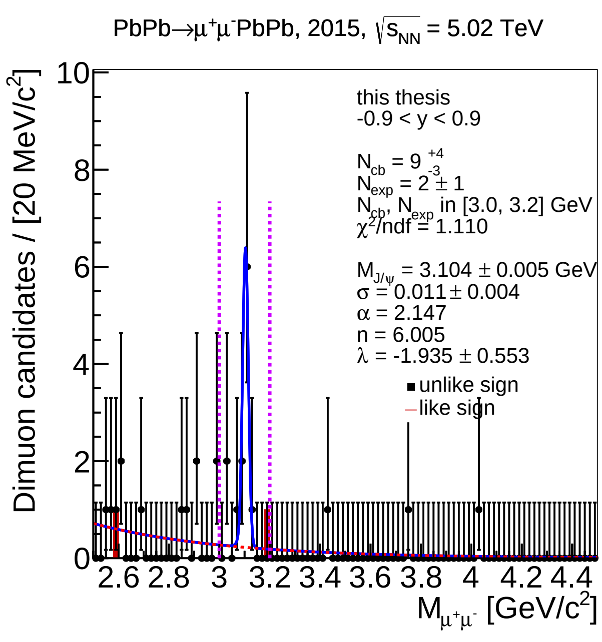

Figure 6.6: A fit of the mass distribution of di-muon candidates recorded with the CCUP8 trigger in the low-intensity runs from 2015 Pb-Pb collisions.

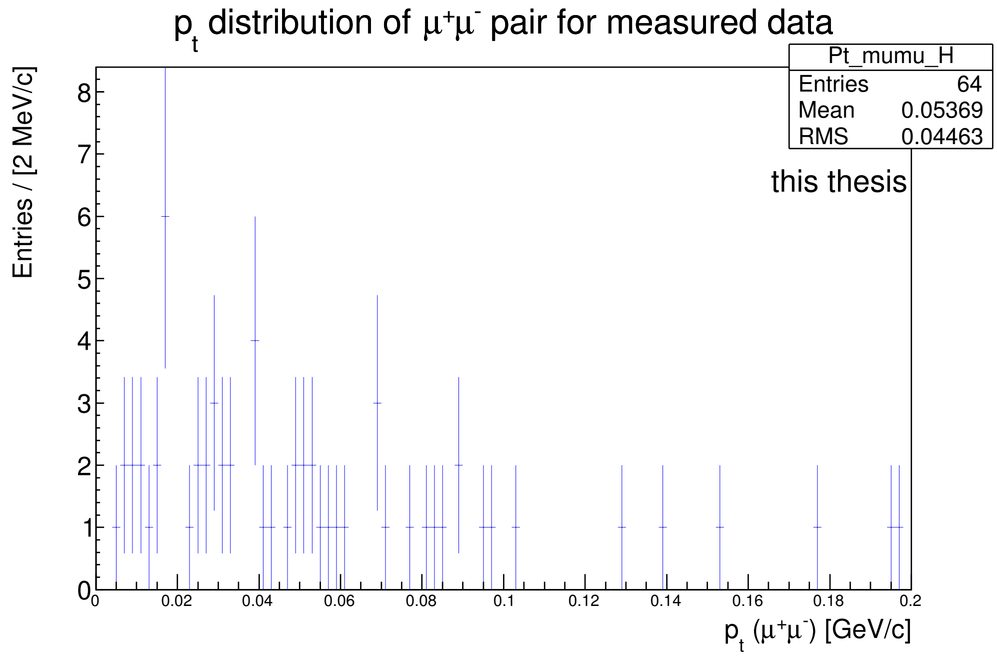

Figure 6.7: p_t distribution of di-muon candidates recorded with the CCUP8 trigger in the low-intensity runs from 2015 Pb-Pb collisions..

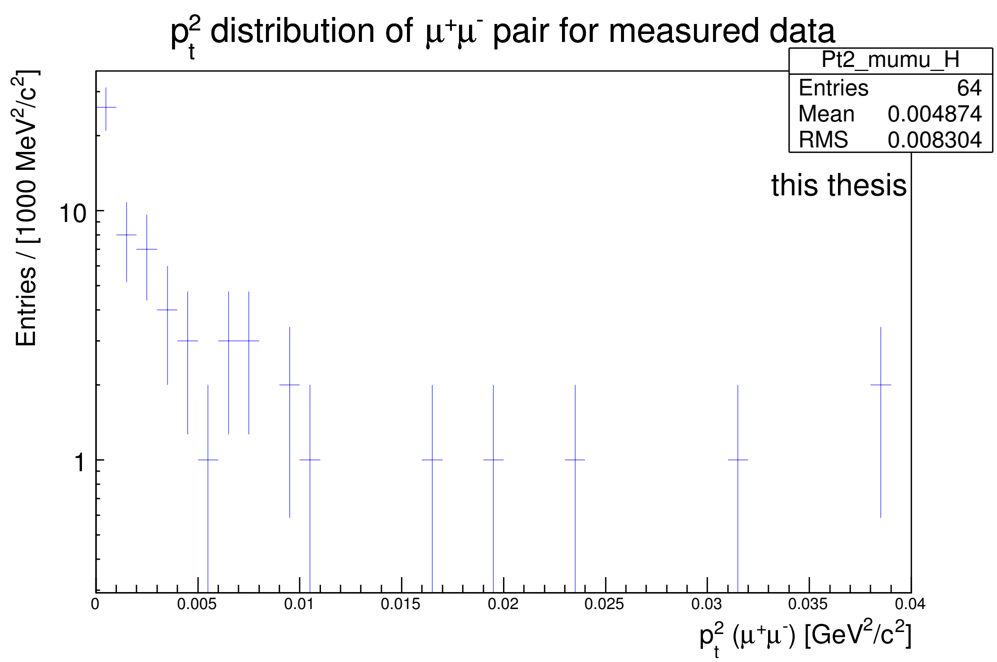

Figure 6.8: p_t^2 distribution of di-muon candidates recorded with the CCUP8 trigger in the low-intensity runs from 2015 Pb-Pb collisions.

Chapter 7

Summary

Small-x physics is an interesting subject of study. A lot of work has been done by H1 and ZEUS Collaborations from data obtained at HERA [12]. Although the LHC facility was not primary built to continue with these studies, ultra-peripheral collisions give an opportunity to do so. The rapidity dependence of the cross section at LHC energies of Run 1 has been measured [1] and this measurement is briefly described in Sec. 1.7. We have repeated this measurement with partial success. The calculation of the dependence of the cross section on transferred momentum p_t^2 was also done with Run 1 data for the first time. Descriptions of the different LHC runs, energies, the experiment ALICE and the process of data mining from collision to AOD files over UPC triggers were mentioned in Chapter 2.

First in our measurement, we had to understand the available data and pick the right selection criteria. The impact of these cuts on original data are in Tabs. 3.1, 3.2 and 3.3. Plots of mass, p_t and p_t^2 distributions can be found in Figs. 3.1-3.6.

The important part of correcting the measured data to measure the cross section is accomplished with simulated Monte Carlo data. The influence of the ALICE detector performance is introduced in Sec. 3.3.2 and the results are presented in Fig. 3.13 and Sec. 3.6. A deviation of our result from the published measurement by factor of 4, which propagates to our other results, indicates, that we have to investigate more the acceptance × efficiency procedure.

Because we deal with a small number of measured events in Run 1, we had to also think out the best binning order. This is described in Sec.3.3.4 and the resulting plots are in Figs. 3.7. At the end we have decided to distribute our data in 5 bins, which is written in Sec. 3.4.

In order to recover the transferred momentum $|t|$ from data, we have calculated a correction on the photon momentum. This is explained in Sec. 3.3.3 and results are discussed in Sec. 3.5.

Next, we have performed fits of the Monte Carlo coherent data to recover the numbers used by STARlight. Using the form factor with fixed range of Yukawa potential $a = 0.7$ fm, we came up with an average value of $R_A = (6.70 \pm 0.26)$ fm. This result is very close to the theoretical one and we have found that our corrections are good enough to be used on measured data. More details in Sec. 3.7.

We have also measured the differential cross section for Run 1 data. The whole story is in Chapter 4. The main result is, that we have measured 314 $^{+20}_{-19}$ J/ψ particles, which we have corrected for the fraction of incoherent events (see Sec. 4.2) and for feed-down as discussed in Sec. 4.3. The cross section dependences on p_t^2 and $|t|$ are in Tab. 4.3 and Fig. 4.4. The $|t|$-dependence of the cross section was also fitted with the model used in STARlight (Fig. 4.6) and with a simple exponential function (Fig. 4.5). The corresponding discussion can be found in Secs. 4.4 and 4.5. We have also computed the p_t^2-integrated cross section at mid-rapidity and found $\mathrm{d}\sigma^{\mathrm{coh}}_{\mathrm{J}/\psi}/\mathrm{d}y = 0.98^{+0.07}_{-0.06}(\mathrm{sta})$ mb.

This thesis was originally supposed to work with Run 2 data. Chapters 5 and 6 are dedicated to it. In Sec. 5.1 and Sec. 5.2 our work on UPC triggers is described. We have also developed a luminosity computation framework, which can daily automatically update information on luminosity collected with the ALICE detector classes. Results are accessible to the whole collaboration and serve well the run/trigger coordinators. This was done under the supervision of ALICE trigger coordinator Evgeny Kryshen and its description is in Sec. 5.3.

In Chapter 6 we explained, why we could not do a full measurement of Run 2 data and show the first results (see Fig. 6.5) from low intensity runs to demonstrate, that our developed software is ready to be used when the full Run 2 data will be available. We have also extracted the number of J/ψ particles in these runs and the integrated luminosity, which was compared to the total integrated luminosity of Run 2.

In conclusion, we have prepared a tool to measure differential cross section of coherent J/ψ production in Pb-Pb UPC. This was tested on Run 1 data and the integral over p_t^2 of our measurements was compared to the published measurement. We have found out some discrepancies, which have not been understood yet, so we state our results to be preliminary.

In the short future we are going to explain or correct the discrepancies and publish our results in the ALICE collaboration as an analysis note. When data and simulations of Run 2 will be available, we will use them to repeat this measurement and to compare the p_t^2 distribution of coherent photoproduction of J/ψ at two different values of Bjorken x.

Bibliography

[1] E. Abbas *et al.* [ALICE Collaboration], Eur. Phys. J. C **73** (2013) 11, 2617 [arXiv:1305.1467 [nucl-ex]].

[2] M. Broz [ALICE Collaboration], AIP Conf. Proc. **1654** (2015) 100005. doi:10.1063/1.4916016

[3] B. Abelev *et al.* [ALICE Collaboration], Phys. Lett. B **718** (2013) 1273-1283 doi:10.1016/j.physletb.2012.11.059

[4] G. Christopher, "Elementary particle physics in a nutshell," ISBN: 978-0-691-13116-0

[5] G. Aad *et al.* [ATLAS Collaboration], Phys. Lett. B **716** (2012) 1 doi:10.1016/j.physletb.2012.08.020 [arXiv:1207.7214 [hep-ex]].

[6] S. Chatrchyan *et al.* [CMS Collaboration], Phys. Lett. B **716** (2012) 30 doi:10.1016/j.physletb.2012.08.021 [arXiv:1207.7235 [hep-ex]].

[7] F. Halzen, A. Martin, "Leptons and quarks: An introductory course in modern particle physics," ISBN: 0-471-88741-2

[8] W. N. Cottingham, D. A. Greenwood "An introduction to the Standart Model of particle physics," ISBN-13: 978-0-521-85249-4

[9] H. D. Politzer, Phys. Rev. Lett. **30** (1973) 1346. doi:10.1103/PhysRevLett.30.1346

[10] D. J. Gross and F. Wilczek, Phys. Rev. Lett. **30** (1973) 1343. doi:10.1103/PhysRevLett.30.1343

[11] A. Accardi *et al.*, arXiv:1212.1701 [nucl-ex].

[12] H. Abramowicz *et al.* [H1 and ZEUS Collaborations], arXiv:1506.06042 [hep-ex].

[13] S. Chekanov *et al.* [ZEUS Collaboration], Eur. Phys. J. C **24** (2002) 345 doi:10.1007/s10052-002-0953-7 [hep-ex/0201043].

[14] S. A. Kulagin and R. Petti, Phys. Rev. C **82** (2010) 054614 [arXiv:1004.3062 [hep-ph]].

[15] J. G. Contreras and J. D. Tapia Takaki, Int. J. Mod. Phys. A **30** (2015) 08, 1542012.

[16] S. Munier, A. M. Stasto and A. H. Mueller, Nucl. Phys. B **603** (2001) 427 doi:10.1016/S0550-3213(01)00168-7 [hep-ph/0102291].

[17] J. J. Aubert *et al.* [E598 Collaboration], Phys. Rev. Lett. **33** (1974) 1404. doi:10.1103/PhysRevLett.33.1404

[18] J. E. Augustin *et al.* [SLAC-SP-017 Collaboration], Phys. Rev. Lett. **33** (1974) 1406 [Adv. Exp. Phys. **5** (1976) 141]. doi:10.1103/PhysRevLett.33.1406

[19] K. A. Olive *et al.* [Particle Data Group Collaboration], Chin. Phys. C **38**, 090001 (2014) and 2015 update.

[20] S. S. M. Wong, "Introductory nuclear physics," ISBN: 978-0-471-23973-4

[21] R. Vogt, "Ultrarelativistic heavy-ion collisions," ISBN: 978-0-444-52196-5

[22] C. Battilana, "CMS Muon Results" `https://twiki.cern.ch/twiki/bin/view/CMSPublic/PhysicsResultsMUO` [cited on 26.4.2016].

[23] A. J. Baltz, G. Baur, D. d'Enterria, L. Frankfurt, F. Gelis, V. Guzey, K. Hencken and Y. Kharlov *et al.*, Phys. Rept. **458** (2008) 1 [arXiv:0706.3356 [nucl-ex]].

[24] C. A. Bertulani, S. R. Klein and J. Nystrand, Ann. Rev. Nucl. Part. Sci. **55** (2005) 271 [nucl-ex/0502005].

[25] G. Baur, K. Hencken, D. Trautmann, S. Sadovsky and Y. Kharlov, Phys. Rept. **364** (2002) 359 doi:10.1016/S0370-1573(01)00101-6 [hep-ph/0112211].

[26] A. Cisek, W. Schafer and A. Szczurek, Phys. Rev. C **86** (2012) 014905 doi:10.1103/PhysRevC.86.014905 [arXiv:1204.5381 [hep-ph]].

[27] M. B. G. Ducati, M. T. Griep and M. V. T. Machado, Phys. Rev. C **88** (2013) 014910 doi:10.1103/PhysRevC.88.014910 [arXiv:1305.2407 [hep-ph]].

[28] T. Lappi and H. Mantysaari, Phys. Rev. C **87** (2013) no.3, 032201 doi:10.1103/PhysRevC.87.032201 [arXiv:1301.4095 [hep-ph]].

[29] A. Adeluyi and C. A. Bertulani, Phys. Rev. C **85** (2012) 044904 doi:10.1103/PhysRevC.85.044904 [arXiv:1201.0146 [nucl-th]].

[30] S. Klein and J. Nystrand, Phys. Rev. C **60** (1999) 014903 doi:10.1103/PhysRevC.60.014903 [hep-ph/9902259].

[31] S. R. Klein and J. Nystrand, Phys. Rev. Lett. **92** (2004) 142003 doi:10.1103/PhysRevLett.92.142003 [hep-ph/0311164].

[32] V. Rebyakova, M. Strikman and M. Zhalov, Phys. Lett. B **710** (2012) 647 doi:10.1016/j.physletb.2012.03.041 [arXiv:1109.0737 [hep-ph]].

[33] T. H. Bauer, R. D. Spital, D. R. Yennie and F. M. Pipkin, Rev. Mod. Phys. **50** (1978) 261 Erratum: [Rev. Mod. Phys. **51** (1979) 407]. doi:10.1103/RevModPhys.50.261

[34] R.J. Glauber, "High Energy Physics and Nuclear Structure," ed. S. Devons, Plenum Press, New York, (1970).

[35] N. Cartiglia [H1 and ZEUS Collaborations], In *Stanford 1996, The strong interaction, from hadrons to partons* 337-363 [hep-ph/9703245].

[36] K. Aamodt *et al.* [ALICE Collaboration], JINST **3** (2008) S08002.

[37] E.C. Villar, "The AD detector array: a new tool for studying diffractive physics at the ALICE experiment," master's thesis at Pontifical Catholic University of Peru, Lima (2015).

[38] E. Cerron Zeballos, I. Crotty, D. Hatzifotiadou, J. Lamas Valverde, S. Neupane, M. C. S. Williams and A. Zichichi, Nucl. Instrum. Meth. A **374** (1996) 132. doi:10.1016/0168-9002(96)00158-1

[39] G. Herrera Corral, J. Phys. Conf. Ser. **624** (2015) no.1, 012008. doi:10.1088/1742-6596/624/1/012008

[40] L. Evans and P. Bryant, JINST **3** (2008) S08001. doi:10.1088/1748-0221/3/08/S08001

[41] I. Antcheva *et al.*, "ROOT: A C++ framework for petabyte data storage, statistical analysis and visualization," Comput. Phys. Commun. **180** (2009) 2499 [arXiv:1508.07749 [physics.data-an]].

[42] ALICE Collaboration, "The list of ALICE Physics Working Groups:" `http://alice-collaboration.web.cern.ch/PhysicsCoordination` [cited on 26.4.2016].

[43] J. Adam *et al.* [ALICE Collaboration], Phys. Lett. B **751** (2015) 358 doi:10.1016/j.physletb.2015.10.040 [arXiv:1508.05076 [nucl-ex]].

[44] M. Vidovic, M. Greiner, C. Best and G. Soff, Phys. Rev. C **47** (1993) 2308. doi:10.1103/PhysRevC.47.2308

[45] A .P .Kalweit, E. Kryshen, "Event and track properties:" `https://indico.cern.ch/event/327364/` [cited on 26.4.2016].

[46] J. Allen, "Perl programming language, Manual pages:" `http://perldoc.perl.org/perl.html` [cited on 26.4.2016].

[47] R. Lavicka, "Personal web pages:" `https://rolavick.web.cern.ch/rolavick/` [cited on 26.4.2016].

[48] E. Kryshen, "ALICE Event Selection QA official repository:" `http://aliqaevs.web.cern.ch/aliqaevs/data/2015/lumi_pb.png` [cited on 26.4.2016].

[49] J. Wiechula, " TPC tracking distortions:" `https://indico.cern.ch/event/489302/` [cited on 26.4.2016].

[50] R. Shahoyan, "2015 data production readiness:" `https://indico.cern.ch/event/506372/` [cited on 26.4.2016].